DYNAMIC BEARING SIMULATION USING COMBINED EFEM-DEM METHOD

by

Lijun Cao

A Dissertation

Submitted to the Faculty of Purdue University

In Partial Fulfillment of the Requirements for the degree of

Doctor of Philosophy

School of Mechanical Engineering

West Lafayette, Indiana

August 2018

THE PURDUE UNIVERSITY GRADUATE SCHOOL
STATEMENT OF DISSERTATION APPROVAL

Dr. Farshid Sadeghi, Chair

Department of Mechanica Engineering

Dr. Arun Prakash

Department of Civil Engineering

Dr. Carl Wassgren

Department of Mechanical Engineering

Dr. Jeffrey F. Rhoads

Department of Mechanical Engineering

Approved by:

Dr. Jay P. Gore

Head of the Departmental Graduate Program

This dissertation is dedicated
to my parents
Yuping Cao and Peihua Gu,
and to my love,
Yuting Yang.

TABLE OF CONTENTS

LIST OF TABLES

LIST OF FIGURES

ABSTRACT

Author: Cao, Lijun. Ph.D.
Institution: Purdue University
Degree Received: August 2018
Title: Modeling of Bearing Dynamics Using Combined EFEM-DEM Method
Major Professor: Farshid Sadeghi

The objective of this investigation was to develop a 3D dynamic model to study the rotor-bearing-housing system. To achieve the objective, an existing dynamic bearing model (DBM) was combined with a flexible bearing housing model and a flexible rotor model. The DBM is based on the discrete element method (DEM), in which all bearing components are assumed to be rigid and have six degrees of freedom. The 3D explicit finite element method (EFEM) was used to develop the flexible housing and rotor models. To couple the bearing outer race (OR) with housing, a novel algorithm was developed to detect contact conditions between the housing support and OR and then calculate contact forces based on the penalty method. A study of housing support geometry demonstrates that bearing support plays a large role on the dynamic performance of the bearing. Motion of bearing outer race is closely related to the geometry and deformation of the housing.

The effect of elastomeric bushing support on bearing dynamics was also studied and then compared to the bearing housings made with linear-elastic material. The EFEM was used to model a cylindrical elastomeric bushing, which was then coupled with DBM. Constitutive relationship for the elastomeric material is based on the Arruda-Boyce model combined which uses a generalized Maxwell-element model to capture both hyperelastic and viscoelastic behaviors of the material. Comparison between the two types of housings illustrated that elastomeric materials as expected have large damping to reduce vibration and absorb energy which leads to a reduction in ball-race contact forces and friction. It was also shown that a desired bushing support performance can be achieved by varying bushing geometry. Simulations using the combined EFEM bushing and DBM model demonstrated that the elastomeric bushing provides better compliance to bearing misalignment as compared to a commonly used rigid support model. Modeling with a bearing surface dent showed that vibrations due to surface abnormalities can be significantly reduced using elastomeric bushing

support. It has also been shown that choosing a proper bushing is an efficient way to tuning bushing vibration frequencies.

The model was further developed to study the effects of rotor and support flexibilities on the performance of rotor-bearing-housing system. The system is composed of a flexible rotor and two supporting deep-groove ball bearings mounted in flexible bearing housings. In order to combine the dynamic bearing model with finite element rotor and support system, new contact algorithms were developed for the interactions between the various components in the system. The Total Lagrangian formulation approach was applied to decrease the computational effort needed for modeling the rotor-bearing-housing system. The combined model was then used to investigate the effects of bearing clearances and housing clearances. It was found that as the rotor is deformed due to external loading, the clearances have a significant impact on the bearing varying compliance motion and reaction moments. Results also show that the deformation of the flexible housing depends on the total force and moment generated within the bearing due to rotor deformation. The first critical speed of rotor was simulated to investigate the unbalance response of the rotor-bearing system. It was demonstrated that rotor critical speed has a significant effect on inner race displacement and reaction moment generated at bearing location.

The dynamic behavior of the cage in a ball bearing was studied using experimental and analytical investigations. For the experimental investigation, a wireless sensor telemeter system was designed and developed to monitor the cage motions. The sensor, which was integrated on the bearing cage, is comprised of a commercially-available capacitor-inductor (LC) circuit. The LC circuit on the rotating cage was coupled to a transceiver which was stationary and positioned in close proximity to the cage. In order to achieve the objective of the analytical investigation, the explicit finite element method (EFEM) was used to simulate the bearing cage. The EFEM cage model was then combined with the dynamic bearing model to simulate the cage motion during operation. The results from the experimental measurement using the telemeter were then compared with the analytical modeling. The developed telemeter demonstrated the capability of the cage telemeter in detecting various bearing frequencies. These include: the cage frequency, shaft frequency, and ball pass frequency on outer race (BPFO) which was introduced by creating a spall on bearing outer race. Compared to standard accelerometers which are commonly used to measure vibrations on the bearing housing, the cage telemeter has shown advantage in sensing

cage motions and detecting bearing defect regardless of the location of the damage. Analytical simulation using the EFEM cage model correlated well with the experimental results and provided more insight into the bearing cage dynamics.

CHAPTER 1. INTRODUCTION

1.1 Background

Rolling element bearings are critical components in power transmission and are required to operate at optimum performance with minimum maintenance. However, factors such as deformation of rotor and housings, severe loading conditions and bearing surface abnormalities can cause great instability and result in imminent bearing failure. Therefore it is of critical importance to develop an analytical model to predict bearing dynamics under various operating conditions. Bearing modeling has been advanced tremendously over the last few decades, starting from the quasi-static model to the 3D dynamic model nowadays. However, existing bearing models commonly assume the bearing outer race to be fixed to ground, or apply a simplified one-dimensional support model which is insufficient since the 3D shape plays an important role in the determination of support performance. Moreover, as the bearing is fixed on a rotor which transmits power, displacements and misalignments of the rotor can significantly impact the bearing performance. In order to develop a more versatile and advanced bearing simulation tool, the Dynamic Bearing Model (DBM) previously developed in METL (Purdue University) is combined with flexible bearing housing and flexible rotor models. The new combined rotor-bearing system then can be used to investigate the effect of housing and rotor flexibilities on bearing dynamics, and to help optimize the design of bearing systems.

Bearings in general are always paired with a housing support to stabilize the motion of the shaft and bearing components. Steel housings (linear elastic materials) are the most common form of support for bearings which provide large stiffness and constraint for the bearing. However, the effect of housing geometries and deformation of the housing have been neglected in previously developed bearing models. The material of bearing support can be changed depending on the specific applications. In the support bearings for vehicle drive shaft and helicopter tail-rotor driveline, bearing support made with elastomeric materials are used to isolate vibration and reduce noise. Elastomeric bushings due to their shape flexibility and capabilities to isolate vibration have become a popular solution to reducing bearing vibrations and instabilities caused by, for instance, shaft misalignment and surface abnormalities (i.e., dents, spalls, etc.). A bearing bushing is typically manufactured as a hollow elastomeric cylinder sandwiched between

a bearing outer race and a rigid housing. The vibration transmitted through the bushing is damped as a result of the non-linear viscoelastic nature of elastomeric material. Because of the fact that the characteristics of elastomeric bushing depends closely on the material as well as the geometric nonlinearities, analytical methods for bushing design are not available, and often costly experimental work is required in order to achieve a reasonable optimized design. Therefore the development of a proper bearing housing support model is of significant importance to the dynamics of ball and rolling element bearings. In this study, the effects of housing material properties and geometry on bearing dynamics are investigated.

Rotors supported by rolling element bearings are extensively used in rotating machinery to transmit motion. In order to minimize the rotordynamic instabilities, the rotor-bearing system is required to operate without excessive vibration within a range of operating load and speed combination. Sources of instabilities from the bearing support component, such as bearing radial clearance, varying compliance and support stiffness are known to introduce vibration into the system and have to be properly accounted for in the design of rotor-bearing system. The flexibility of rotor, in return can also cause large displacements and misalignments on bearing elements, especially when the rotor goes through the critical speeds. Therefore, a more advanced modeling tool is needed to help understand the interactions between the rotor, bearing and housing, and analyze the effects of such interactions on the behavior of rotor-bearing system.

Rolling element bearings are widely used in rotating machineries. And the proper functioning of these machineries relies heavily on the operating condition of bearings. A defective bearing not only causes malfunction, but also can lead to excessive vibration, damage and eventually the failure of the entire machine. Different methods have been implemented for the detection and diagnosis of bearing defects, including the vibration and acoustic measurement, temperature measurements, and wear debris analysis. And a new technique for condition-monitoring is needed to improve the accuracy and response of the detection.

1.2 Review

1.2.1 Modeling of Rolling Element Bearing with Flexible Housing

There exists a large body of knowledge on bearing dynamics and modeling. Early research [1,2] focused on quasi-static models in which static equilibrium formulation was used and thus, the motion of bearing elements could not be exclusively studied. As computer capabilities improved in the 1970s, investigators concentrated on developing full bearing dynamic models. One of the successful 3D dynamic models was Advanced Dynamics of Rolling Elements (ADORE) developed by Gupta [3]. ADORE allows six degrees of freedom to all bearing elements except for the outer race which is assumed to be fixed in space (rigid housing). Saheta [4] developed a dynamic bearing model (DBM) based on the discrete element method. Ghaisas et al. [5] extended DBM and presented a model for cylindrical roller bearings. However, in their analysis the outer race was considered as fixed on ground as well.

Bearing outer races are fixed in a housing (steel, rubber, etc.) and therefore cannot be considered as fixed to the ground when investigating rotating machinery. Adams's [6] flexible multi-bearing rotors model included the effects of bearing support by using a pedestal model (spring and dashpot) with constant support stiffness. Stacke et al. [7] have developed an efficient rolling bearing simulation tool (BEAST) by using parallel computing to simulate the dynamic behavior of rolling bearings in three-dimensions. Stacke et al. [8] demonstrated that BEAST can be combined with shaft and rotor system and also connected with external systems using various connection methods. Available connection types include linear spring and dashpot elements for six degrees of freedom. When modeling bearing housings, spring and dashpot model greatly reduces computational effort. However, this approach will have difficulty in analyzing the effect of geometric non-linearity in a 3D support.

The disadvantages of using springs and dashpots to model the housing support mechanism can be eliminated by combining the finite element method with a dynamic bearing model. There has been significant progress made in coupling the finite element model and bearing model. Ashtekar and Sadeghi [9] modeled a flexible cage with explicit finite element method (EFEM) and coupled it with a dynamic ball bearing model which is based on the discrete element method [4]. The results from the combined model showed significant difference by comparing with the

rigid cage model and a discrete element cage model developed by Weinzapfel and Sadeghi [10]. The EFEM flexible cage also showed its advantage to simulate cage expansion due to centrifugal forces and predicting fatigue failure.

1.2.2 Modeling of Elastomeric Bushing

Hill [11] and Horton [12, 13] solved for and developed a closed-form approximation of the static load-deflection relations of rubber bushing mountings. The reduced formulation treated long and short bushings separately while assuming small deformations. Additional assumptions also had to be made in order for the final solution to be possible, and the assumptions proved that developing a pure analytical model to represent rubber bushing is very difficult. Berg [14] approached the problem by proposing a one dimensional non-linear rubber model which is based on a superposition of elastic, friction and viscous forces. Due to the simplicity of the model, it reduces computational effort and therefore becomes suitable to be integrated into a complex dynamic analysis system. However the model was only validated for a limited frequency range by using one dashpot element. The model is also incapable of handling the 3D effect of bushing flexibility. Sjöberg [15] followed the same approach developed by Berg [14] and extended the frequency range of the model by using fractional derivatives in the viscous dashpot element. But the final force-displacement response was established based on a predefined bushing geometry and cannot be generalized for other shapes.

To include the effect of shape flexibility, researchers have turned to the finite element method (FEM) for a more advanced simulation tool. Various constitutive models have been developed to characterize the nonlinear and rate-dependent behaviors of elastomeric materials. The Mooney-Rivlin model [16, 17] was one of the first aimed to estimate the elastic strain energy following an invariant-based continuum mechanics approach. But it is only capable of capturing the hyperelastic stress-strain behavior in extension tests and is not validated in other deformation modes. Yeoh [18] and Ogden [19] used higher order invariant terms of stretch tensor to improve the prediction of rubber material behavior at larger deformations of different modes. However, to use the models, more complicated experiments were required to identify the material parameters. Molecular chain statistics based network models [20 - 23] have been proved to be effective in rubber constitutive modeling with an insight into the characteristics of rubber at molecule level. Using this method, Arruda and Boyce [24] adopted Langevin statistics

developed by Kuhn and Grun [25] and proposed an eight-chain network model which was shown to match well with experimental results of various deformation tests. The eight-chain model is also mathematically simple and easy to apply. However the previous models only simulate hyperelastic behaviors at stationary deformations. In a dynamic analysis, the time-dependent viscoelasticity of elastomeric material must be considered as well. Bergström and Boyce [26] combined two polymer networks in parallel to include both hyperelastic and viscoelastic responses. But the mathematical complexity of the combined model makes the implementation into finite element method difficult and time-consuming. Kaliske and Rothert [27] developed an efficient three-dimensional viscoelastic formulation suitable for both small and finite strains. A generalized Maxwell-element rheological model was used and it was validated with experimental data for energy storage modulus and loss modulus over a wide range of excitation frequencies. Compared to the large number of developed rubber constitutive models, examples of applying these models in a dynamic analysis using finite element methods are few. Kadlowec [28] performed finite element analysis (FEA) to predict elastomer bushing response to large radial deformation and coupled deformations. The results of force-displacement curve compared well between the FEA simulation and experiments. But the bushing model does not consider rubber viscoelasticity, and therefore cannot be used in a dynamic analysis. Olsson [29] developed a finite element rubber bushing model in ABAQUS to study the rate and amplitude dependent effects of carbon-black filled rubber.

1.2.3 Modeling of Rotor-Bearing-Housing System

In rotating machinery, rotors are used to transmit torque and energy. And in the case of a rotor supported by ball bearings, flexibility of the rotor must be considered since the rotor deformation can result in the displacement and change of orientation of bearing elements. The Jeffcott model [30] is the first to investigate the rotor dynamics using a beam model, in which a uniform shaft is supported freely in bearings at its ends and carries a mass at the center. Kim and Noah [31] also implemented the Jeffcott rotor and obtained the synchronous and subsynchronous whirling motions with bearing clearances. After the Jeffcott model, the transfer matrix methods were introduced to study rotor dynamics. Lund [32] developed a rotor-bearing system mathematically by using a stiffness matrix, a damping matrix and an inertia matrix. Bansal [33] developed an analytical approach to calculate the damped critical speeds and instability threshold speed of

rotor-bearing systems. The method of solution is based on the transfer matrix method and the shaft is approximated as a series of lumped mass connected by massless beam elements. Then the finite element model became the new trend. Nelson and McVaugh [34] developed a general finite element method which included the effects of rotatory inertia, gyroscopic moments and axial load and the bearings were represented by linear stiffness and viscous damping. El-saeidy [35] modeled a rotor-rolling bearings system which combined a C^0 four-node finite element (FE) rotor model with the ball bearing system represented by simple external loads. But since the solution of FE rotor model uses modal analysis, the accuracy of the solution depends on the number of modes used. Gupta et al. [36] used circular Timoshenko beam finite element formulation to model the rotor system. However, the model can only be solved for steady-state periodic response since the shooting method is used in the integration algorithm.

Compared to simple beam model analysis, fewer compromises and simplifications are made in 3D solid element models. Rao and Sreenivas [37] used ANSYS and developed a 3D solid element model for dynamics of a dual rotor system. The effects of rotors, centrifugal forces and gyroscopic moments were investigated using this model. The supporting structure (casing) of the system was also found to influence the coupled motion of rotors. Ashtekar and Sadeghi [38] developed a model to represent the bearing-rotor system in a turbocharger. The model combines a bearing model with a 3D finite element rotor model developed using component mode synthesis, which is a reduced form of finite element method. Brouwer and Sadeghi [39] investigated the dynamics of flexible rotor systems supported by deep-groove ball bearings. The dynamic rotor model was developed with a full 3D elastic formulation using the EFEM. It was shown by Brouwer and Sadeghi [39] that the motion and orientation of the bearing inner race are altered by the deformation of the rotor, and results in larger ball spin and slip in bearing raceway.

Rotor and bearing analytical models, such as the investigations cited previously, commonly assume the bearing outer race (OR) to be fixed in space and exclude bearing support flexibility from the analysis. However, in applications such as gas turbine engines, etc., modeling the flexibility of the supporting foundations is critical for complete understanding of the behavior of the rotor bearing systems. Nicholas [40] studied rotor system critical speed by considering the effect of bearing support flexibility, which was modeled by a support spring, mass and damper in series with the bearing, and showed that the support stiffness varied the critical speed response of

an unbalanced rotor. Vance [41] used a similar approach and included the dynamics properties of foundation in the analysis of turbomachinery, and demonstrated that omission of the foundation from the model resulted in an inaccurate prediction of critical speeds. Vázquez [42] developed polynomial transfer functions to represent the support structure of a flexible rotor supported by fluid film bearings, and showed that the stability thresholds increased with the support flexibility. Cao et al. [43] developed a 3D flexible housing support model using the explicit finite element method (EFEM) and combined it with an existing dynamic bearing model (DBM). The combined model was used to demonstrate that the support stiffness depends on the geometry and boundary conditions and will significantly affect the bearing motions. However, the outer ring does not have a full 6 degrees of freedom. Cao and Sadeghi [44] applied an elastomer constitutive model and developed an EFEM elastomeric bushing model. The significant damping effect from the elastomeric bushing was shown to effectively reduce vibrations in the bearing system and the flexibility of elastomer also improved the compliance of bearing to shaft motions.

1.2.4 A Wireless Sensor Telemeter for In-Situ Cage Vibration Measurement and Corroboration with Analytical Results

Tandon and Choudhury [54], showed that different methods have been implemented for the detection and diagnosis of bearing defects. Among these available methods, the bearing vibration analysis is the most widely used approach. McFadden and Smith [55] were among the first to develop a model and describe the vibration produced by a rolling element bearing under constant load and a single point defect on the inner race. The point defect was modeled using an impulse function as a single impact load. Ashtekar et al. [49, 56] investigated the influence of race defects on the motions of bearing components using a dynamic ball bearing model. They developed a force-deflection relationship for the contact between a ball and a dented surface. The size and location of the dent were studied. Sawalhi and Randall [57] tested a seeded defect on bearing race and investigated the vibration signals resulting from the entry and exit of the rolling element when it comes into contact with the defect. They developed algorithms to quantify the defect size using the entry and exit signals.

Most of the bearing vibration measurements from previous studies used an accelerometer(s) and the sensor was commonly placed on the outer race or bearing housing since access to the internal

spaces of a bearing under operating condition is quite limited. This traditional sensing technique, however, has its limitation. Cao et al. [58] used a machine tool spindle system with a bearing defect and showed that the vibration response depended on the accelerometer placement. The transfer path between the excitation and response changes with the location of the accelerometer. Therefore, a wireless telemetry for bearing vibration detection is needed.

In the 1990s, researchers first started to develop and implement bearing telemeters for temperature measurement. Nickel and Sadeghi [50] were among the first to design and develop a microradiotelemeter to measure the in-situ temperature of the roller in a tapered roller bearing. A small circuit board was printed using photolithography and then it was installed into the roller of the tapered roller bearing with a battery case and an antenna. The results indicated that the temperature of the roller increased faster than the temperature of the housing. Based on the work of Nickel and Sadeghi [50], Joshi et al. [51] designed and developed a remotely powered temperature telemeter mounted on a bearing cage. Therefore, the size of the telemeter was reduced and the measurement was not limited by the battery life. Ashtekar et al. [53] and Brouwer et al. [59] have tested a bearing cage telemeter in a turbocharger bearing cartridge. The telemeter was based on a temperature-sensitive capacitor in an LC circuit. The telemetry system has demonstrated its capability in wirelessly measuring bearing cage temperature at high speeds (~100 krpm). The temperature telemeter was used for the development of a vibration telemeter for bearing cage.

Among all of the bearing elements (outer race, inner race, rolling element and cage), the dynamics of the bearing cage has particularly drawn much attention from researchers in the field, since it is considered to be the most flexible element and its behavior affects the performance of the bearing. Kannel and Bupara [60] developed an analytical model describing the in-plane motions of a bearing cage stability and motion. Gupta et al. [61] investigated cage unbalance motion via both experiment and simulation. Their results showed a critical shaft speed at which the cage mass center began to whirl. Stacke et al. [7, 8] developed a rolling bearing simulation model called BEAST (BEAring Simulation Tool), and considered the cage to be rigid in the model. The simulation results showed the variation of the cage orbit under different loading conditions and the simulation results were validated with experimental measurements. Ghaisas et al. [5] studied the dynamics of a rigid cage in a cylindrical roller bearing. They found that

instability of cage motion leads to discrete cage-race collisions with high force magnitudes. Note that previous bearing models commonly assume the cage to be rigid, but the most recent works have included cage flexibility in the model. Weinzapfel and Sadeghi [10] used a discrete element approach to model cage flexibility in a ball bearing. In the cage model, the cage pockets are discrete elements connected by flexible fibers. Ashtekar and Sadeghi [9] developed a 3D explicit finite element model (EFEM) of the cage which was combined with a discrete element bearing model. Both works investigated the effects of flexible cage and showed a reduction in the ball-cage contact force.

1.3 Scope of the Dissertation

The scope of this dissertation covers the investigations of the dynamics of bearing system which was modeled using the combined EFEM-DEM simulation method. The bearing system includes a bearing model and flexible models for rotor and bearing housings. In Chapter 2, an existing dynamic bearing model (DBM) was combined with a flexible bearing housing model and a flexible rotor model. The DBM is based on the discrete element method (DEM), in which all bearing components are assumed to be rigid and have six degrees of freedom. The 3D explicit finite element method (EFEM) was used to develop the flexible housing and rotor models. To couple the bearing outer race (OR) with housing, a novel algorithm was developed to detect contact conditions between the housing support and OR and then calculate contact forces based on the penalty method. A study of housing support geometry and housing materials was carried out in this chapter. In Chapter 3, a 3D explicit finite element method (EFEM) was developed to model a cylindrical elastomeric bushing, which was then coupled with an existing dynamic bearing model (DBM) Constitutive relationship for the elastomer is based on the Arruda-Boyce model combined with a generalized Maxwell-element model to capture both hyperelastic and viscoelastic behaviors of the material. Results were obtained to show the effects of damping capability and flexibility of the elastomeric bushing on bearing behavior. In Chapter 4, a model was developed to study the effects of rotor and support flexibilities on the performance of rotor-bearing-housing system. The system is composed of a flexible rotor and two supporting deep-groove ball bearings mounted in flexible bearing housings. The dynamics of the ball bearings were simulated using an existing dynamic bearing model, which was developed using the discrete element method (DEM). The explicit finite element method (EFEM) was used to model

the flexibilities of the rotor and bearing support. . The combined model was then used to investigate the effects of bearing clearances and housing clearances. And it was shown that the dynamics of rotor, bearing and housing are interdependent on each other. In Chapter 5, a wireless sensor telemeter system was designed and developed to monitor the cage motions and the explicit finite element method (EFEM) was used to simulate the bearing cage. The developed telemeter demonstrated the capability of the cage telemeter in detecting cage frequencies and bearing defect. Compared to standard accelerometers, the cage telemeter has shown advantages in sensing cage motions and detecting bearing defect regardless of the location of the damage. Analytical simulation using the EFEM cage model correlated well with the experimental results and provided more insight into the bearing cage dynamics. Chapter 6 summarizes the completed work and gives an overview of the future work.

CHAPTER 2. EFFECT OF HOUSING SUPPORT ON BEARING DYNAMICS

2.1 Introduction

The goals of this chapter were to determine the effects of housing materials and geometries on bearing performance by combining a discrete element dynamic bearing model with an EFEM housing model. The interaction between the bearing and the EFEM housing is achieved by using a robust contact algorithm, which solves the contact between the deformable support and rigid outer race. In order to investigate both linear elastic and elastomeric housing supports, a constitutive model for an elastomeric rubber material was developed by combining the eight chain model with a generalized Maxwell-element viscoelastic model to include both hyperelastic response and time-dependent response. The results demonstrate that the housing support has a significant effect on the performance of the bearing and it is critical in comprehensive modeling of bearing dynamics.

2.2 Model Description

Figure 2.1 illustrates a flowchart progression of the combined DBM and EFEM housing support model. In this approach, first, the states of bearing components are initialized and the finite element mesh for the deformable housing is generated. As the simulation starts, DBM and the EFEM are combined as two parallel networks, in which DBM solves for the new state of each bearing component and EFEM calculates the deformed state of bearing housing. During each time step, contact forces between DBM and EFEM housing are determined using a contact algorithm. The following sections will describe the DBM, the EFEM housing models for both linear-elastic and viscoelastic elastomeric materials, and the rigid-flexible contact model.

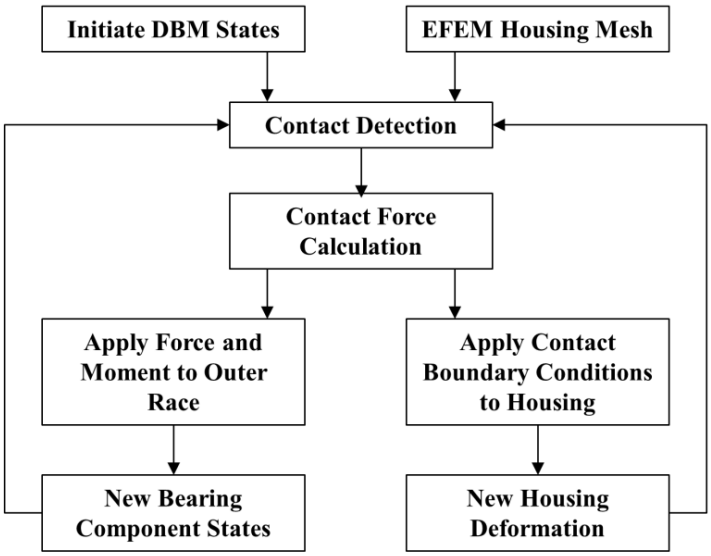

Figure 2.1. Flowchart of the combined model.

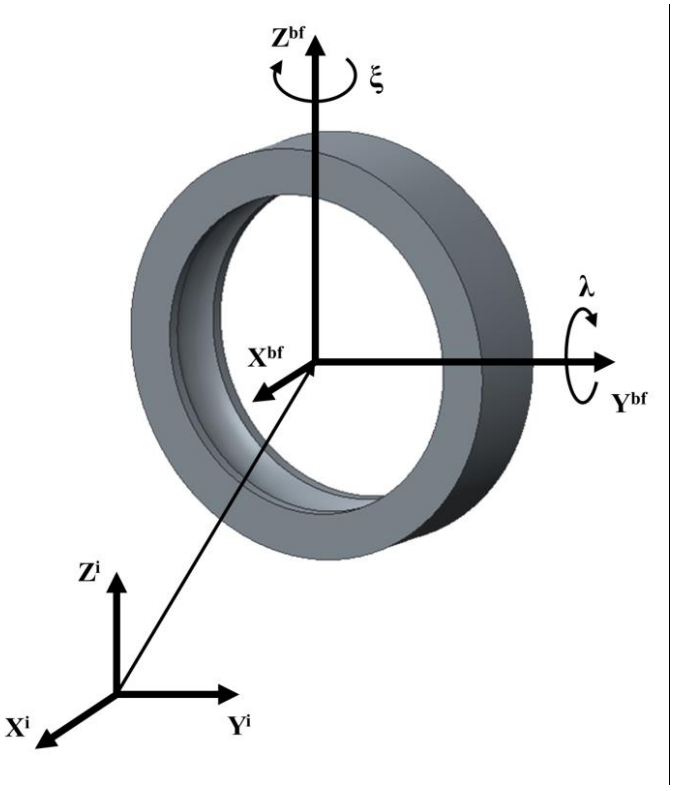

Figure 2.2. Outer race reference frame.

2.2.1 Dynamic Bearing Model

In this investigation, the dynamic bearing model for deep-groove ball bearings developed by Saheta [4] was modified to account for housing support deformation. The DBM is based on the discrete element method in which each of the bearing components (i.e. races, balls and cage) is considered rigid and has six degrees-of-freedom (6 DOFs). The frictional torque applied to the outer race is not large enough to cause significant sliding motion at the outer race and housing interface. Therefore the outer race was allowed five degrees of freedom, three for translation and two for rotation, as illustrated in Figure 2.2. Translation of the outer race occurs in the X-, Y- and Z-axes of inertial reference frame, while rotation takes place about Y- and Z-axes of the body-fixed frame, which is fixed at the center of mass of outer race and aligned with principle axes.

When bearing elements (balls, races, etc.) come in contact, their local elastic deformation is significantly smaller as compared to the characteristic length of the elements. Therefore, the Hertzian force deflection relationship was used to account for this local deformation;

$$F_N = K_H \delta^{3/2} \tag{2.1}$$

where K_H is the Hertzian stiffness coefficient and δ is the amount of deformation which in this analysis is the amount of geometric overlap between the bearing elements. The stiffness coefficient K_H is given by Hamrock et al. [45].

In addition to the normal force, a tangential frictional force also exists between the bearing elements. The calculation of tangential force uses the magnitude of the normal force and the relative velocity between components at the contact point. It is assumed that only the variation of the relative velocity along the major axis of the contact ellipse is considered since the length of minor axis is negligible compared to the length of major axis. The calculation of relative velocity considers the relative slip at the center of the contact ellipse and the additional slip, which varies along the major axis, due to the local spin about the contact center. The friction coefficient is assumed to be a function of magnitude of the relative velocity, and a description of this function is given by Weinzapfel and Sadeghi [10]. More details of the tangential contact force can be found in Brouwer and Sadeghi [39]. After evaluating the net force and moment

acting on each bearing component using the normal and tangential forces, the translational and rotational accelerations can be determined using Newton's law of motion. Then the accelerations and velocities are integrated in time using the Fourth Order Runge-Kutta integration scheme to calculate the new states of position and velocity of each bearing component. This procedure is repeated until steady state condition is reached.

2.2.2 Explicit Finite Element Model – Linear Elastic Material

One of the goals of this study was to simulate the dynamic deformation of different types of materials using EFEM. Therefore, an efficient numerical algorithm was necessary to account for the interaction between the DBM rigid outer race and EFEM for the housing. This was achieved by using the total Lagrangian formulation, in which all stresses and strains are referred to the undeformed configuration, and therefore most of the spatial derivatives can be pre-computed. A detailed description of this algorithm is given by Miller et al. [46].

In this investigation, tetrahedral elements were used to model steel housing (linear elastic materials). The formulation of EFEM with linear elastic material is described by Ashtekar and Sadeghi [9].

Deformation of the elements is calculated using the Right Cauchy-Green deformation tensor

$$\boldsymbol{C}_{ij} = \boldsymbol{F}^T\boldsymbol{F} \tag{2.2}$$

where F is the deformation gradient tensor with respect to the undeformed configuration. With the deformation tensor C_{ij}, strain can be evaluated using the Lagrangian strain tensor

$$\boldsymbol{E}^L_{ij} = \frac{1}{2}(\boldsymbol{C}_{ij} - \boldsymbol{\delta}_{ij}) \tag{2.3}$$

Then the second Piola-Kirchoff's material stress is calculated using

$$\boldsymbol{S}_{ij} = \frac{E}{1+v}(\boldsymbol{E}^L_{ij} + \frac{v}{1-2v} tr(\boldsymbol{E}^L_{ij})\boldsymbol{\delta}_{ij}) \tag{2.4}$$

where v is Poisson ratio and E is Young's modulus. To determine the stress in the deformed configuration, the second Piola-Kirchoff stress is transferred to Cauchy stress T using,

$$\boldsymbol{T} = J^{-1} \cdot \boldsymbol{F} \cdot \boldsymbol{S} \cdot \boldsymbol{F}^{T} \tag{2.5}$$

where J is the determinant of deformation gradient tensor F. As the volume of each element is sufficiently small, the state of stress is assumed to be uniform within an element. Therefore the traction force on each face of the tetrahedron can be obtained by,

$$f = (\boldsymbol{T} \cdot n) \cdot A \tag{2.6}$$

with A being the face surface area and n being the face outward normal. The traction force is then equally distributed over all three nodes of the face. The external contact force, which will be discussed in a later section, is added to the nodal force calculated in Equation (2.6) to determine the total nodal force. After the total nodal force F_t is determined, the equation of motion for each node

$$m\ddot{x} = F_t - C_d\dot{x} \tag{2.7}$$

can be integrated in time to determine the new states of position and velocity for each node. In Equation (2.7), m is the mass of node and C_d is the material damping coefficient. The same process is repeated for each element within the housing mesh, therefore the deformation state of the entire housing support is continuously updated at each time step.

2.2.3 Explicit Finite Element Model – Elastomeric Material

The EFEM previously described was modified to include the effects of elastomeric (rubber) housing materials. Rubber can undergo large strains and nonlinear elastic deformation and is also characterized by its rate-dependent viscoelastic nature. Therefore, the rheological model of rubber, as shown in Figure 2.3, is represented by a generalized Maxwell element model, which consists of two parts: a Hookean element to represent the hyperelastic response at equilibrium and a finite number of separate Maxwell elements in parallel to represent the time-dependent viscoelastic response.

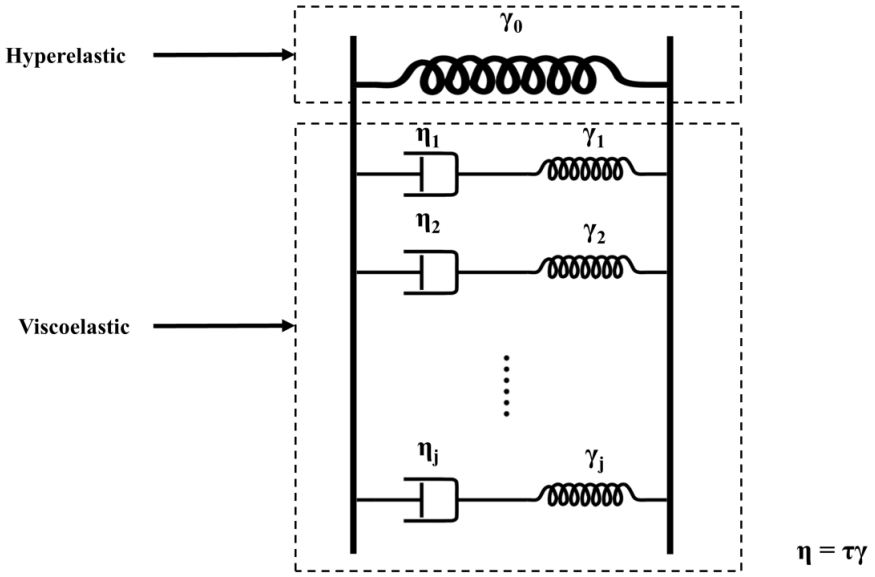

Figure 2.3. Generalized Maxwell-element rheological model.

The hyperelastic stress and strain relationship is derived from a strain energy function which is based on the eight chain model developed by Arruda and Boyce [24]. However, according to Bower [47], a dynamic analysis should include the effect of compressibility of rubber to account for the volume change of elements under large deformation. Therefore the strain energy function for rubber hyperelastic behavior is given in the compressible form

$$W = CR\left[\frac{1}{2}(\bar{I}_1 - 3) + \frac{1}{20N}\left(\bar{I}_1^{\,2} - 9\right) + \frac{11}{1050N^2}\left(\bar{I}_1^{\,3} - 27\right) + \frac{19}{7000N^3}\left(\bar{I}_1^{\,4} - 81\right) + \frac{519}{673750N^4}\left(\bar{I}_1^{\,5} - 243\right)\right] + \frac{B}{2}(J-1)^2 \quad (2.8)$$

where

$$\bar{I}_1 = \frac{I_1}{J^{2/3}} \quad (2.9)$$

$$I_1 = trace(\boldsymbol{C}) \quad (2.10)$$

and $\boldsymbol{C}$ is the Right Cauchy-Green deformation tensor given by Equation (2.2). There are three material parameters in the strain energy function: the rubbery modulus CR, the network locking stretch N, and the bulk modulus B. The stress-strain relations for hyperelastic response is then deduced by differentiating the strain energy function using

$$\boldsymbol{S} = \frac{\partial W}{\partial \boldsymbol{F}}\boldsymbol{F}^{-T} \quad (2.11)$$

where $\boldsymbol{S}$ is the second Piola-Kirchhoff stress from the hyperelastic response. The final expression of $\boldsymbol{S}$ is then derived to be

$$\boldsymbol{S} = \frac{2CR}{J^{\frac{2}{3}}}\left(\frac{1}{2} + \frac{I_1}{10NJ^{2/3}} + \frac{33I_1^2}{1050N^2J^{4/3}} + \frac{76I_1^3}{7000N^3J^2} + \frac{2595I_1^4}{673750N^4J^{8/3}}\right)\left(\boldsymbol{\delta}_{ij} - \frac{I_1}{3}\boldsymbol{C}^{-1}\right) + JB(J-1)\boldsymbol{C}^{-1} \tag{2.12}$$

The viscoelastic part of the constitutive structure is represented by the Maxwell elements in Figure 2.3. The derivation of the numerical model for large strain computation is given by Kaliske and Rothert [27]; therefore, only the formulation ready for a finite element implementation is provided here. The stress contribution of each viscous Maxwell element is given by

$$\boldsymbol{H_j^{n+1}} = \exp\left(-\frac{\Delta t}{\tau_j}\right)\boldsymbol{H_j^n} + \gamma_j \frac{1-\exp(-\frac{\Delta t}{\tau_j})}{\frac{\Delta t}{\tau_j}}[DEV\ \boldsymbol{S^{n+1}} - DEV\ \boldsymbol{S^n}] \tag{2.13}$$

where $DEV\ \boldsymbol{S}$ is the deviatoric part of $\boldsymbol{S}$, τ is the relaxation time constant and γ is normalized elastic constant. The total viscoelastic stress of all Maxwell elements is added to the hyperelastic stress $\boldsymbol{S}$ to give the total second Piola-Kirchhoff stress $\boldsymbol{S_{tot}}$

$$\boldsymbol{S_{tot}^{n+1}} = \boldsymbol{S^{n+1}} + \sum_{j=1}^{N}\boldsymbol{H_j^{n+1}} \tag{2.14}$$

With the total stress determined, the same process described in the previous section is followed to calculate nodal forces. It should be noted that viscous damping effect in the rubber material model is inherent in the constitutive model in Equation (2.14), therefore no damping coefficient is needed in the equation of motion of node, and the equation of motion for each node can be simplified to

$$m\ddot{x} = F_t \tag{2.15}$$

which is integrated in time to solve for the deformation of rubber.

2.2.4 Rigid – Flexible Contact Model

A contact model was developed to determine the interaction between the DBM bearing model and EFEM bearing support. The surfaces that may experience contact are the outer surface of

the rigid outer race and the inner surface of the finite element housing. In order to solve the contact forces, a constraint enforcement approach based on the penalty method was developed to resist the penetration of the nodes of deformable body into the rigid body. When the two bodies are in contact, the magnitude of the normal contact force is proportional to the penetration distance of each node into the surface of rigid body. Because the outer race is a rigid body of an annular shape, the penetration of node is easily calculated in the outer race body-fixed frame. To transform from the inertial frame to the body-fixed frame, the 1, 2, 3 the Euler angle sequence was used. The transformation matrix is given by

$$\boldsymbol{T_{trans}} = \begin{bmatrix} \cos\xi\cos\lambda & cos\eta sin\lambda + sin\eta sin\xi cos\lambda & sin\eta sin\lambda - cos\eta ssin\xi cos\lambda \\ -cos\xi sin\lambda & cos\eta cos\lambda - sin\eta sin\xi sin\lambda & sin\eta cos\lambda + cos\eta sin\xi sin\lambda \\ sin\xi & -sin\eta cos\xi & cos\eta cos\xi \end{bmatrix} (\qquad 2.16)$$

where the first angle η , which is the axial rotation of the outer race, is fixed to be zero and the other two angles ξ and λ are related to the rotations about the body-fixed axes Y and Z. Figure 2.4 shows a representative node A in proximity of the outer race. And the vector connecting C and A in the outer race body-fixed frame is given by

$$r_{AC}^{bf}(x_{bf}, y_{bf}, z_{bf}) = \boldsymbol{T_{trans}} \cdot r_{AC}^{i}(x_i, y_i, z_i) \qquad (2.17)$$

where r_{AC}^{i} is the vector r_{AC} in the inertial frame. The distance d

$$d = \sqrt{y_{bf}^2 + z_{bf}^2} \qquad (2.18)$$

is the radial component of vector $\boldsymbol{r}_{AC}$ in body fixed Y-Z plane. If d is smaller than the outer radius of outer race R_{OR}, then node A is detected to penetrate the outer race. And the normal contact force between node A and outer race can be calculated by

$$F_n^{bf} = (R_{OR} - d) * K * n \qquad (2.19)$$

where K is the contact stiffness constant used in the penalty method and n is the outward unit normal to the outer race surface at contact point. In the penalty method, infinitely large contact stiffness constant K is ideal to enforce the constraint of no penetration between two bodies in contact. However a K too large will significantly reduce the stability of the solution. Therefore,

a small amount of penetration is allowed in the solution by choosing a reasonable value of K to improve the convergence rates while not affecting the accuracy of the solution. A validation of the contact model is presented in the next subsection (2.3.2). In this investigation, $K = 2.5e8\ N/m$ was used for outer race and steel contact and $K = 5e6\ N/m$ was used for outer race and rubber contact. The calculated nodal contact forces are added to F_t of Equations (2.7) and (2.15) to determine the total force acting on each node.

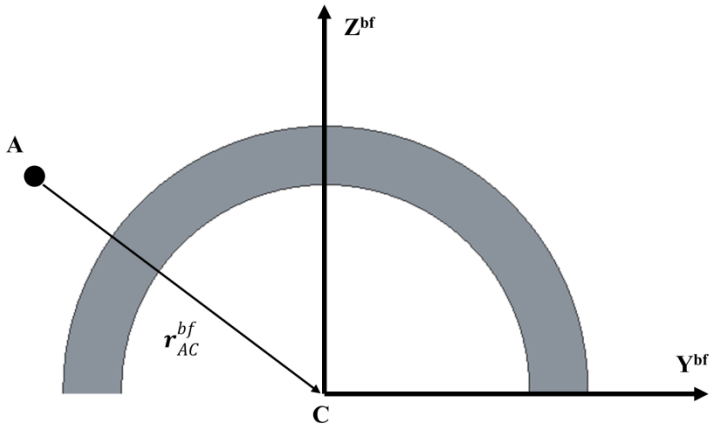

Figure 2.4. Outer race and contacting mode.

2.3 Model Validation

2.3.1 Elastomeric Model

The proposed constitutive model for elastomeric material was verified by comparing with the experimental results given by Bergström and Boyce [26]. Determination of the material constants was accomplished by fitting the model to the stress-strain results obtained from uniaxial compression experiments of a chloroprene rubber with 15 parts per hundred carbon black. In this study, the material constants for the eight chain hyperelastic model are CR = 0.324 MPa, N = 8.0, B = 100 CR, and the parameters for the Maxwell-element model in Equation (2.13) were adjusted based on the values given by Kaliske and Rothert [27].

The uniaxial compression test conducted by Bergström and Boyce [26] was repeated in the current investigation using the EFEM. A 12mm rubber cube meshed with tetrahedral elements, as illustrated in Figure 2.5, was developed and tested to compare with previously published

experimental results. The cube was subject to deformation by applying a displacement controlled load on the top face; therefore the cube was compressed at a constant strain rate and was free to stretch in the other two directions. Figure 2.6 depicts the results of the stress-strain curves obtained from the current FE model and compares with the experimental data in Bergström and Boyce [26]. The stress and strain hysteresis loops are compared at different final strain levels and show good quantitative agreement. However, at high strain levels, discrepancies are found during the unloading. According to Bergström and Boyce [26], the reason is that the model exhibits the same time-dependent behavior during loading and unloading, but experiment shows that Chloroprene rubber exhibits lower time-dependence during unloading. It should be noted that when the loading and unloading compression test is carried out at higher rate, the rate-independent hyperelastic stress remains the same, but the viscoelastic stress increases. The slope of the stress-strain curve and the size of the hysteresis loop will increase as well. As a result, the effective dynamic stiffness of rubber becomes larger.

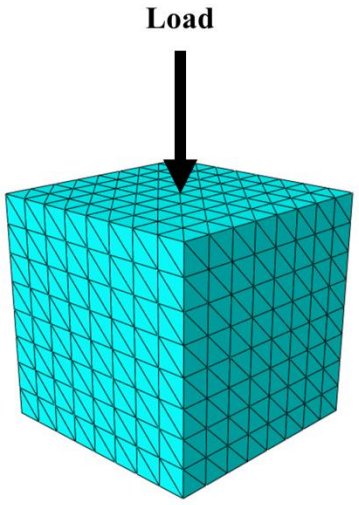

Figure 2.5. 12mm side cubic finite element network.

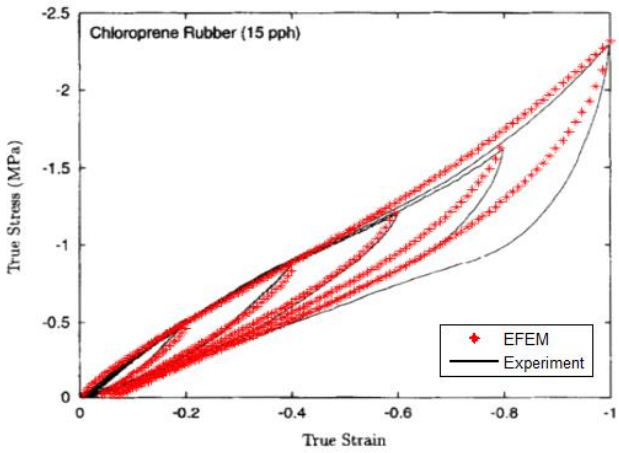

Figure 2.6. Uniaxial compression to different final strains. Strain rate $\dot{\varepsilon} = -0.01s^{-1}$.

2.3.2 Contact Model

Figure 2.7 depicts a rigid cylinder (e.g. outer race of a bearing) compressed against a deformable rectangular cuboid. The theoretically three-dimensional semi-infinite domain was truncated to a rectangular cuboid with a width eight times the largest half-contact width (a range of half-contact widths were modeled), a height five times the largest half contact width and a depth the same as the largest half contact width. The cylinder has a circular profile of radius 35.5 mm and the same depth as the flat surface. The EFEM deformable rectangular cuboid was modeled with linear elastic property, and with modulus of elasticity of 210 GPa and Poisson ratio of 0.3. In the contact region, an area three times wider and 1.5 times as deep of the largest half contact width was finely meshed, in order to accurately model the contact.

Table 2.1. Maximum stress comparison for contact validation.

Displacement (μm)	EFEM (MPa)	Abaqus (MPa)	% Difference
0.5	316.02	329.01	-3.95
1	456.45	469.54	-2.79
2	673.97	698.39	-3.50
3	856.15	866.25	-1.17
4	1032.73	1031.02	0.17
5	1181.42	1186.20	-0.40

The results obtained from the ABAQUS and EFEM contact model were corroborated. Figure 2.8 depicts the qualitative comparison of the von Mises stress distribution between both

simulations. The results are in good agreement. Table 2.1 contains a comparison of the maximum stresses and the error between the current EFEM model and ABAQUS. The result indicates that the models are in good agreement with a maximum relative error of less than 4%. Figure 2.9 and Figure 2.10 demonstrate that the contact pressure distribution from the EFEM is in good agreement with ABAQUS solution and the analytical Hertzian contact pressure profile.

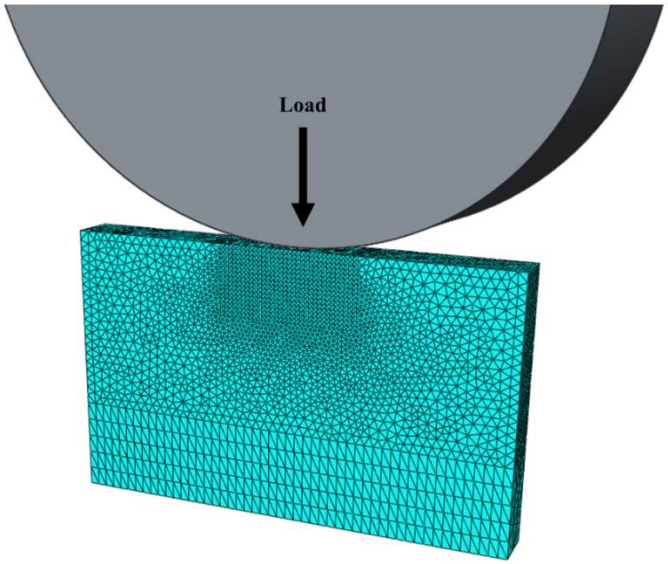

Figure 2.7. Hertzian line contact between rigid and flexible bodies.

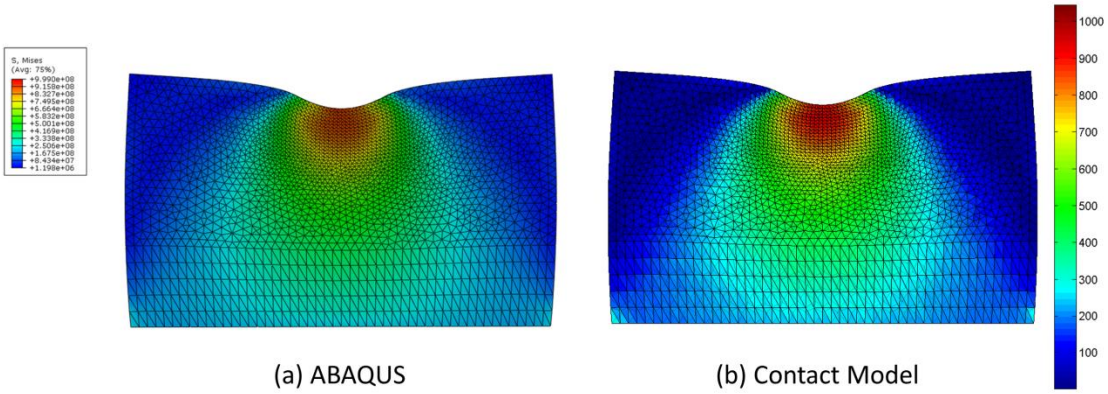

Figure 2.8. Von Mises stress results: (a) ABAQUS and (b) EFEM contact model results (100 × deformation).

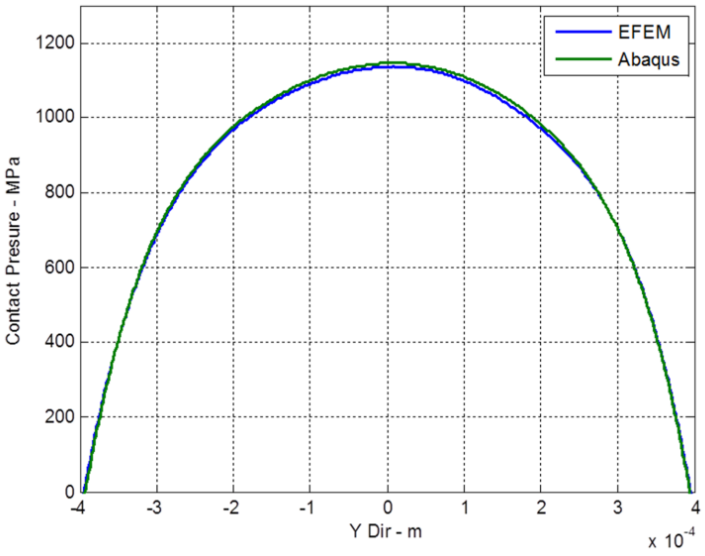

Figure 2.9. Comparison of ABAQUS contact pressure (green) and EFEM contact model pressure (blue).

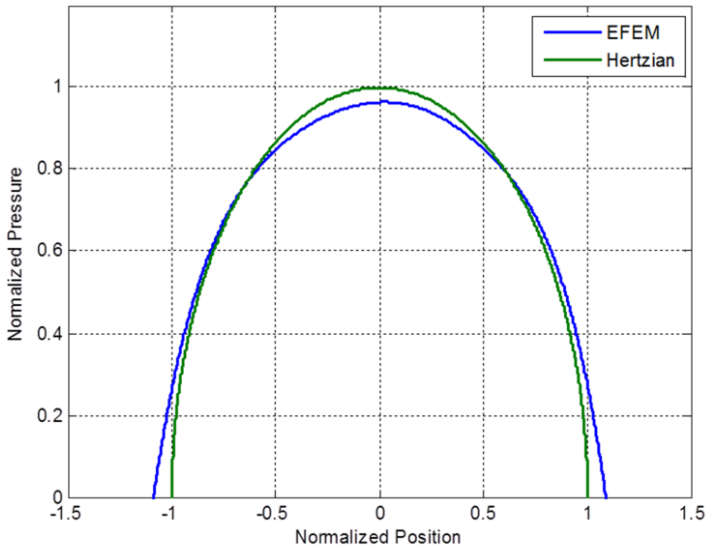

Figure 2.10. Comparison of Hertzian pressure (green) and EFEM contact model pressure (blue).

2.4 Results and Discussion

The combined DBM and EFEM housing were used to investigate the effects of bearing housing material and flexibility on the dynamics of ball bearings. In this section, the results of housings with various geometries and material properties will be discussed. Table 2.2 provides the geometry of a deep-groove ball bearing and Table 2.3 gives the housing material properties. Figure 2.11 depicts the dimensions of various housing geometries developed for this investigation. Please note that the housings are various iterations of the commonly used pillow block housing shown in Figure 2.11 (c). Housing A is a square cuboid, and Housing B was created by duplicating the part of Housing C below X-Y plane to generate a mirror image. Housing D is simply an annular cylinder. For housing A, all four sides were fixed, for housing B, the top and bottom surfaces were fixed, for housing C, the bottom surface was fixed and for housing D, the annulus was fixed to the ground.

Table 2.2. Bearing specifications.

Bearing Type	Deep Groove
Number of Balls	8
IR Radii (mm)	20.047
IR Groove Radii (mm)	6.013
OR Radii (mm)	31.953
OR Groove Radii (mm)	6.310
OR Thickness (mm)	3.574
Ball Radius (mm)	5.955
Cage Pocket Radius (mm)	6.200
Bearing Depth (mm)	20.0

Table 2.3. Material constants.

Material - Steel	
Modulus of Elasticity (GPa)	210
Density (kg/m^3)	7850
Poisson's Ratio	0.3
Mass Proportional Damping Coefficient (1/s)	77
Material - Rubber	
Rubber Modulus CR (MPa)	0.324
Network Locking Stretch N	8
Bulk Modulus (MPa)	100 * CR

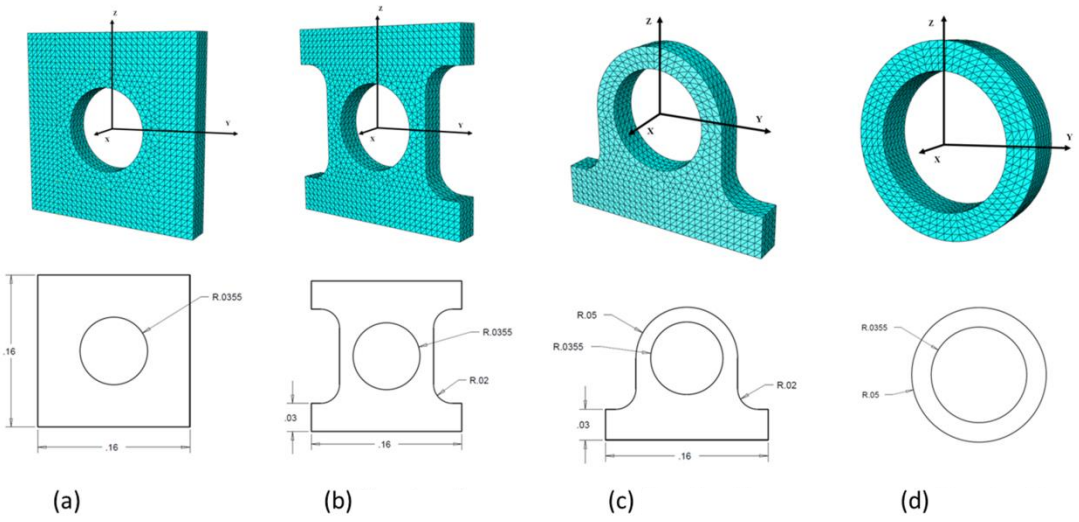

Figure 2.11. Geometries and dimensions of housing supports (a) Housing A. (b) Housing B. (c) Housing C. (d) Housing D.

2.4.1 Effect of Assembly Tolerances

Housing support characteristics are significantly influenced by assembly tolerances. A load, as shown in Figure 2.12 was gradually applied at the center of gravity (CG) of the inner race in the negative Z direction, and the inner race was rotated at 2000 rpm.

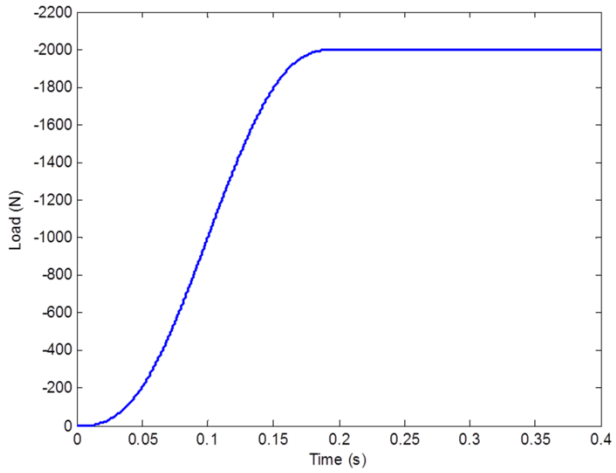

Figure 2.12. Assembly tolerance study – load profile.

Enforcement of the assembly tolerance is achieved by adjusting the outer diameter of the outer race, as shown in Figure 2.13. The thickness h is varied to account for the change in outer race outer diameter. Table 2.4 lists a range of assembly tolerances used to investigate the effects of housing tolerance on bearing performance. The housing bore radius was set to be the same as outer race outer radius (including thickness h). A clearance fit is modeled by reducing the thickness h. Modeling of the interference fit, however used a different approach, since a sudden increase in h will result in a large overlap between the outer race and the housing nodes; and thus lead to instability in the FE solution. Therefore, A three-step process was followed instead: (1) bearing is assembled in the housing with a transition fit, (2) the simulation is started and gradually increase the outer race thickness h, so the EFEM can solve for the housing deformation due to interference, (3) check the stability of the solution after the interference fit is applied.

Table 2.4. Assembly tolerances.

Case	Fit Tolerance
1	Clearance 1μm
2	Transition
3	Interference 1μm
4	Interference 5μm
5	Interference 10μm

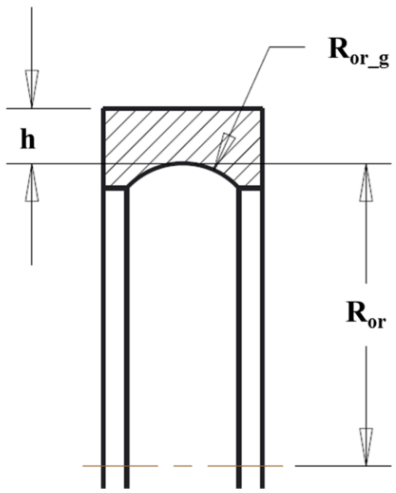

Figure 2.13. Bearing outer race cross-section view.

Figure 2.14 shows the stress distributions in the housing supports after the load was applied to the bearing. The normal contact forces between nodes and bearing outer race are indicated by the black arrows mapped to the magnitude of the force. It is demonstrated that as the assembly tolerance changed from interference fit to clearance fit, the distribution of contact forces became more concentrated due to the reduction of contact area between outer race and housing. This resulted in a decrease of the housing support stiffness, as illustrated by the load and displacement curves depicted in Figure 2.15. In the first two cases (clearance fit and transition fit), the outer race is only in contact with a portion of circumference. The support stiffness is the largest in the interference fit cases. Note that in all three interference fit cases, since the bearing outer race was supported by the complete circumference of the housing bore, the support stiffness was nearly the same.

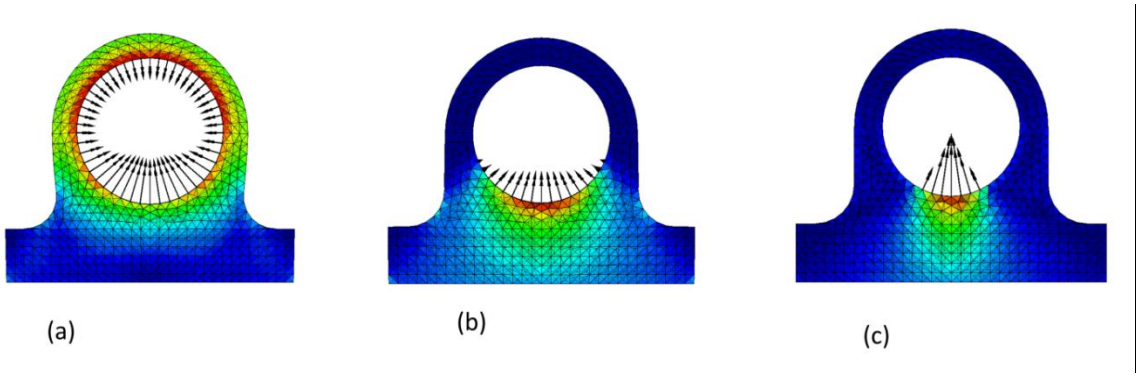

Figure 2.14. Housing stress and contact force distribution (Front View). (a) Interference fit. (b) Transition fit. (c) Clearance fit.

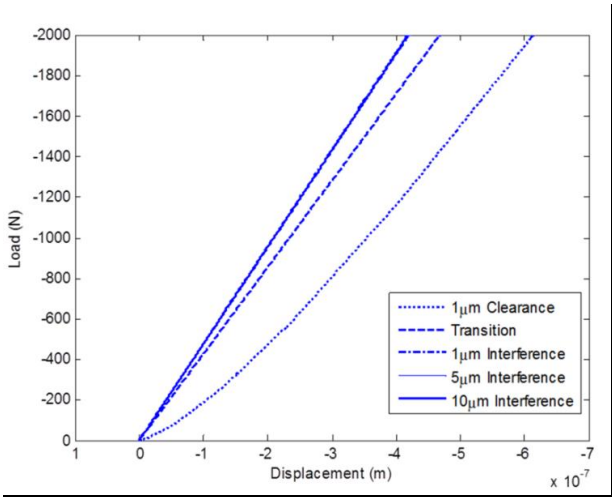

Figure 2.15. Housing support load – displacement curve for different assembly tolerances.

2.4.2 Effect of Housing Geometry

Bearing models developed in the past either assumed a rigid housing support (fixed bearing outer race) or used a simplified spring-dashpot model, in which the load and displacement relation is invariant to housing geometry. In this investigation, the bearing dynamics in various housing geometries was studied. For comparison purposes, housings A, B, and C depicted in Figure 2.11 were used to support the bearing and study the effect of housing geometry variation. A radial load of 250N was applied to the bearing which was transition fitted into the three housings and the load was rotated about bearing CG at 50 rpm. In this study, all three housings were modeled with steel, the deformation of which is not time-dependent.

Figure 2.16 depicts the contact force distribution and deformation of Housing A, at every 90 degrees of load rotation. When all outer edges of the square housing were fixed, elastic deformation of the housing is small regardless of the direction of load application. Therefore the outer race displacement was nearly the same in all radial directions. The identical stress patterns and contact force distributions also confirmed that Housing A provides the same support in any radial directions.

Figure 2.17 shows the results obtained from the bearing supported in Housing B. The elliptical orbit of the outer race CG motion illustrated that symmetry of the outer race motion is consistent with the symmetry of housing geometry and fixed boundary conditions. The plots of stress and contact force distribution show that the fillets and fixed bases of Housing B are stiffer than the necks to resist deformation. So when the load was applied in the positive and negative Y directions, the radial displacement of outer race CG was larger than in other loading directions.

Figure 2.18 illustrates that outer race CG motion changed significantly when the bearing is in Housing C. The deformation mechanism of the housing support varies at different loading directions. When the load was applied in the negative Z direction, the outer race compressed against the base of Housing C, and displacement of the outer race was small. When the load was applied in the positive Y direction, the annulus part of the housing inclined due to the bending moment created by the load. When the load was applied in the positive Z direction, housing deformation was due to the elongation in the necks as the result of the tensile stress (red stress

region near the necks) between upper annulus and housing base. Note that the contact force distribution is more uniform due to the fact that the thickness of upper annulus is uniform.

Figure 2.19 shows the comparison between the resulting outer race CG motions in the three housings. It is clear that the shape of the orbit is closely related to the geometry of housing support. The orbit of outer race CG in Housing A was the smallest and nearly a perfect circle. As housing wall thickness reduced at various locations in Housing B and C, the outer race displacement increases as a result of the reduced supporting stiffness at those locations.

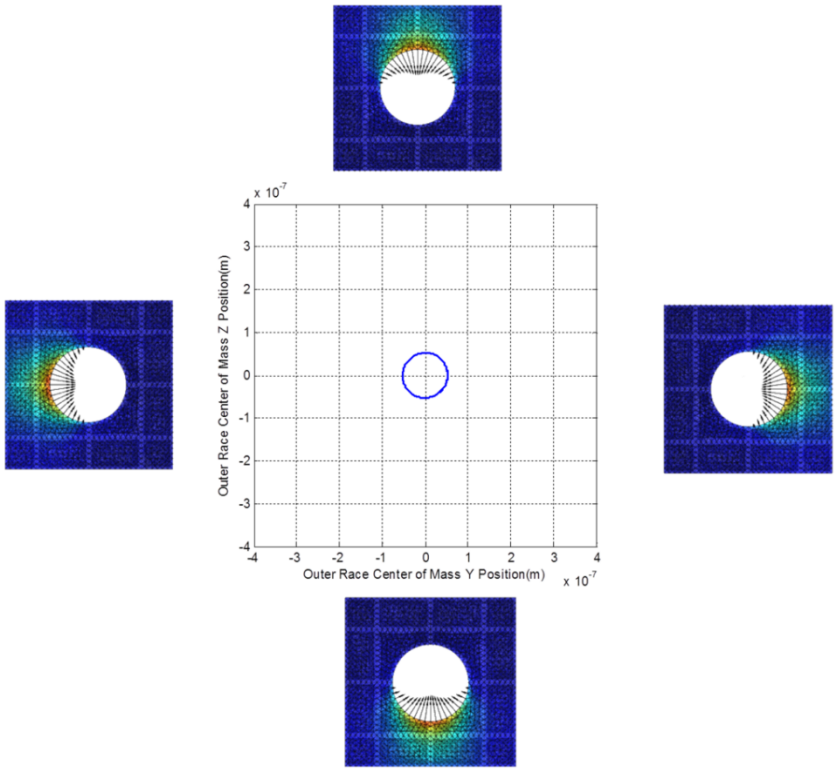

Figure 2.16. Outer race center of mass motion in Housing A and housing deformations (60000×deformation).

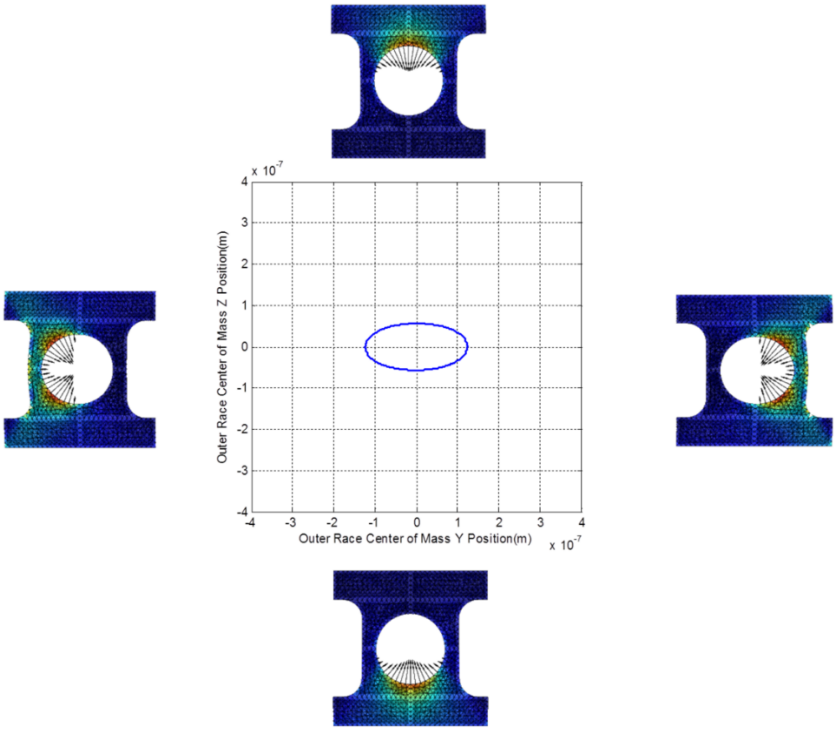

Figure 2.17. Outer race center of mass motion in Housing B and housing deformations (60000×deformation).

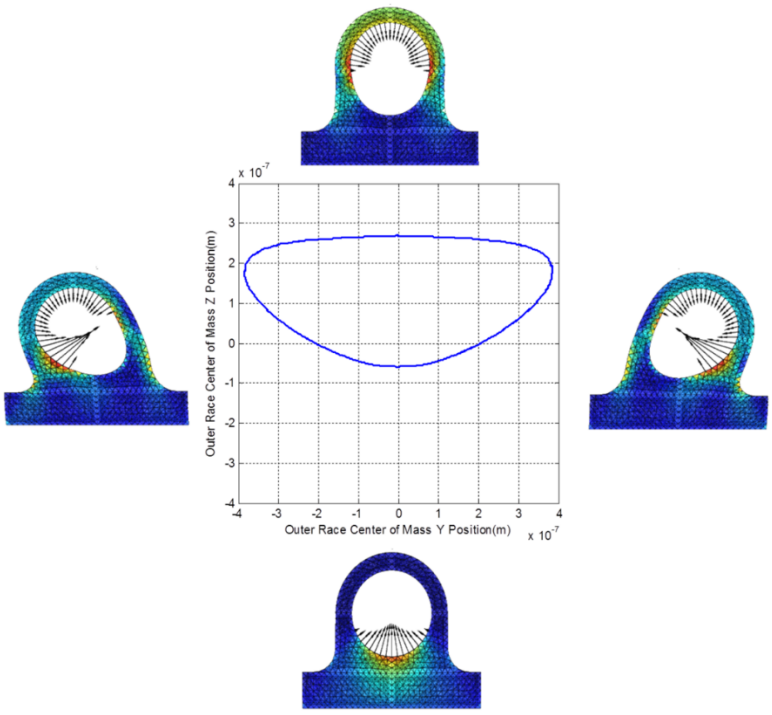

Figure 2.18. Outer race center of mass motion in Housing C and housing deformations (60000×deformation).

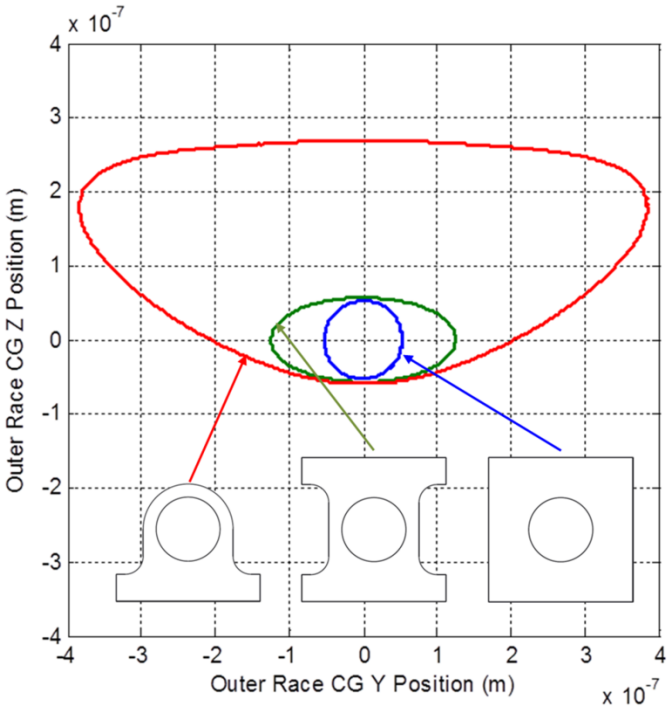

Figure 2.19. Outer race CG motion under the support of Housing A (blue), Housing B (green) and Housing C (red).

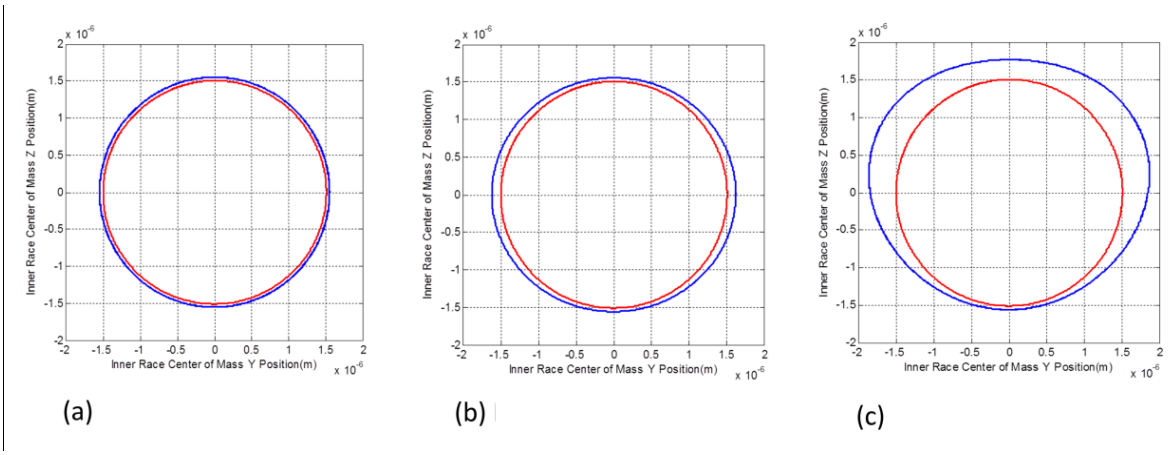

Figure 2.20. Comparison of inner race center of mass motion in rigid housing (red) and flexible housing (blue). (a) Results in Housing A. (b) Results in Housing B. (c) Results in Housing C.

Housing flexibility affects the motion of bearing outer race as well as bearing inner race. Figure 2.20 illustrates the comparison of the motion of inner race CG between the bearings with rigid housing support and with deformable housing support. When the outer race was fixed, inner race displacement was only the result of elastic deformation due to Hertzian contacts between the balls and races. If flexibility of housing is considered, the inner race motion orbit size will increase significantly due to the outer race displacements. The results presented here cannot be obtained through any type of analysis which ignored the contribution of flexibility in housing geometries.

2.4.3 Effect of Housing Materials

In many bearing applications where vibration isolation is a critical issue, bushings made of elastomeric materials are used to separate the bearing outer race and the housing, thus reducing vibration. In this section, results are presented to compare between bushings (Housing D) made of rubber and steel.

Figure 2.21 illustrates the load profiles applied to the bearing from 0 N to 250 N over three different rates (time durations). In the case where steel was used to model the bushing of the same geometry, the radial displacements of bearing outer race shown in Figure 2.22 followed the same profiles regardless of the rate of load application. The reason is that in an elastic material, the load and deflection relation is rate-independent. Alternatively, the EFEM rubber bushing exhibited a time-dependent characteristic. Figure 2.23 depicts the motion of outer race CG displacement with rubber bushing under the same loads depicted in Figure 2.21. The rubber bushing was deformed fast during load increment and started creeping after the load reached steady state value. Before creep process started, the faster the load was applied the smaller deformation was observed in the rubber bushing. This is due to the fact that when the strain rate is high, the viscoelastic stress in rubber increases to prevent the rapid deformation. After 30 seconds of simulation time, the displacements of outer race in all three cases converged to the same level, since rubber will eventually reach the same equilibrium state with the same steady state load.

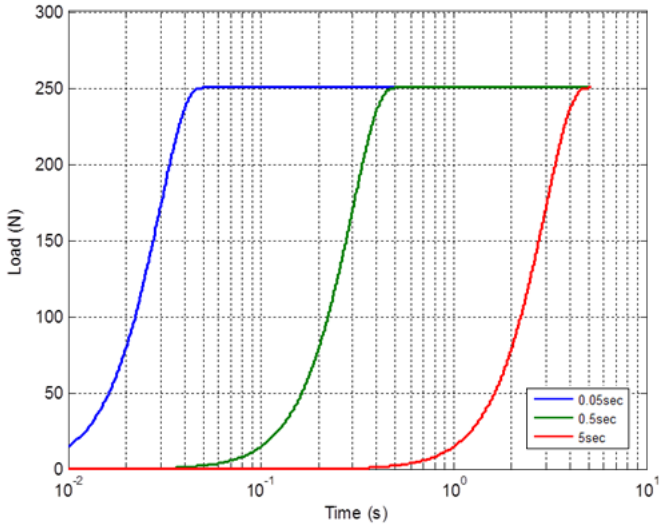

Figure 2.21. Profiles of 250N radial load applied in different rates.

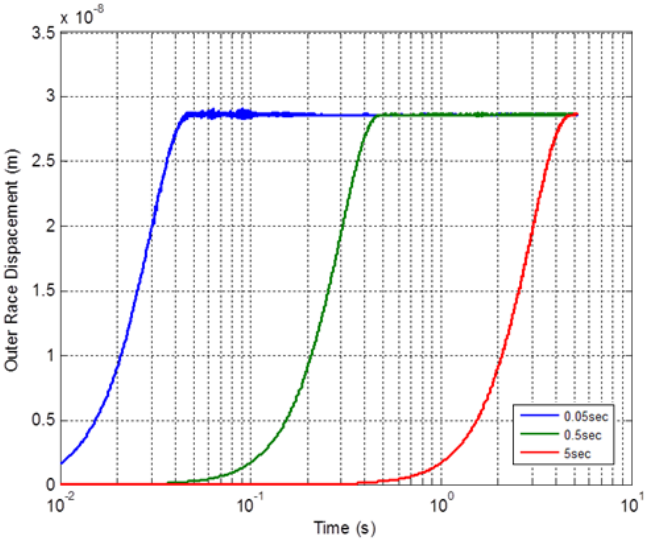

Figure 2.22. Curves of outer race displacement in steel bushing subject to the radial loads in Figure 2.21.

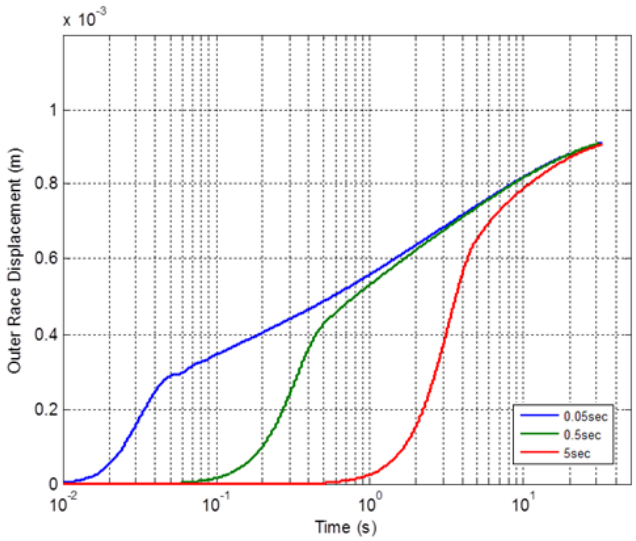

Figure 2.23. Curves of outer race displacement in rubber bushing subject to the radial loads in Figure 2.21.

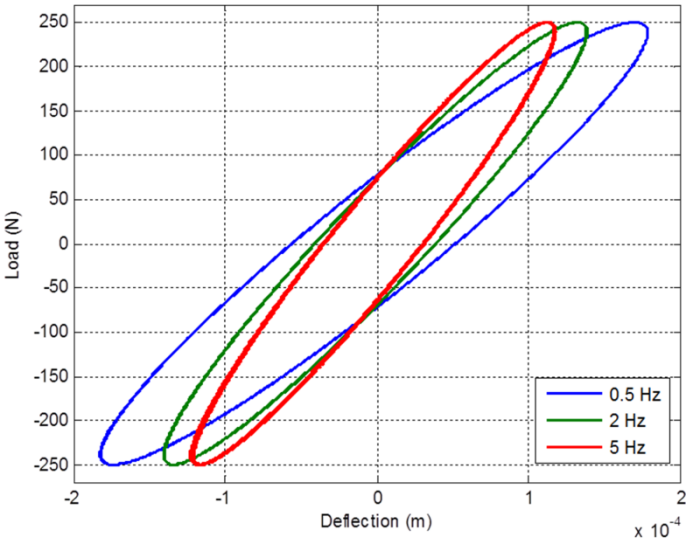

Figure 2.24. Rubber bushing cyclic deformation test.

Characteristics of the elastomeric materials are also illustrated in a cyclic deformation test. A harmonic excitation loading was applied to the bearing supported by the rubber bushing. The viscoelastic behavior, as shown in the hysteresis loops in Figure 2.24 indicates the energy dissipation capability of rubber material. The slope of the hysteresis loop changes according to the rate of deformation. When the deformation was carried out at a higher frequency, the stiffness property embedded in the viscoelasticity of materials increased as well.

In addition to radial loading, an investigation of impact loading was conducted in order to investigate rubber bushing advantage over steel in absorbing vibration and reducing contact forces. An impulse force depicted in Figure 2.25 was applied to the bearing in the negative Z direction to simulate an impact load. Bearing was assembled with interference in both rubber bushing and steel bushing. Figure 2.26 illustrates the summation of normal contact force between outer race and balls in the loading direction after the impact. The rubber bushing reduced the amplitude of force oscillation to nearly zero in just 0.1 seconds, while in the case with steel bushing, the high frequency force oscillation slowly decayed over a much longer time period. In the bearing and rubber bushing system, the vibration energy introduced by the impact load was mostly absorbed through rubber internal friction. In the case with steel bushing, however, due to the fact that steel has small damping capability, the system depends on the bearing ball-race frictions to dissipate energy.

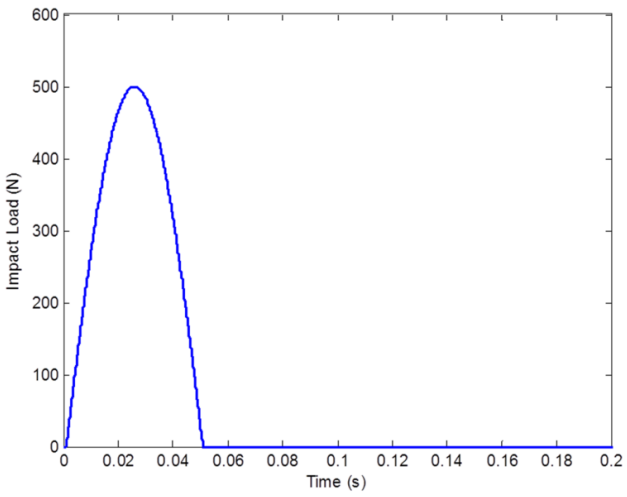

Figure 2.25. Impact load profile.

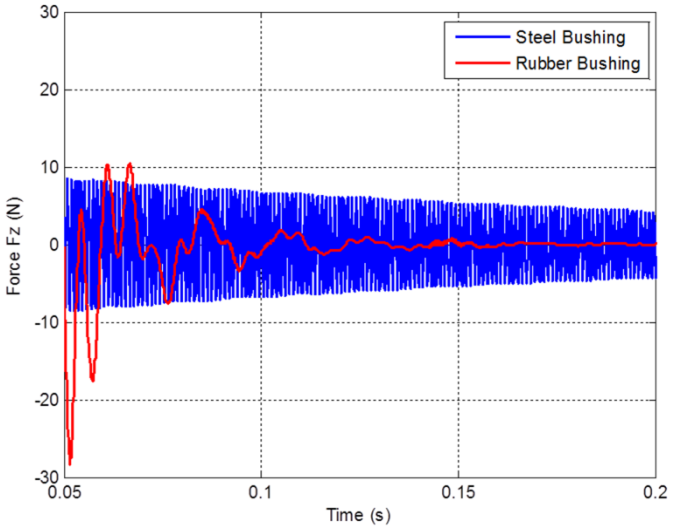

Figure 2.26. Summed normal contact forces between outer race and balls in Z direction after impact.

A parametric study was conducted to understand the relation between the hyperelastic and viscoelastic stress components in the constitutive model of rubber by proportionally changing the contribution of viscoelastic stress (VS) in the total stress in Equation (2.14). Figure 2.27 shows the results of outer race CG motion supported by rubber bushing with a range of VS contributions. It is clear that a rubber model with higher viscoelasticity will "delay" the deformation upon a sudden load. When only 10% of viscoelastic stress was included, the hyperelastic response overshadowed the viscoelastic behavior and rubber bushing exhibited the rate-independent characteristic of linear elastic materials. However, decrease of VS caused the rubber material to lose its capability in absorbing vibration after a rapidly applied load, as seen in the increasing vibration amplitude.

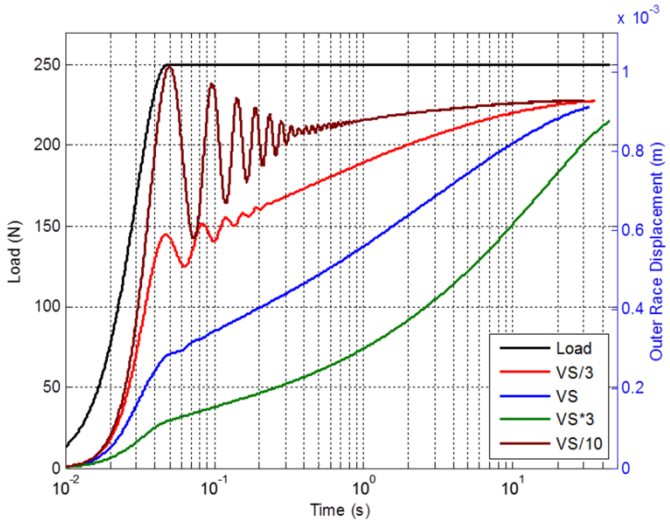

Figure 2.27. Outer race displacement curves in rubber bushings with different levels of viscoelasticity.

2.5 Conclusions

An explicit finite element model was developed to model bearing housings and combined with a discrete element dynamic bearing model to investigate the effect of housing flexibility on bearing dynamics. In this investigation, all bearing components are allowed six degrees-of-freedom except the outer race was only allowed five DOF. The DOF which allows for the bearing to rotate (fret) in the housing was neglected. Two different housing support materials (i.e. elastic and viscoelastic) were considered in this investigation using EFEM. A novel rigid and deformable body contact model using the penalty method was developed to detect and determine contact forces between the rigid outer race and deformable housing. Housings with different geometries were developed and used to demonstrate the effects of housing on outer race and inner race motions. The results from this investigation show that the housing deformation is significant and cannot be neglected in modeling bearing dynamics. The analysis for rubber bushing demonstrated that, due to the viscoelastic behavior, rubber deformation is rate dependent and as expect illustrated the rubber advantage over steel in damping impact loading.

CHAPTER 3. AN EXPLICIT FINITE ELEMENT MODEL TO INVESTIGATE THE EFFECTS OF ELASTOMERIC BUSHING ON BEARING DYNAMICS

3.1 Introduction

The goal of this chapter was to study the effects of elastomeric bushing on bearing dynamics using a combined dynamic bearing (DBM) and flexible bushing (EFEM) model. The constitutive material model is comprised of the eight-chain hyperelastic model developed by Arruda and Boyce [24] and the generalized Maxwell-element viscoelastic model developed by Kaliske and Rothert [27]. Both elastomeric material properties and bushing geometry are varied to create a basis for different bushings analysis. The bearing is supported by the EFEM bushing in a three-dimensional space, and the operational conditions are changed as a function of load, misalignment and surface discontinuities. The results demonstrate that elastomer bushing is effective in reducing vibrational reaction forces caused by impact loading or surface defects. Flexibility of the elastomeric bushing is also shown to improve bearing performance when misalignment occurs on bearing races.

3.2 Model Description

In this study the elastomeric bushing was modeled as an annular cylinder sandwiched between a rigid bearing outer race and ground using EFEM with tetrahedral elements. Figure 3.1 illustrates the flowchart of the combined EFEM bushing and DBM model. First, the states of bearing elements are initialized and the finite element mesh for the flexible bushing is generated. During the dynamic simulation, stresses and reaction forces are calculated according to the bushing deformation, which is enforced by the displacement of outer race. New states of bearing elements and nodes of the bushing mesh are updated using the Fourth Order Runge-Kutta integration scheme.

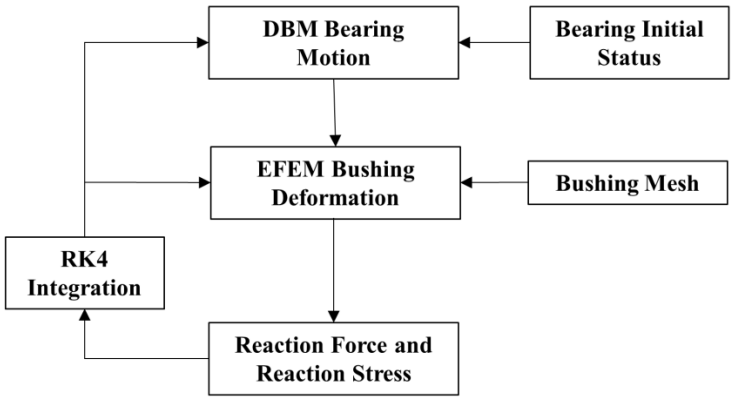

Figure 3.1. Flowchart of the combined bearing bushing model.

3.2.1 Elastomeric Bushing Model

Based on the EFEM formulation described by Ashtekar and Sadeghi [9], Cao et al. [43] developed the EFEM model for elastomeric materials. The rheological representation of this model, as shown in Figure 3.2, is composed of two parts: a Hookean element to represent the hyperelastic response at equilibrium and a number of Maxwell elements in parallel to model the rate-dependent viscoelastic behavior.

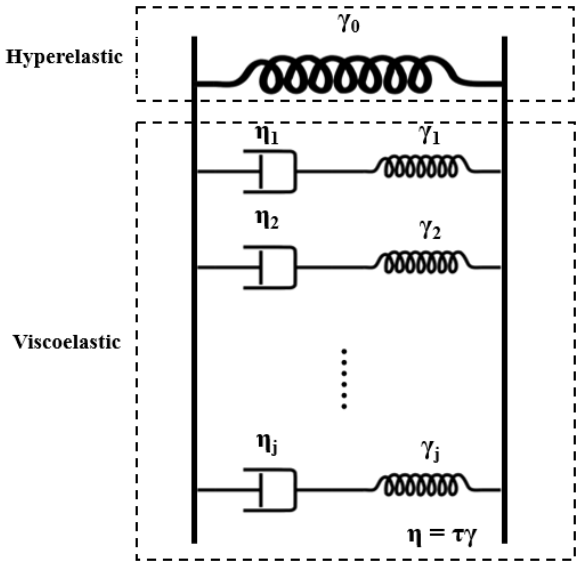

Figure 3.2. Elastomer material rheological model.

The hyperelastic stress and strain relationship is derived from a strain energy function using the eight chain model [24]. In a dynamic analysis, the compressible form of the eight chain model is given by

$$W = C_R\left[\frac{1}{2}(\bar{I}_1 - 3) + \frac{1}{20N}\left(\bar{I}_1^2 - 9\right) + \frac{11}{1050N^2}\left(\bar{I}_1^3 - 27\right) + \frac{19}{7000N^3}\left(\bar{I}_1^4 - 81\right) + \frac{519}{673750N^4}\left(\bar{I}_1^5 - 243\right)\right] + \frac{B}{2}(J-1)^2 \tag{3.1}$$

where

$$\bar{I}_1 = \frac{I_1}{J^{2/3}} \tag{3.2}$$

$$I_1 = trace(\boldsymbol{C}) \tag{3.3}$$

$$\boldsymbol{C}_{ij} = \boldsymbol{F}^T\boldsymbol{F} \tag{3.4}$$

$$J = \det(\boldsymbol{F}) \tag{3.5}$$

$\boldsymbol{C}$ is the Right Cauchy-Green deformation tensor and $\boldsymbol{F}$ is the deformation gradient tensor with respect to the undeformed configuration. The material constants included in Equation (3.1) are the elastomeric material modulus C_R, the network locking stretch N and the material bulk modulus B, which is equal to $100C_R$. The second Piola-Kirchhoff stress for the hyperelastic response is then deduced by differentiating the strain energy function using

$$\boldsymbol{S} = \frac{\partial W}{\partial \boldsymbol{F}}\boldsymbol{F}^{-T} \tag{3.6}$$

and the final expression of $\boldsymbol{S}$ becomes

$$\boldsymbol{S} = \frac{2C_R}{J^{\frac{2}{3}}}\left(\frac{1}{2} + \frac{I_1}{10NJ^{2/3}} + \frac{33I_1^2}{1050N^2J^{4/3}} + \frac{76I_1^3}{7000N^3J^2} + \frac{2595I_1^4}{673750N^4J^{8/3}}\right)\left(\boldsymbol{\delta}_{ij} - \frac{I_1}{3}\boldsymbol{C}^{-1}\right) + JB(J-1)\boldsymbol{C}^{-1} \tag{3.7}$$

The finite element formulation of the Maxwell elements for large strain computation was solved by Kaliske and Rothert [27]. The stress contribution of each viscous Maxwell element is given as

$$\boldsymbol{H_j^{n+1}} = \exp\left(-\frac{\Delta t}{\tau_j}\right)\boldsymbol{H_j^n} + \gamma_j \frac{1-\exp(-\frac{\Delta t}{\tau_j})}{\frac{\Delta t}{\tau_j}}[DEV\ \boldsymbol{S^{n+1}} - DEV\ \boldsymbol{S^n}] \tag{3.8}$$

where $DEV\ \boldsymbol{S}$ is the deviatoric part of tensor $\boldsymbol{S}$, τ is the relaxation time constant and γ is normalized viscoelastic constant. The viscoelastic stress of each Maxwell element is added to the hyperelastic stress $\boldsymbol{S}$ to give the total second Piola-Kirchhoff stress $\boldsymbol{S_{tot}}$

$$\boldsymbol{S_{tot}^{n+1}} = \boldsymbol{S^{n+1}} + \sum_{j=1}^{N} \boldsymbol{H_j^{n+1}} \tag{3.9}$$

To determine the stress in the deformed configuration, the second Piola-Kirchhoff stress is transferred to Cauchy stress $\boldsymbol{T}$ using,

$$\boldsymbol{T} = J^{-1} \cdot \boldsymbol{F} \cdot \boldsymbol{S_{tot}} \cdot \boldsymbol{F}^T \tag{3.10}$$

Therefore the traction force on each face of the tetrahedron can be obtained by,

$$f = (\boldsymbol{T} \cdot n) \cdot A \tag{3.11}$$

where A is the face surface area and n is the face outward normal. The traction force is then equally distributed over all three nodes of the face. After the total nodal force F_t is determined, the equation of motion for each node is;

$$m\ddot{x} = F_t \tag{3.12}$$

can be integrated in time to determine the new states of position and velocity for each node. As the state of each element within the bushing mesh is continuously updated following the same process, the dynamic deformation of the bushing can be obtained.

3.2.2 Dynamic Bearing Model

The dynamic bearing model (DBM) for deep-groove ball bearings developed by Saheta [4] was used for bearing dynamics analysis. DBM is based on the discrete element method which assumes each bearing element (i.e. races, balls and cage) to be a rigid body with six degrees-of-freedom. The normal contact force and tangential frictional force are calculated to account for the interactions between bearing elements. The normal contact force is determined using the Hertzian force deflection relationship, in which the amount of geometric overlap between the

two bodies is approximated as the local contact deformation. The calculation of the tangential force uses the magnitude of the normal contact force and the friction coefficient which is assumed to be a function of the magnitude of the relative velocity at contact point. Details of the tangential force formulation can be found in Brouwer and Sadeghi [39]. The normal and tangential forces are then used to determine the net force and moment applied on each bearing element. The translational and rotational accelerations are integrated in time to solve for the dynamic motions of bearing elements.

3.3 Elastomeric Bushing Model Validation

The EFEM elastomeric bushing model and pertinent simulations were compared with experimental results published by other researchers [28, 48]. Cao et al. [43] verified the constitutive elastomer model with simulating a uniaxial compression test on a 12mm rubber cube. The resulting stress-strain hysteresis loops are in good agreement with the experimental data obtained by Bergström and Boyce [26]. In the following sections (3.3.1 and 3.3.2), simulations using the EFEM bushing model will be corroborated with previously published experimental studies. For the harmonic excitation tests presented in the following studies.

3.3.1 Elastomer Viscoelasticity

To verify the viscoelastic behavior of elastomeric bushings, experimental results from Kadlowec [28] were compared to the solutions from the current EFEM bushing model. Kadlowec [28] conducted one-dimensional deformation tests on an elastomeric bushing with 60mm axial length, 18.2mm outer radius and 9.85mm inner radius. Radial deformation was imposed following a step displacement at a constant rate until final displacement was reached. Figure 3.3 depicts the deformation history. The step displacement was ramped to 1.0mm with various rise times: 0.2, 0.5, 1, 2, 4, and 8 seconds. The same radial deformation tests were simulated in the EFEM elastomeric bushing model using a bushing mesh (Figure 3.4) of the same dimensions. Elastomeric material constants were given by Kadlowec [28].

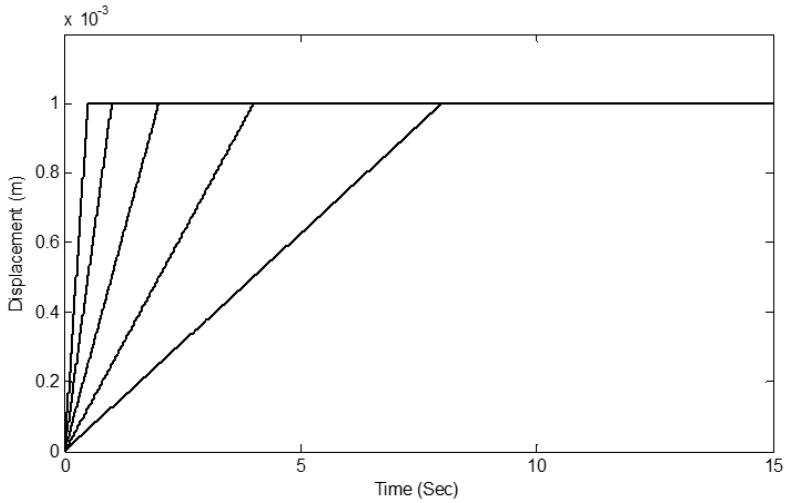

Figure 3.3. Deformation history of radial step loads with various ramp speeds.

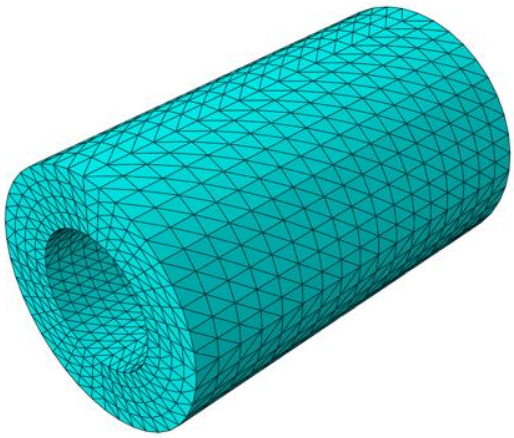

Figure 3.4. FE mesh for the same elastomer bushing used in Kadlowed [28].

Figure 3.5 shows the force relaxation response to the step displacement recorded by Kadlowec [28] and Figure 3.6 depicts the results from the EFEM simulation. The simulated responses correlate well with the experimental data, and both captured the importance of the relaxation phenomena. Force relaxation at constant deformation is a typical characteristic of viscoelastic materials. As the material undergoes a change in the deformation state, both hyperelastic and viscoelastic stresses are generated within the material. However, when the deformation remains constant, the viscoelastic stress will slowly diminish and the responses will relax to the same equilibrium state. It can also be observed from the results that the peak force response of short

rise time case is larger than those of longer rise time cases. This phenomena reveals the fact that the viscoelasticity of elastomeric material is rate-dependent.

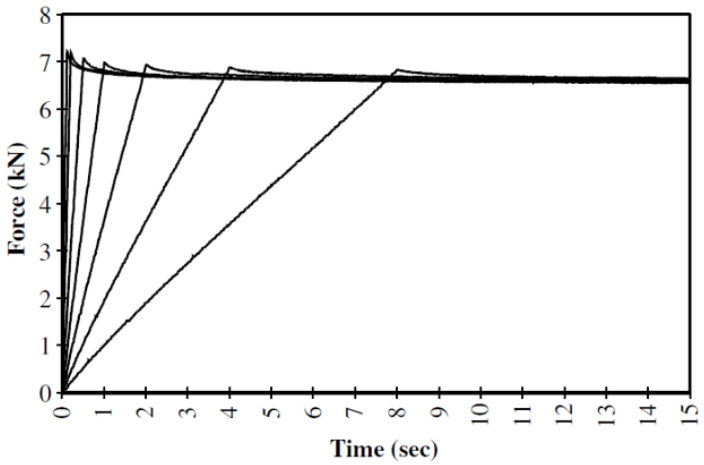

Figure 3.5. Radial force relaxation response obtained by Kadlowed [28].

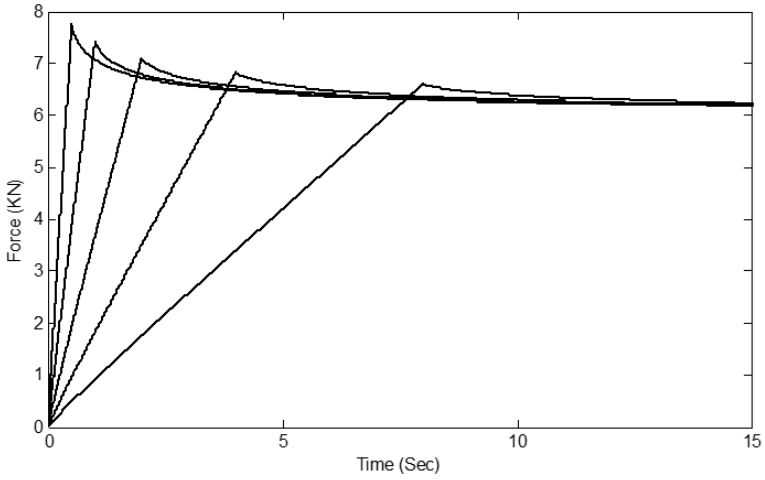

Figure 3.6. Radial force relaxation response obtained using the combined model.

The rate-dependence characteristic of elastomeric material is often evaluated using a harmonic excitation tests. Figure 3.7 illustrates the force-displacement hysteresis loops as the result of applying a radial harmonic excitation with 1.0 mm amplitude. The excitation frequencies employed were 1 Hz, 5 Hz and 10 Hz. To quantify the hysteresis loops, dynamic stiffness K_d and hysteretic damping ratio η_d are evaluated by measuring the slope of the hysteresis loop and the fraction of energy lost in each deformation cycle. The formulations are given as:

$$K_d = \frac{F_{max}}{x_{max}} \tag{3.13}$$

$$\eta_d = \frac{E_d}{\pi K_d {x_{max}}^2} \tag{3.14}$$

where F_{max} and x_{max} are the maximum reaction force and displacement, and E_d is the amount of energy loss, which is the area enclosed by the hysteresis loop. The resulting dynamic stiffness is: 8.13E+6 N/m, 9.10E+6 N/m and 9.52e+6 N/m for the 1 Hz, 5 Hz and 10 Hz cases. The hysteretic damping ratio is: 0.0742, 0.0725 and 0.0681. As the excitation frequency increases, the dynamic stiffness also increases corresponding to the larger viscoelastic stress. The damping ratio shows a slight decrease as the result of the increasing stiffness K_d.

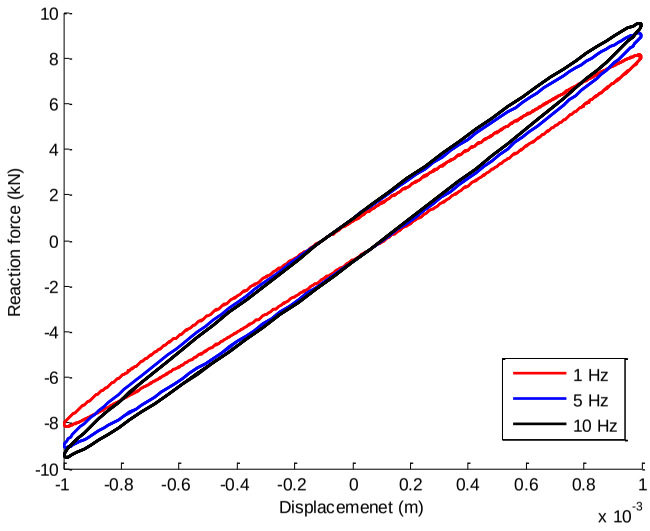

Figure 3.7. Effect of excitation frequency on the hysteresis response with 1mm harmonic displacement amplitude.

3.3.2 Elastomer Nonlinearity

Elastomers as nonlinear elastic materials, exhibits hyperelastic stress-strain relationship which is independent of material strain rate. To verify the nonlinear elasticity of elastomeric bushing, the same EFEM bushing model shown in Figure 3.4 was used in the simulation. A 1Hz radial excitation deformation was applied to the inner sleeve, and the amplitude of the excitation displacement was varied to compare the hyperelastic behaviors at small displacement and large displacement. The amplitudes used were 1mm, 2mm and 4mm. As shown in Figure 3.8, the

bushing force response is more linear in the small displacement region. The nonlinear tendency in the response becomes significant as the displacement increases. Similar elastomeric bushing nonlinear characteristics were also observed in the experimental study conducted by Ok and Yoo [48].

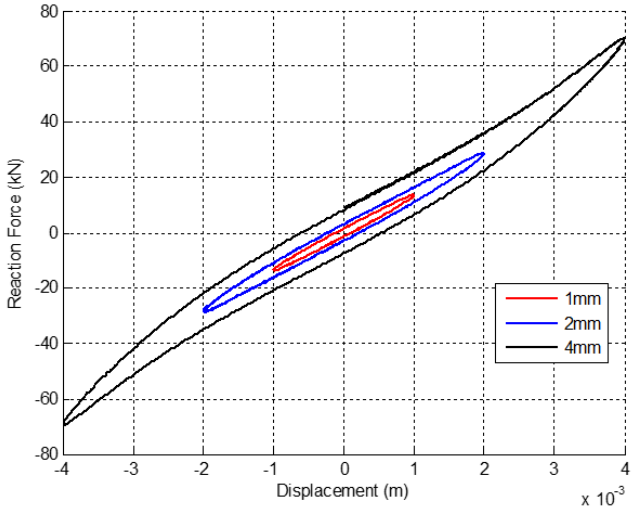

Figure 3.8. Elastomer bushing excitation deformation with various maximum displacements (1Hz harmonic deformation).

To demonstrate that the nonlinear characteristic is independent of the rate at which the deformation is applied, a radial step test was carried out for final displacements between 1 mm and 5 mm. In each step, the displacement was increased by 1 mm within 1 second, and then the displacement was held constant for 14 seconds for the force to relax to equilibrium state. Figure 3.9 shows the displacement-time history of the step test. The steady-state force was recorded at each step, and the steady-state force is represented in the dimensionless form $\bar{F}$ to account for the effects of bushing sizes and material stiffness. $\bar{F}$ is defined as:

$$\bar{F} = \frac{F}{C_R \cdot L \cdot D} \tag{3.15}$$

where C_R is material stiffness, L is bushing length and D is bushing inner diameter. The force-displacement curve is plotted in Figure 3.10 on top of the hysteresis loops of 0.1Hz and 1 Hz frequencies. It can be seen that the nonlinear tendency of the hysteresis loop follows the relaxed force-displacement curve. In the case of higher deformation rate, the viscoelastic effect will

increase the slope of hysteresis loop, however the nonlinearity of the curve is still governed by the hyperelastic property of the material.

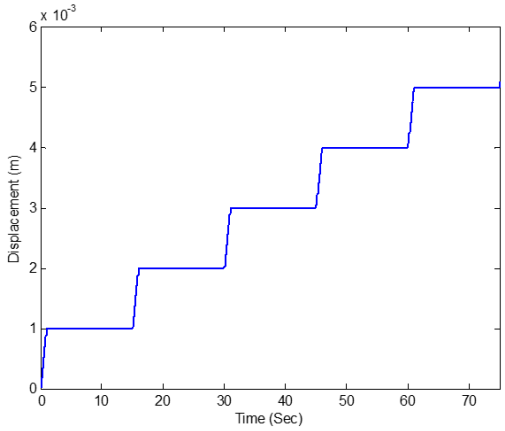

Figure 3.9. Time history of step deformation load.

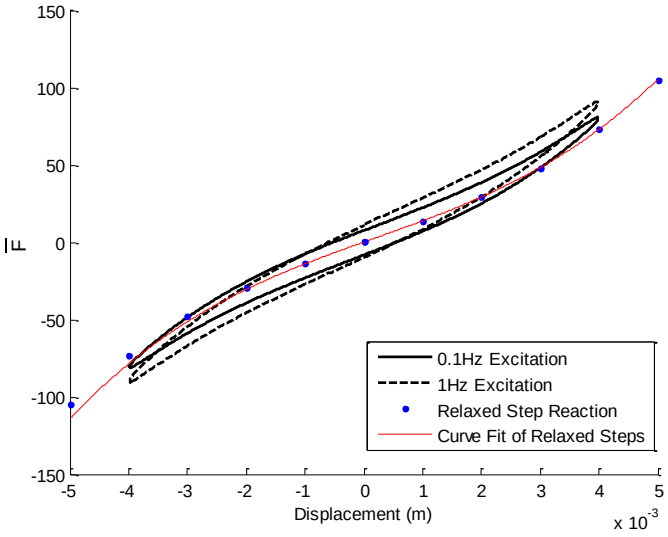

Figure 3.10. Elastomer bushing nonlinear response at large deformation for various excitation speeds on top of a relaxed state curve (red).

3.4 Results and Discussion

The combined EFEM bushing and DBM bearing model was developed to study the effects of elastomeric bushing support on bearing performance. The investigation begins with obtaining an understanding of the effect of material property and geometry on the elastomeric bushing. A parametric study on elastomeric material constants was carried out to show the relationship

between constitutive material parameters and global bushing behavior. Dimensional analysis was applied to arrange bushings of various sizes into dimensionless groups, therefore reduce the number of simulations needed on bushings with geometric similitude. The investigation was then concentrated on bearing dynamic analysis when the bearing, supported by elastomer bushing, was subject to different operational conditions.

3.4.1 Effect of Material Properties

The elastomeric material constants studied in this analysis are C_R, the material modulus and γ_j, the normalized viscoelastic constant of the Maxwell elements. The magnitude of C_R represents the stiffness of the material at continuum level, and γ_j indicates the viscoelasticity of the material. When γ_j is large, the elastomer behaves closer to a viscous material, and a small γ_j indicates that the elastomer behaves similar to a pure hyperelastic material. A harmonic radial excitation deformation was applied to the elastomeric bushing to investigate the effect of material property on bushing dynamic behaviors. The bushing under test is 40mm in inner diameter, 20mm in radial thickness and 40mm in axial length. Table 3.1 provides the elastomeric material constants which were considered as reference values. Table 3.2 lists the material groups created based on the reference values from Table 3.1.

Table 3.1. Elastomer material constants used in the constitutive model.

Material - Elastomer					
Rubber Modulus CR (MPa)					0.647
Network Locking Stretch N					8
Bulk Modulus B (MPa)					100 * CR
Maxwell Element Constants					
	γ	τ		γ	τ
j=1	0.492	10	j=8	2.304	4.92E-04
j=2	0.687	2.42	j=9	2.485	1.19E-04
j=3	1.153	0.59	j=10	2.764	2.89E-05
j=4	1.286	0.14	j=11	2.798	7.02E-06
j=5	1.804	3.46E-02	j=12	3.704	1.70E-06
j=6	1.944	8.40E-03	j=13	1.912	4.12E-07
j=7	2.116	2.00E-03	j=14	8.226	1.00E-07

Table 3.2. Materials created in parametric study in section 3.4.1.

Group 1 (Material Modulus Variation)		
2C_R	C_R	0.5C_R
Group2 (Viscoelastic Constant Variation)		
2γ	γ	0.5γ

Table 3.3. Results of bushing dynamic stiffness and hysteresis damping ratio from parametric study in section 3.4.1.

		0.1Hz		10Hz	
		K_d	η_d	K_d	η_d
Group1	2CR	3.96E+06	0.132	6.38E+06	0.155
	CR	1.98E+06	0.132	3.19E+06	0.157
	0.5CR	9.89E+05	0.132	1.60E+06	0.159
Group2	2γ	2.32E+06	0.217	4.60E+06	0.195
	γ	1.98E+06	0.132	3.19E+06	0.157
	0.5γ	1.81E+06	0.073	2.42E+06	0.11

As the result of elastomeric material damping, the hysteresis loops are obtained and plotted in Figure 3.11 for low speed (0.1Hz) deformation and in Figure 3.12 for high speed (10Hz) deformation. The dynamic stiffness and hysteretic damping ratio determined for each material group are given in Table 3.3. The results demonstrate that for the material group 1, the material modulus C_R is linearly related to the dynamic stiffness of the bushing at both high and low deformation frequencies. Variation of C_R, however, has nearly no effect on the hysteretic damping ratio. Material group 2 demonstrated that elastomers with large viscoelasticity have large hysteresis damping ratio, which also indicates significant capability of absorbing vibrational energy. The viscoelasticity also contributes to the dynamic stiffness, especially at high deformation frequencies.

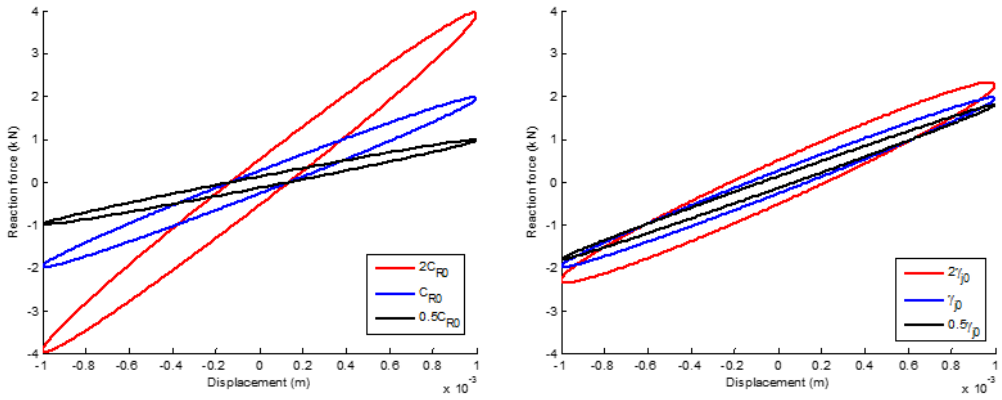

Figure 3.11. Harmonic excitation with varying material properties – 1mm excitation at 0.1 Hz.

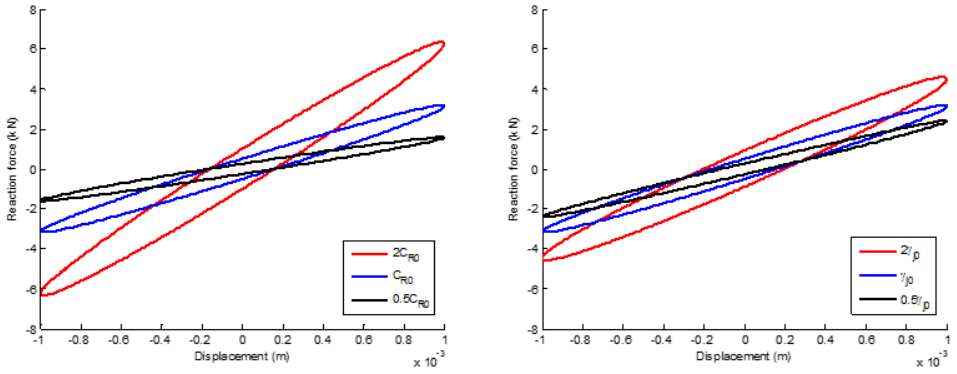

Figure 3.12. Harmonic excitation with varying material properties – 1mm excitation at 10 Hz.

3.4.2 Effect of Bushing Geometries

Choosing a proper geometry for the bushing is important to achieving the desired bushing performance. To study the effect of bushing geometries, a dimensional analysis was carried out on bushings with various dimensions. A cylindrical bushing, as shown in Figure 3.13 has three major dimensions: inner diameter D, radial thickness H and axial length L.

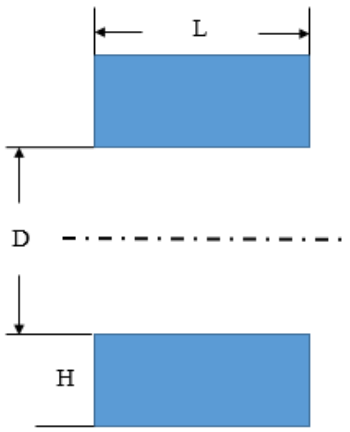

Figure 3.13. Cylindrical bushing dimensions.

Using the Buckingham Pi theorem, the dimensionless parameters are determined as

$$\bar{D} = \frac{D}{H} \tag{3.16}$$

$$\bar{L} = \frac{L}{H} \tag{3.17}$$

$$\bar{x} = \frac{x}{H} \tag{3.18}$$

where $\bar{D}$ is dimensionless inner diameter, $\bar{L}$ is dimensionless axial length and $\bar{x}$ is dimensionless radial displacement. The bushings were created with the same 20mm thickness H and inner diameter D and axial length L were varied to generate a range of different dimensionless inner diameter $\bar{D}$ and dimensionless axial length $\bar{L}$. Table 3.4 lists the 6 values of $\bar{D}$ and $\bar{L}$, and a total of 36 bushing geometries were created. A harmonic excitation deformation with 1mm amplitude and 10Hz frequency was applied to all 36 bushings. The hysteresis response of each bushing was analyzed using the hysteresis damping ratio η_d and the dimensionless dynamic stiffness $\overline{K_d}$ which is

$$\overline{K_d} = \frac{\overline{F_{max}}}{\overline{x_{max}}} \tag{3.19}$$

Table 3.4. Dimensionless length and diameter created in dimensional study in section 3.4.2.

$\bar{D}$	1	2	4	6	8	10
$\bar{L}$	1	2	4	6	8	10

Figure 3.14 and Figure 3.15 show the effect of bushing length on the dynamic stiffness and hysteresis damping ratio. The effect of bushing diameter is depicted in Figure 3.16 and Figure 3.17. It can be seen that an increase in the dimensionless axial length $\bar{L}$ will stiffen the bushing response. And the slope of the curves in Figure 3.14 indicates that such stiffening effect reduces as $\bar{L}$ becomes larger. Similar results were also obtained by Hill [11]. The reason for the stiffening effect can be explained by comparing the deformed configurations between short and long bushings, as shown in Figure 3.18. When being compressed, elastomeric material contained between the outer race and housing will expand along the directions perpendicular to the loading axis, and will cause the bulging of the end planes of the bush. For a bushing with large length, the amount of bulging has less effect and most of the elastomeric material is highly confined between the rigid bodies, and the bushing will be stiffer. Figure 3.16 demonstrates that an increase in the dimensionless inner diameter $\bar{D}$ will decrease the stiffness for short bushings but the opposite trend was observed in long bushings. The reduced radial stiffness formulation developed by Hill [11] captured similar opposite trends for long and short bushings. Effect of bushing geometries on the hysteresis damping ratio shown in Figure 3.15 and Figure 3.17 demonstrates that the combination of a small $\bar{D}$ and $\bar{L}$, which typically represents short bushing with large thickness, has large damping ratios. As $\bar{D}$ and $\bar{L}$ increase, the damping ratio reduces significantly.

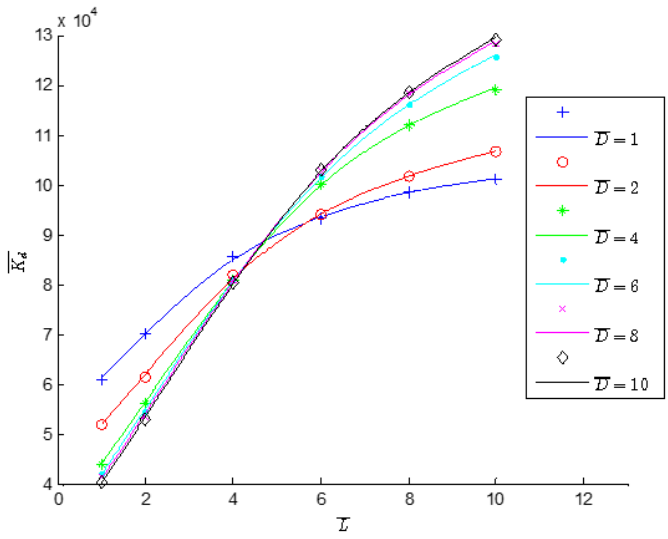

Figure 3.14. Dimensionless dynamic stiffness as a function of dimensionless length.

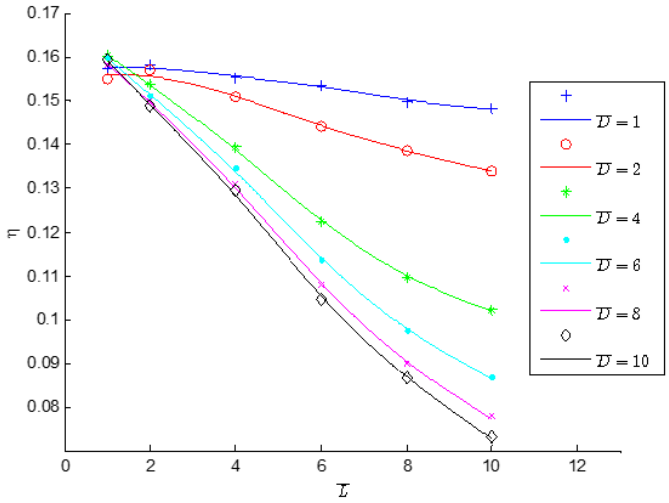

Figure 3.15. Hysteresis damping ratio as a function of dimensionless length.

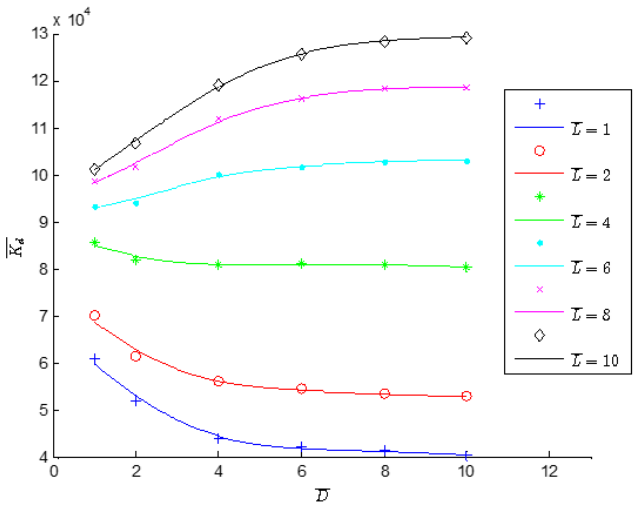

Figure 3.16. Dimensionless dynamic stiffness as a function of dimensionless inner diameter.

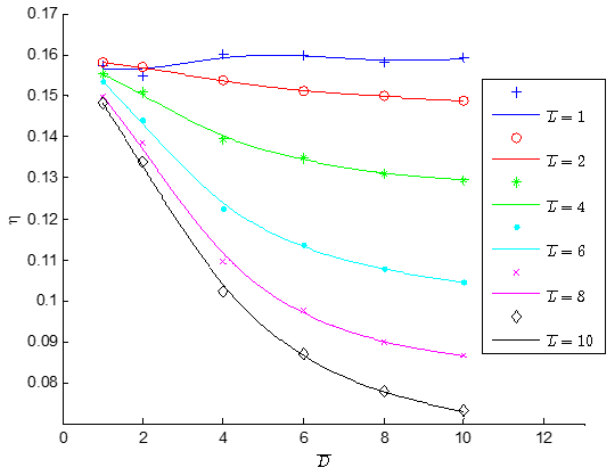

Figure 3.17. Hysteresis damping ratio as a function of dimensionless diameter.

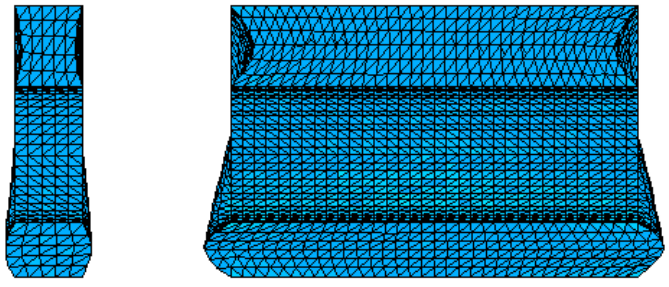

Figure 3.18. Bulging of end planes of short and long bushings.

3.4.3 Impact Loading and Rotating Unbalance

A sudden change in the loading such as an impact can cause vibration and instability in the bearing system, and elastomeric bushings are employed to absorb the vibrational energy. In this study, an impact loading as depicted in Figure 3.19 was applied to the inner race of a deep-groove ball bearing which was supported by elastomer bushing. Table 3.5 provides the major dimensions of the bearing elements. The bearing outer diameter (OD) is 71mm, and the bearing speed was set to 1000 RPM. A 5μm ball interference was created to preload the bearing.

Table 3.5. Bearing dimension specifications.

Bearing Type	Deep Groove
Number of Balls	8
IR Radii (mm)	20.047
IR Groove Radii (mm)	6.013
OR Radii (mm)	31.953
OR Groove Radii (mm)	6.310
OR Outer Diameter (mm)	71
Ball Radius (mm)	5.955
Cage Pocket Radius (mm)	6.200
Bearing Length (mm)	20

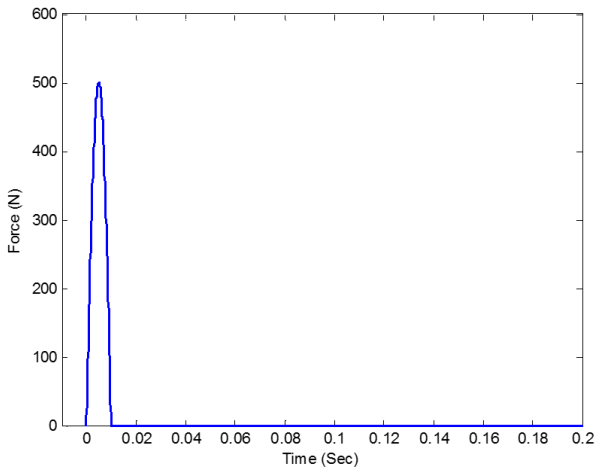

Figure 3.19. Impact load time history – 500N maximum amplitude.

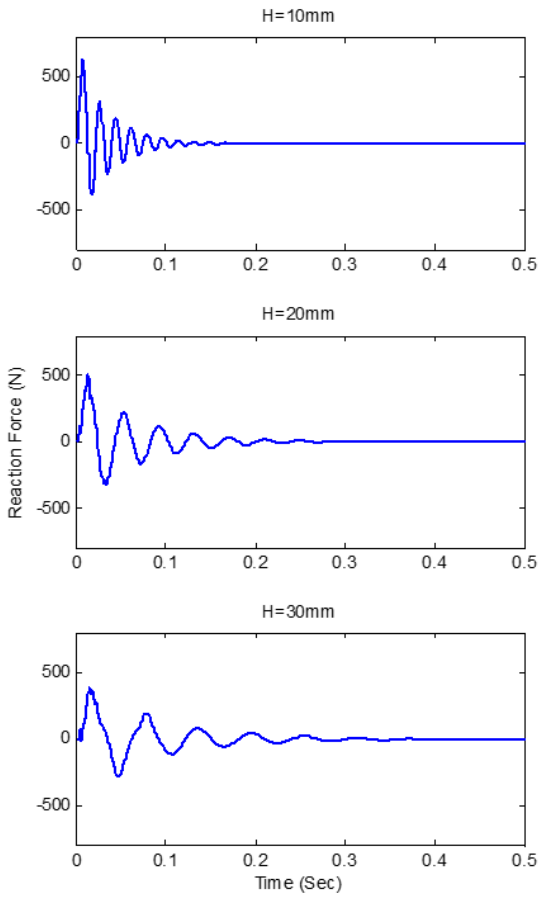

Figure 3.20. Reaction force on OR after impact for different thicknesses.

Figure 3.20 illustrates the vibration reaction force measured on the outer boundary of bushings with different thicknesses: 10mm, 20mm and 30mm. Comparison between the three responses shows that the reaction force reduced to zero faster in a thinner bushing. It should also be mentioned that the frequency of the reaction force oscillation of the thin (10mm) bushing is significantly higher. The damping mechanism of bushings with various thicknesses can be investigated using the results from section 3.4.2. With the previous dimensional analysis (Figure 3.14-Figure 3.17) and the $\overline{D}$ and $\overline{L}$ of the bushings (Table 3.6), it is found that the hysteresis damping ratios of the three bushings are approximately the same, however, the dynamic stiffness varies a lot between the three bushings.

Table 3.6. Dimensionless lengths and diameters of the bushings used in the impact study.

	Bushing Thickness		
	H=10mm	H=20mm	H=30mm
$\overline{D}$	7.1	3.55	2.37
$\overline{L}$	2	1	0.67

It is known that hysteresis damping ratio is related to the ability of energy absorption for a single vibration cycle, and dynamic stiffness affects the natural frequency of the system. Since the thinner bushing has a larger stiffness, the vibrations occurs faster to damping the unstable energy. To validate the conclusion above, the same impact study was carried out on bushings with the same thickness but different elastomer moduli C_R, so the bushing stiffness was varied by changing material properties. And similar results were obtained in Figure 3.21. Therefore in addition to choosing a proper elastomeric material, the damping capability of elastomer bushing can be tuned using the bushing geometry.

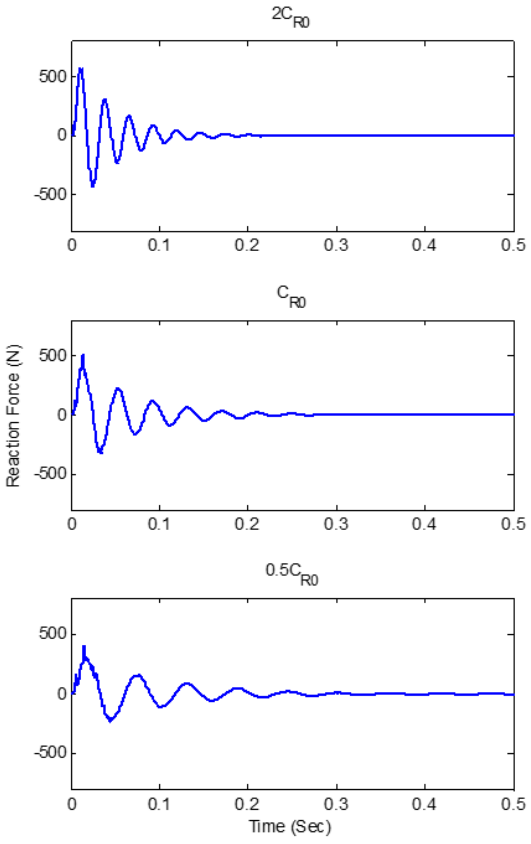

Figure 3.21. Reaction force on OR after impact for different material modules.

Rotating unbalance, which is caused by the uneven distribution of mass about the rotation axis, is also a dynamic loading that is commonly seen in rolling element bearing applications. To study the effect of elastomeric bushing on rotating unbalance, a mass eccentricity was created on the inner race. The inner race rotation speed was chosen to be 1000 RPM, and the unbalance mass and radius were chosen to generate a 100 N unbalance load at steady state. Elastomeric bushings of various thicknesses (10 mm, 20 mm and 30 mm) were used for comparison. Figure 3.22 depicts the circular orbits of inner race center of mass as the result of the rotating unbalance load. For the bushing with a thinner thickness, the radius of inner race orbit is significantly smaller. This is due to the fact that the bushing stiffness increases for a reduced thickness.

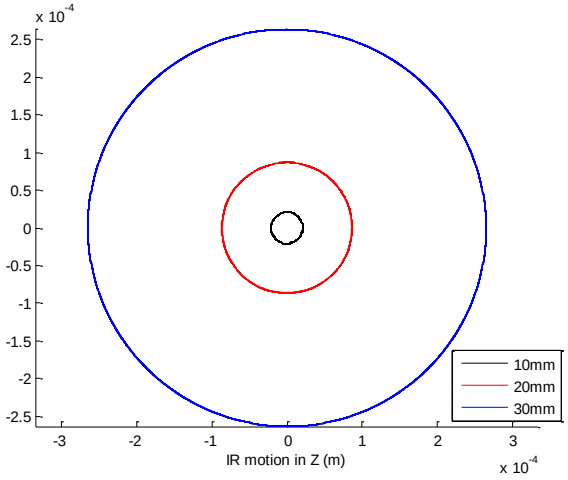

Figure 3.22. Steady state IR center of mass motions in rotating unbalance (bushing thickness: black-10mm, red-20mm, blue-30mm).

3.4.4 Vibration Reduction – Dent

Pits and dents are common occurrences in rolling element bearings. Existence of surface discontinuities will excite large vibrations within the system and shorten bearing life. A surface defect model developed by Ashtekar and Sadeghi [49] was included in the DBM to study the effect of elastomer bushing support on bearing instabilities caused by surface defect. The contact force model for a defected surface is based on

$$F = K_H {\delta_b}^n \tag{3.20}$$

where K_H is the Hertzian contact stiffness , δ_b is the relative displacement between ball and raceway surface, and n is the deflection exponent which is a function of load, dent shape and ball distance relative to the dent center. More details are given by Ashtekar and Sadeghi [49]. In this investigation, a dent with 500μm diameter was created at the bottom of outer race raceway, as shown in Figure 3.23. The same bearing described in Table 3.5 was used and the inner race speed was 100 RPM. The thickness of the elastomeric bushing is 10mm.

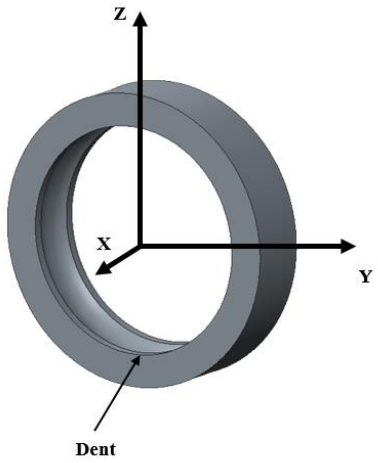

Figure 3.23. Location of dent created at the bottom of bearing outer race.

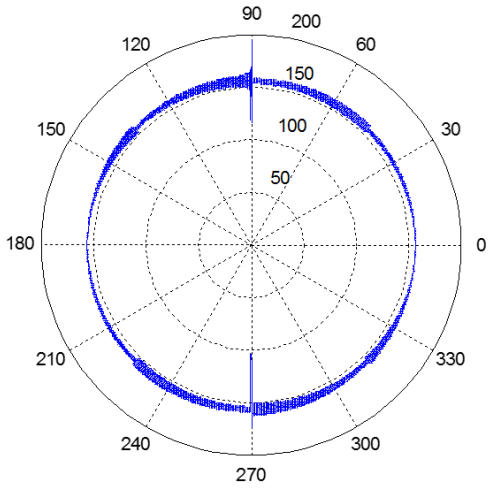

Figure 3.24. Normal contact force between ball and outer race in a bearing (fixed outer race) with dent at bottom (270 deg).

The effect of a dent on bearing dynamics is demonstrated in Figure 3.24 which shows the normal contact force between ball and a fixed outer race. The dent caused contact force fluctuations as the ball rolled over the dent, and the peak fluctuation occurred along the axis on which the dent is located. In the presence of elastomeric bushing support, however, the fluctuations (Figure 3.25) in the contact force stabilized much faster as compared to the fixed outer race case. Note that Figure 3.24 and Figure 3.25 tracked the reaction force acting on a single ball, since other balls experienced the same response.

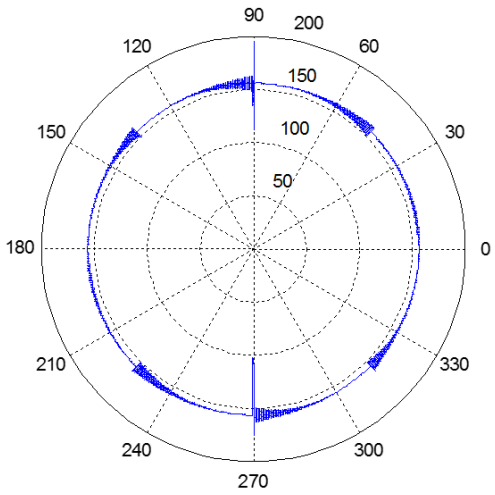

Figure 3.25. Normal contact force between ball and outer race in a bearing (outer race supported by elastomer bushing) with dent at bottom (270 deg).

As the vibrations are transmitted to the inner race, the inner race motions depicted in Figure 3.26 and Figure 3.27 show the corresponding vibrations. It can be seen in Figure 3.26 that a new impact hit the inner race before the bearing was able to damp out the previous one. And Figure 3.27 demonstrates that the bearing supported by an elastomeric bushing damped out the inner race instability more effectively and the existence of elastomeric bushing reduced the inner race maximum vibration by 67%. A Fast Fourier transform analysis (Figure 3.28) on the inner race motions shown in Figure 3.26 and Figure 3.27 also shows that the inner race vibration amplitude is significantly reduced due to the elastomeric bushing damping. When the outer race of the bearing is fixed, the friction reaction within the bearing is the major damping mechanism, and it is less effective than the viscoelastic damping in elastomer bushings.

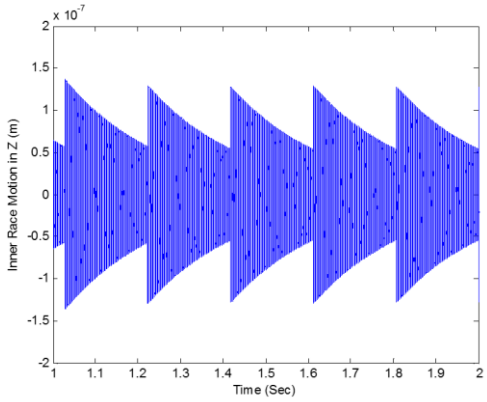

Figure 3.26. Inner race motion in Z direction in the bearing (fixed outer race) with dent (along Z direction).

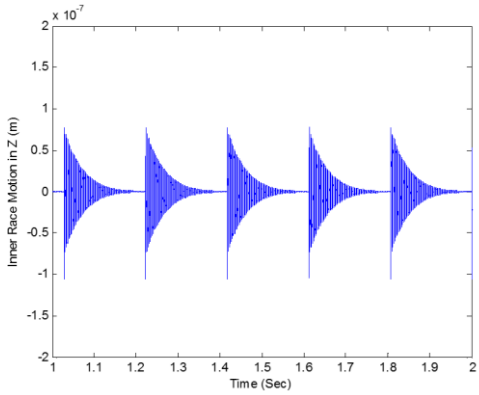

Figure 3.27. Inner race motion in Z direction in the bearing (outer race supported by elastomer bushing) with dent (along Z direction).

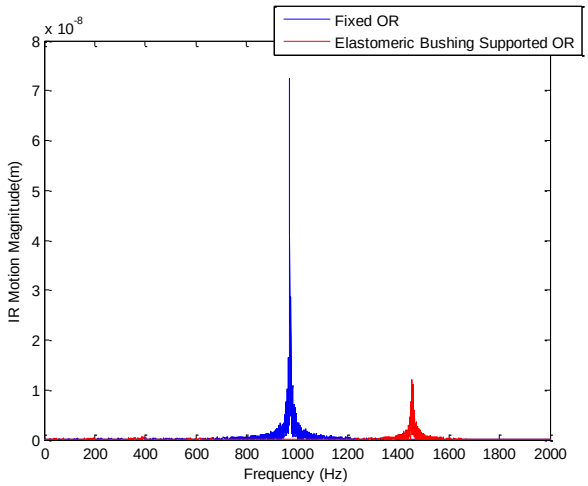

Figure 3.28. Fast Fourier transform (FFT) analysis on the IR motions plotted in Figure 3.26 and Figure 3.27.

Table 3.2 list bushing properties which were used to investigate the effect of elastomer material properties on reducing the vibrations excited by a dent. Figure 3.29 and Figure 3.30 show the ball-OR contact force for each case. It is demonstrated that a bushing with higher viscoelastic constant exhibits larger damping capability. But the damping performance of elastomeric bushing can also be improved by using a material with higher modulus, as seen in Figure 3.29. This result confirms the conclusion from the previous impact study (section 3.4.3).

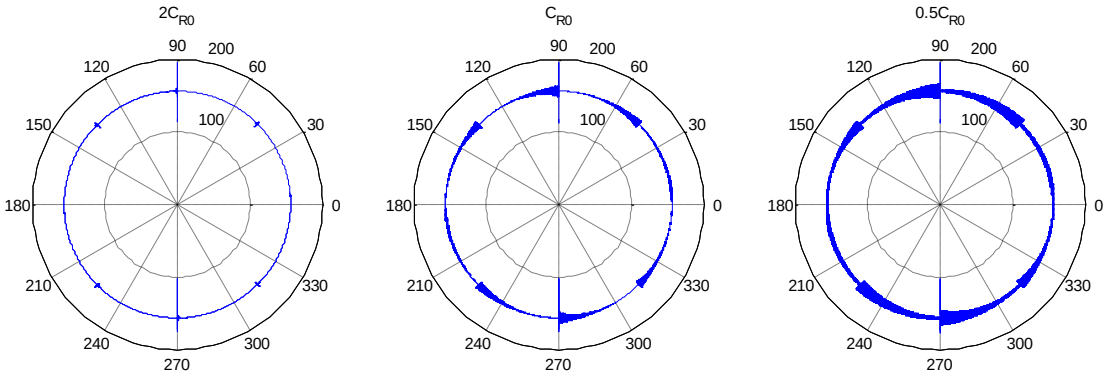

Figure 3.29. Effect of material modulus ($\boldsymbol{C_R}$) on normal contact force between ball and outer race in a bearing with dent at 270 deg.

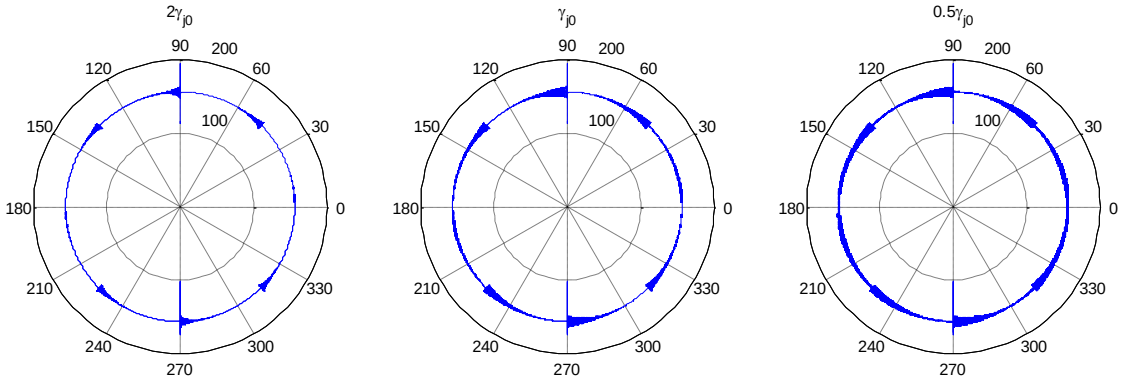

Figure 3.30. Effect of viscoelastic constant ($\boldsymbol{\gamma_{j0}}$) on normal contact force between ball and outer race in a bearing with dent at 270 deg.

3.4.5 Compliance to Angular Misalignment

Angular misalignments commonly occur in bearings. As the inner race is tilted, a moment load is generated in the bearing and results in increased reactions between bearing elements. A 0.15 degree tilt about bearing Y axis was applied to the inner races of two deep-groove ball bearings, one of which is supported by elastomeric bushing, and the other has a fixed outer race. The 0.15 degree tilt on inner races generated a 6.423 Nm angular reaction moment in the bearing with fixed outer race, and a much smaller 0.829 Nm reaction moment was generated in the bushing supported bearing.

Figure 3.31 depicts the normal contact force between the ball and outer race in polar coordinate frame as the ball rotates around the bearing. Since the inner race was tilted about Y axis, larger reactions were expected when the ball moved closer to the positive and negative Z axis (90 and 270 degrees in the Figure 3.31). It can be seen that normal contact forces due to the angular misalignment is significantly larger in the bearing with fixed outer race. Figure 3.32 illustrates the magnitude of slip between a ball and outer race at point of contact. Figure 3.33 shows the spin of the ball about the axis normal to the point of contact with outer race. The slip and spin at contact are major sources of heat generation within the bearing, and are significantly reduced by the elastomer bushing.

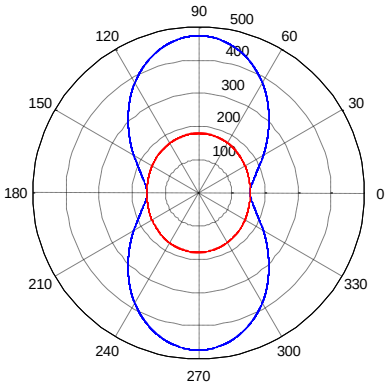

Figure 3.31. Angular misalignment test – normal contact force between ball and outer race (blue: fixed outer race, red: outer race supported by elastomer bushing).

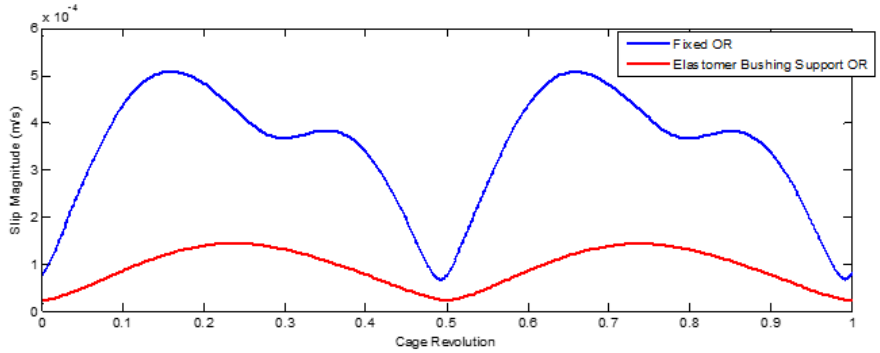

Figure 3.32. Angular misalignment test – slip magnitude between ball and outer race (blue: fixed outer race, red: outer race supported by elastomer bushing).

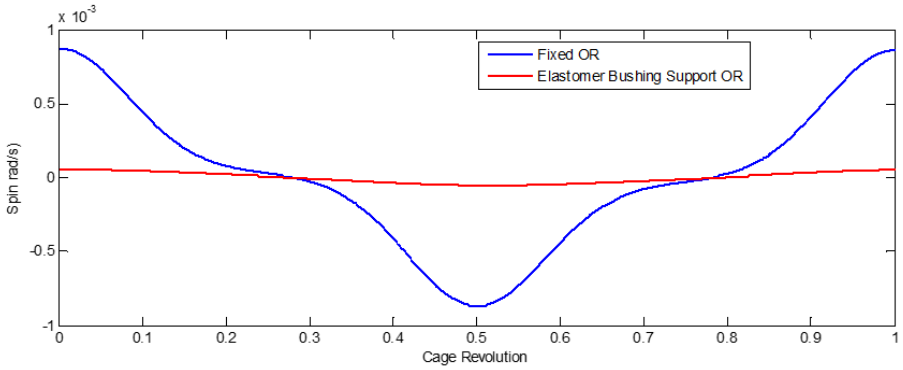

Figure 3.33. Angular misalignment test – ball spin at contact point (blue: fixed outer race, red: outer race supported by elastomer bushing).

In order to compare the compliance to angular misalignment between a fixed bearing and bushing supported bearing, a range of angular moments (2.5 Nm, 5Nm and 10Nm) were applied to the bearing inner race. Figure 3.34 illustrates the moment and tilt angle relationship for both bearings, and the slope of the curve represents the compliance of reaction moment to misalignment. The same data is tabulated in Table 3.7 which lists the tilt angles of inner race and outer race. It is shown that in a bearing with fixed outer race, only the inner race is tilted due to misalignment. However, in the bearing supported by elastomer bushing, the outer race also tilts due to the misalignment and effectively reduces the reactions occurring between the two races. Note that in the bushing supported bearing, the angle difference between the two races is exactly the same as angle difference in the fixed bearing (OR tilt angle is zero). The angle difference between the inner and outer races determines the magnitude of angular moment.

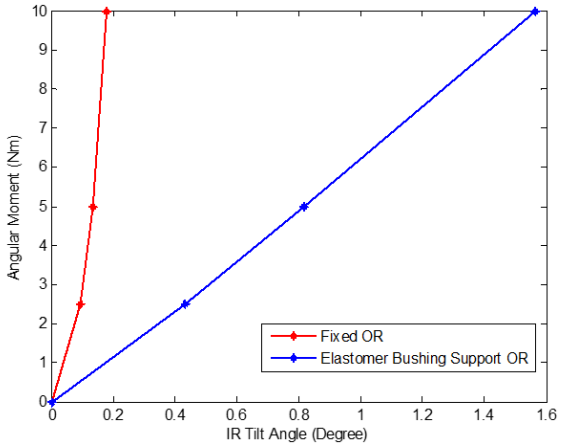

Figure 3.34. Comparison of moment-angle curve between bearings with fixed outer race and bushing supported outer race.

Table 3.7. Tilt angle of bearing races due to applied moments.

	Fixed Bearing	Bushing Supported Bearing		
	IR (Degree)	IR (Degree)	OR (Degree)	Difference(IR-OR)
2.5Nm	0.094	0.433	0.339	0.094
5Nm	0.134	0.815	0.681	0.134
10Nm	0.175	1.560	1.385	0.175

3.5 Conclusions

In this chapter a new EFEM bushing model has been presented that allows for investigations of the effect of elastomeric bushings on bearing dynamics. Results of the proposed elastomeric bushing model show good agreement with the existing experimental work. It is further shown that the model can successfully simulate the expected dynamic performance of elastomeric bushings for various material properties and bushing geometries, however further experimental validation is necessary in future work.

CHAPTER 4. A COMBINED EFEM-DEM DYNAMIC MODEL OF ROTOR-BEARING-HOUSING SYSTEM

4.1 Introduction

In this chapter, a flexible rotor, bearing and support system model was developed using discrete element (DE) and finite element (FE) methods. The model investigated the effects of housing and rotor flexibility and analyzed the dynamics and interdependence of the various components in the system. The existing DEM bearing model [4], the EFEM rotor model [39] and the EFEM housing model [43] were used in the combined DEM-EFEM dynamic model. New approaches were developed to improve the contact algorithms between the components and the EFEM method was modified with the Total Lagrangian formulation method to increase the computational efficiency and robustness of the model. Each bearing element (i.e. IR, OR, rollers and cage) has 6 DOFs, and the EFEM components (i.e. rotor and housing) can be modeled using any desired geometry. Most of the previous researchers have studied the bearing, rotor, and support systems individually without the complex interaction between the components. However, these components are interdependent on each other in a real rotor-bearing-system, and the combined model developed for this investigation addresses the intricacies in the behavior of the system. In this paper, results are presented to discuss the effects of housing and bearing internal clearances on bearing vibration and housing deformation. The critical speed of rotor is also studied to show the effects of rotor and housing flexibilities on bearing performance.

4.2 Model Description

Figure 4.1 illustrates the flowchart of the combined rotor-bearing model, which is composed of a dynamic bearing model, EFEM rotor and EFEM housing. As can be seen in the flowchart, the models for the three parts work in parallel with each other during simulation. In each time step, contact reactions between each pair of coupled models are detected and solved. Contact forces and moments are then applied to the contacting parts and integrate in time to obtain the new state of motions for the next step. In the next few sections (4.2.1 – 4.2.4), the model of each part and the contact algorithms are described in details.

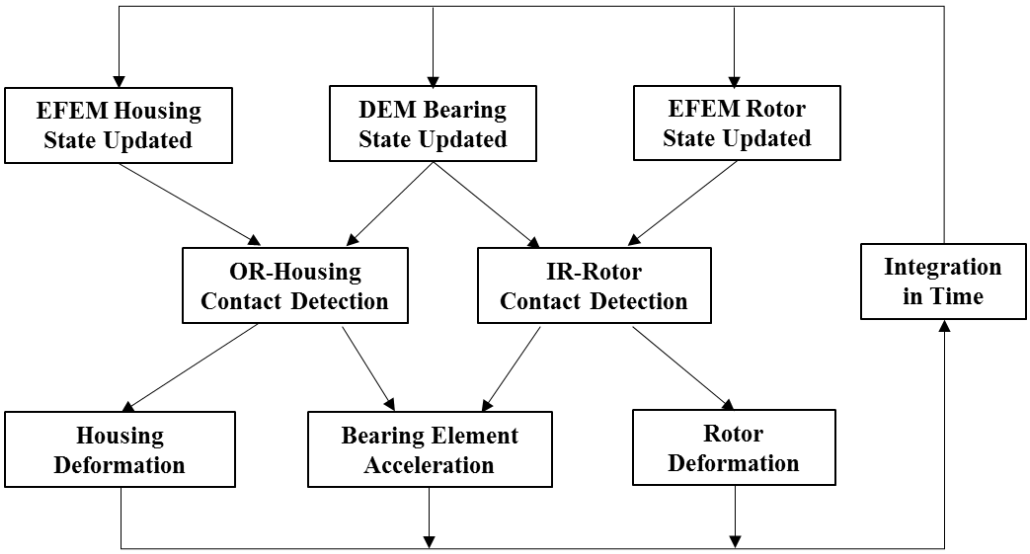

Figure 4.1. Flowchart of combined EFEM-DEM Rotor-Bearing Model.

4.2.1 Dynamic Bearing Model

The dynamic bearing model (DBM) is used for the dynamic analysis of ball bearings. DBM is based on the discrete element method (DEM), which assumes each of the bearing elements (i.e. balls, cage, inner race, and outer race) to be rigid body with six degrees of freedom in a three dimensional space. The dynamic motion of bearing element depends on the external load/moment applied as well as the contact reactions between bearing elements. For a full description of the model, please refer to Saheta [4].

4.2.1.1 Reaction Forces and Moments

The normal contact force is determined by the geometric interaction between two rigid elements. As shown in Figure 4.2, the overlap δ can be calculated according to the distance between the centers of the two elements. When overlap is detected, the force-deflection relationship for Hertzian contact is used to find the corresponding normal force, which will be applied to both elements. The Hertzian force-deflection relationship is given by:

$$F_n = k \cdot \delta^{3/2} \tag{4.1}$$

where F_n is the normal reaction force, and k is the Hertzian contact stiffness, which is a function of the element geometries as described by Hamrock et al. [45].

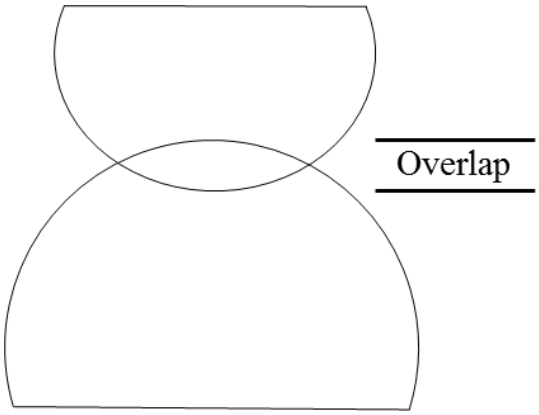

Figure 4.2. Overlap between two bodies in Hertzian contact.

The traction force at the contact is calculated as the product of the normal force and friction coefficient. In this model, the friction coefficient is determined by the relative slip velocity between the two elements in contact. A description of the friction-slip relationship is described by Weinzapfel and Sadeghi [10].

The reaction moments are then determined by the cross product of the force vector and the vector between the contact point and element center. It should also be noted that a contact spin torque due to the variation of slip velocity within the contact region is considered in DBM.

4.2.1.2 Integration Algorithm

The position of a bearing element is specified in the Cartesian coordinates of the inertial frame, and the orientation of the bearing element is defined using the Euler angle sequence in the body-fixed frame. Therefore, the net forces and moments are summed up in the inertial frame and body-fixed frame respectively. The translational and rotational equations of motion are integrated in time using the 4th order Runge-Kutta method to solve for the dynamic motions.

4.2.2 EFEM Rotor and Bearing Housing

The flexible rotor and bearing housing are modeled with tetrahedral elements using the EFEM described by Ashtekar and Sadeghi [9]. The rotor model was modified with the Total Lagrangian formulation [46] to achieve significantly higher numerical efficiency.

The deformation gradient of the finite element is given by;

$$\boldsymbol{F}_{ij} = \boldsymbol{\delta}_{ij} + \sum_{n=1}^{4} \frac{\partial N^n}{\partial X^j} u_i^n \tag{4.2}$$

where u is the displacement of the node, X is the coordinates of the node in the initial configuration, N is the shape function of tetrahedral element, and $\boldsymbol{\delta}$ is the Kronecker delta. Please note that in the previous formulation [39, 9], the derivatives of the shape function with respect to the nodal coordinate were evaluated in the current deformed configuration, therefore these derivatives had to be re-computed at every time step. In the Total Lagrangian formulation, however, these derivatives only need to be evaluated once in the initial configuration and thus significant amount of mathematical operations was saved during the simulation. Deformation of the elements is then calculated using the Right Cauchy-Green deformation tensor

$$\boldsymbol{C}_{ij} = \boldsymbol{F}^T \boldsymbol{F} \tag{4.3}$$

Using the deformation tensor $\boldsymbol{C}_{ij}$, the Lagrangian strain tensor can be evaluated

$$\boldsymbol{E}_{ij}^L = \frac{1}{2}(\boldsymbol{C}_{ij} - \boldsymbol{\delta}_{ij}) \tag{4.4}$$

Then the second Piola-Kirchhoff stress is determined using

$$\boldsymbol{S}_{ij} = \frac{E}{1+v}(\boldsymbol{E}_{ij}^L + \frac{v}{1-2v} tr(\boldsymbol{E}_{ij}^L)\boldsymbol{\delta}_{ij}) \tag{4.5}$$

where v is Poisson ratio and E is Young's modulus. The second Piola-Kirchhoff stress $\boldsymbol{S}_{ij}$ is used to calculate the nodal force in the undeformed configuration

$$\boldsymbol{f_0} = (\boldsymbol{S}_{ij} \cdot \boldsymbol{n_0}) \cdot A \tag{4.6}$$

with A being the face surface area and $\boldsymbol{n_0}$ being the face outward normal. $\boldsymbol{f_0}$ is then converted to the traction force $\boldsymbol{f}$ in the deformed configuration following a push-forward operation using the deformation gradient tensor

$$\boldsymbol{f} = \boldsymbol{F} \cdot \boldsymbol{f_0} \tag{4.7}$$

The traction force is equally distributed over all the nodes on each face to calculate the total nodal force. The equation of motion for each node is integrated in time to determine the new

positons and velocities. This process is repeated for each element within the mesh, therefore the configuration of the mesh is continuously updated at each time step.

4.2.3 DBM-Rotor Contact

In this model, the inner race (IR) of each bearing is fixed on the flexible rotor. Therefore, it is required that the six DOFs of the IR match the DOFs of the rotor cross section where the bearing is located and thus a contact algorithm was developed to fulfill this requirement.

4.2.3.1 Coupling of Translational DOFs

In the EFEM rotor model developed by Brouwer and Sadeghi [39], the 3 translational motions of the IR of the bearing were specified by fixing the center of IR to the center node of the rotor cross section. Although this method is mathematically simple, it causes an infinitely large contact stiffness between the IR and rotor center node. This large contact stiffness will result in instability and convergence difficulty. Especially when the OR is not fixed to ground as is the case of this study.

To improve the IR-rotor contact model, the three translational motions of the IR and rotor are coupled using the penalty method, in which the contact force is proportional to the displacement between the center of IR and the center node of the rotor cross section (at bearing location). The objective of the penalty method is to minimize the relative distance between the IR and rotor, therefore the solution becomes more accurate with a larger penalty stiffness. In this study, a penalty stiffness of 2e9N/m was used, and the centers are connected by a spring which represents the contact stiffness. The contact force is applied to the center of IR and distributed equally to the nodes on the rotor cross section. A small damping term (represented by the dashpot) is also used to minimize the oscillating motions between the two bodies.

4.2.3.2 Coupling of Rotational DOFs

The rotational DOFs of the IR are specified according to the orientation of the rotor cross section, since the IR is considered to be fixed on the rotor. To achieve this, the orientation of the rotor cross section is identified by calculating the three Euler angles (η, ξ, and λ) with respect to the inertial reference frame, as shown in Figure 4.3. Details of the numerical procedure are described by Brouwer and Sadeghi [39]. The three reaction moments, which counter the

rotations of the IR, are in return transferred to the rotor about body-fixed axes. Each reaction moment is applied by adding coupled forces to coupled nodes of the cross section about the body-fixed axis.

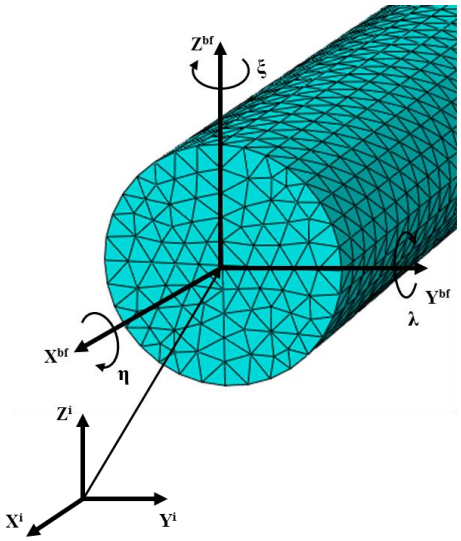

Figure 4.3. Euler angles of rotor cross-section between body-fixed frame and inertial frame.

4.2.4 DBM-Housing Contact

In this study, the housing is modeled as a flexible body while the bearing OR is considered rigid body, therefore a rigid-flexible contact algorithm was developed to evaluate the contact forces between the two bodies.

4.2.4.1 Normal Contact Force

The algorithm developed by Cao et al. [43] is used to determine the normal contact interaction. The contacting surfaces are the outer surface of the rigid OR and the inner surface of the EFEM housing. Normal contact force between the two bodies is evaluated using the penalty method, and the magnitude of the normal contact force is proportional to the amount of interpenetration at contact location as shown in Figure 4.4. Radial distance between the OR central axis and each node on the housing inner surface is calculated in the OR body-fixed reference frame. When the radial distance d is less than the outer radius of OR, then the node is considered to be in contact with the OR. And the normal contact force between node A and OR can be calculated by

$$\boldsymbol{F}_n^{bf} = (R_{OR} - d) \cdot K \cdot \boldsymbol{n} \tag{4.8}$$

where K is the contact stiffness constant and $\boldsymbol{n}$ is the outward unit normal to the OR surface. In this model, $K = 2.5e8\ N/m$ was used for OR and housing contact. The contact force is then applied to both OR and housing as external forces.

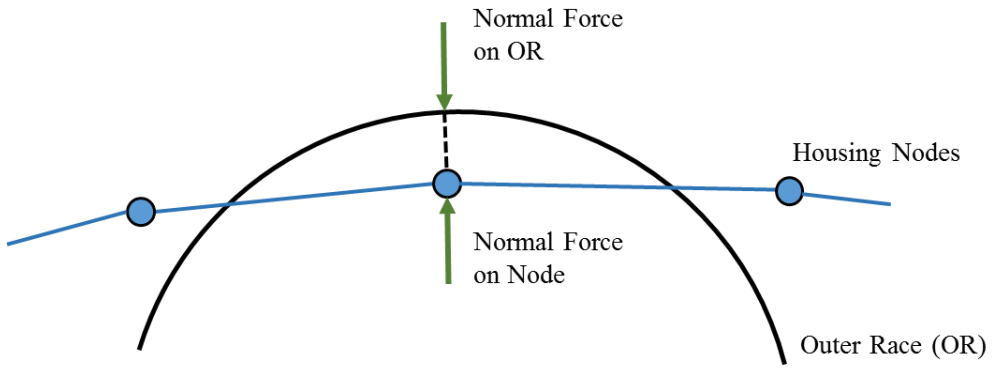

Figure 4.4. The interaction between rigid and flexible bodies.

4.2.4.2 Frictional Contact Force

Since the rotor flexibility was not included in the model developed by Cao et al. [43], only radial interaction between the bearing and EFEM housing was investigated. Also, the 6 DOFs of the bearing OR was reduced to 5 in order to improve the numerical efficiency. In this combined rotor-bearing-housing model, however, the bearing OR needs to have 6 DOFs because reaction forces and moments can occur in all directions. Therefore, the frictional interaction between the bearing OR and housing surface was added to the OR-housing contact model.

Friction is calculated between the two opposing surfaces using the Coulomb friction law. The friction force vector is in the tangential direction at the contact on the OR surface. The magnitude of the friction is the product of the normal force and a friction coefficient. To determine the friction coefficient, a spring is attached between housing inner surface nodes and OR outer surface. In the stick condition, the spring stretches elastically and the friction coefficient increases linearly with the length of the spring. A large penalty term is used for the stiffness of the spring so that the tangential displacement is minimized in the stick condition. When the friction coefficient has reached the slipping point, the coefficient remains constant. In this study, the slipping point friction coefficient is chosen to be 0.6.

4.3 Results and Discussion

The combined EFEM-DEM dynamic model of rotor-bearing system was used to investigate the rotor dynamics and bearing behavior under various operating conditions. Figure 4.5(a) depicts the rotor-bearing system modeled in this study. An EFEM rotor is supported on both ends by deep-groove ball bearings and EFEM pillow block housings. The dimensions and material properties of the rotor and bearing components are listed in Table 4.1. Figure 4.5(b) illustrates the model for a pillow block housing, the bottom of which is fixed to ground. In the following sections, results are presented to show the effects of bearing and housing clearances on the dynamic performance of the rotor system. The study also investigates the rotor-bearing system under both constant radial load and rotating imbalance load conditions.

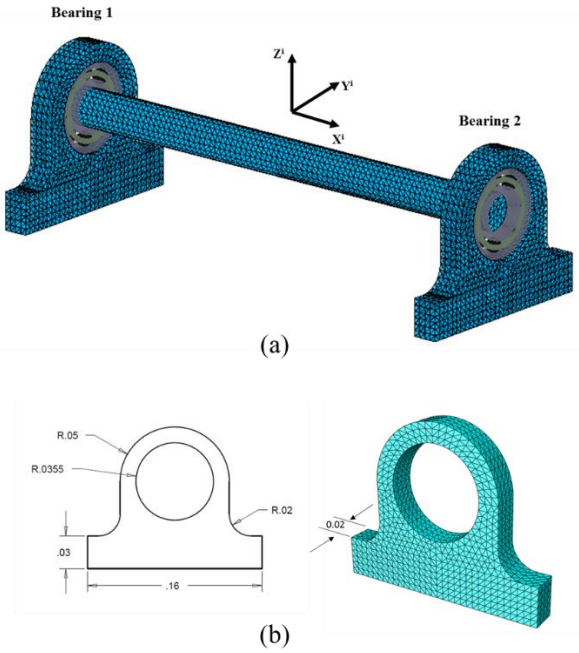

Figure 4.5. (a) Initial state of combined EFEM-DEM dynamic rotor-bearing model, (b) Dimensions (in meter) of pillow block bearing housing and EFEM mesh.

Table 4.1. Ball bearing and rotor characteristics.

Deep-groove Ball Bearing	
Number of Balls	8
IR Radii (mm)	20.047
IR Groove Radii (mm)	6.013
OR Radii (mm)	31.953
OR Groove Radii (mm)	6.310
Ball Radius (mm)	5.953
Cage Pocket Radius (mm)	6.200
EFEM Rotor	
Length (mm)	400
Diameter (mm)	30
Modulus of Elasticity (GPa)	210
Poisson's Ratio	0.3
Density (kg/m^3)	7850
Mass Proportional Damping coefficient (1/s)	100

4.3.1 Effect of Bearing Clearance

Bearing radial internal clearance is defined as the distance through which the inner race can move in the radial direction without generating a contact force with the balls. The internal clearance can change due to the thermal expansion of bearing components during operation, and it will affect the bearing vibration, contact forces and reaction moments, and eventually has an impact on bearing life. Although thermal effect is not included in the current model, the effect of bearing internal clearance can still be investigated by varying the size of the balls. Four different internal clearance cases are modeled: +5μm (clearance fit), 0μm (transition fit), -5μm and -10μm (interference fit). The housing bore clearance is 0μm (transition fit) for all three cases. The rotor speed is increase from 0 to 1000rpm and a constant radial load of 3000N is applied at the rotor center in the –Z direction. Note that since the configuration of the rotor-bearing system is symmetric about the Y-Z plane (across rotor middle cross-section), only results of Bearing 1 in Figure 4.5 are presented here.

Figure 4.6 shows the varying compliance (VC) motions of IR in the Z direction, and Figure 4.7 shows the VC motions in the Y direction. Varying compliance is an inherent feature of bearing dynamics, and the motion varies with the angular positions of the balls. The results in Figure 4.6 and Figure 4.7 demonstrate that as the radial internal clearance decreases, the amplitude of the VC vibration reduces accordingly. This is related to the change of the overall bearing support stiffness, which can be seen in Figure 4.8. The configuration of the bearing under radial load is shown for each clearance case. The balls which are in contact with the IR are shown in red, and the arrows are mapped to the magnitude of the normal force between the race and the ball. It can be seen that with the decrease of internal clearance, the number of balls supporting the radial load increases and so does the area of the loading zone. In the -10μm interference case, the race is in contact with all the balls; therefore the motion of IR is secured in all directions. This explains the significant reduction in the amplitude of VC.

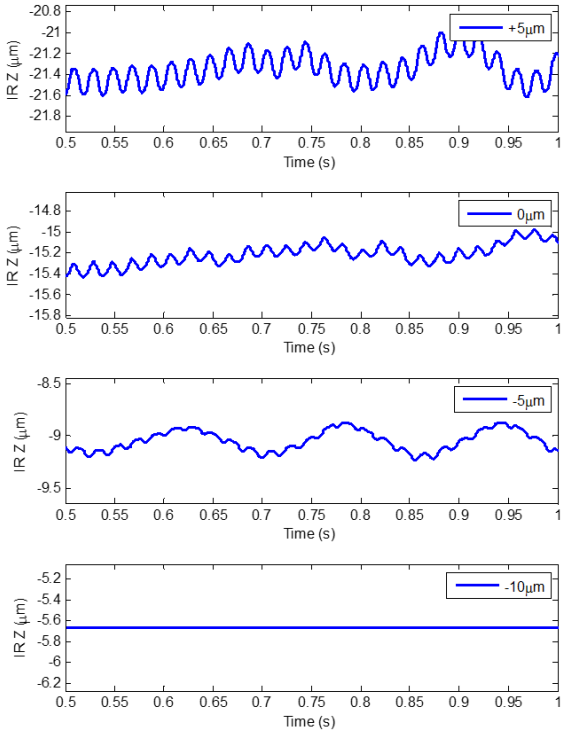

Figure 4.6. Comparison of bearing IR varying compliance motions in Z direction between four different bearing clearance cases.

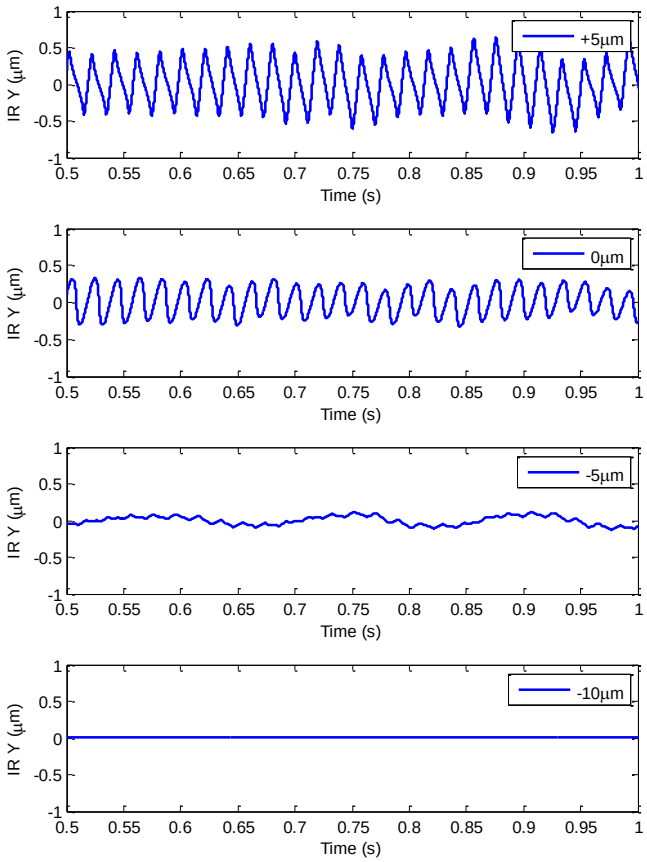

Figure 4.7. Comparison of bearing IR varying compliance motions in Y direction between four different bearing clearance cases.

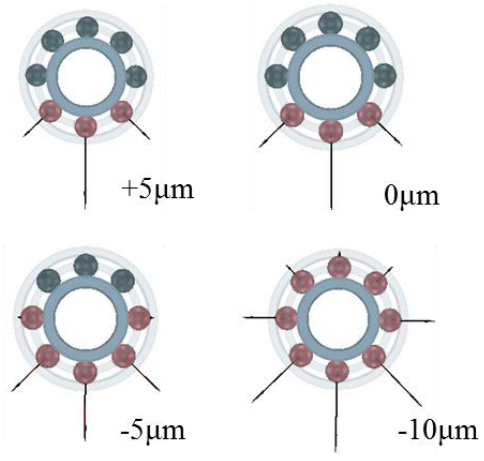

Figure 4.8. Illustration of contact force between balls and OR under radial load.

An interference fit, however, may not be preferred since large reaction force/moment will be generated within the bearing as a result of rotor deformations. Figure 4.9 depicts the simulation results for the rotor-bearing system under a radial load. Increased stresses are shown at the rotor center where the radial load is applied and at the bottom of the EFEM housings where reaction forces are generated to support the rotor. The external load and reaction forces cause deformation of the rotor, and also result in misalignment at bearing locations, as seen in the deformed configuration of rotor in Figure 4.10. Figure 4.11 shows the bearing cross-section in the X-Z plane to demonstrate the interactions between bearing components due to the loading and misalignment. As the IR tilts following the rotor, the contact angle β between the ball and race also changes. So the normal force components in the X direction F_{x1} and F_{x2} will generate a moment about bearing center to counteract the tilt angle α. The sum of F_{x1} and F_{x2} also generates a reaction force in the axial direction. The sum of force components in the Z direction will be the reaction force to balance the external load. It should be noted that as the size of the ball increases (clearance decreases) the normal force between the ball and race increases as well, and results in a larger reaction moment. Figure 4.12(a) shows the polar plot of the normal reaction force between the ball and OR. And Figure 4.12(b) shows the comparison of reaction moment as the tilt angle α increases, and this phenomenon was also demonstrated by Brouwer and Sadeghi [39]. The variation of reaction moment also has an effect on the deformation of housing, which will be explained in a later section (4.3.3).

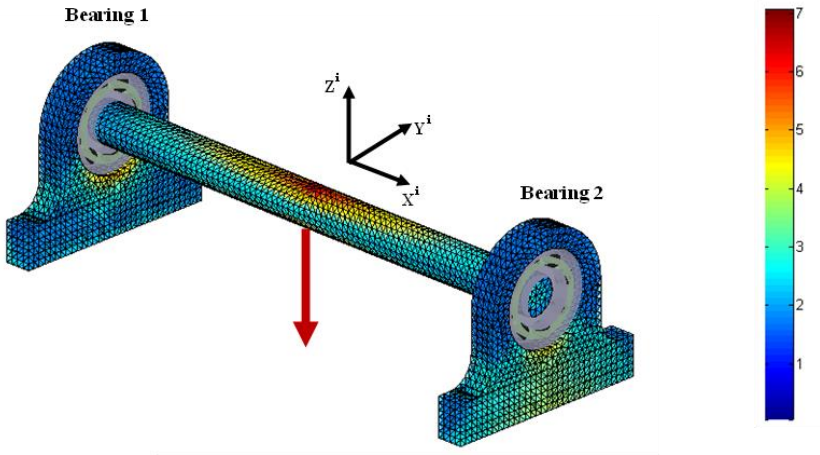

Figure 4.9. The combined rotor-bearing model with radial load applied at rotor center (von Mises stress in MPa shown in the figure).

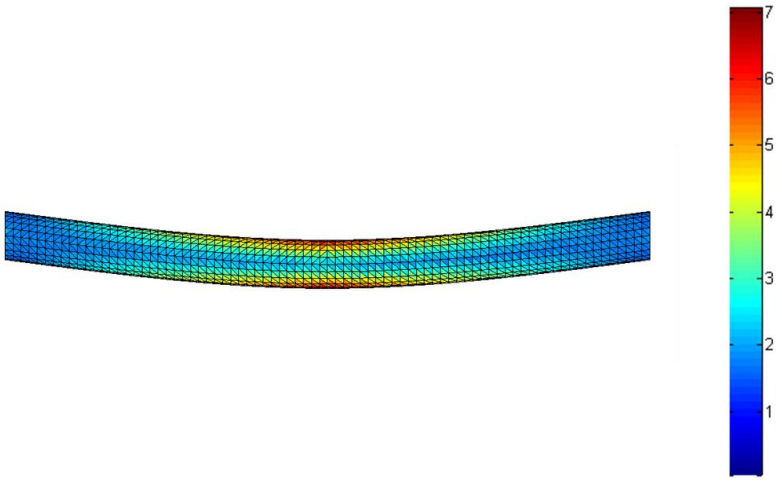

Figure 4.10. Deformed configuration of EFEM rotor (deformation * 40, von Mises stress in MPa shown in the figure).

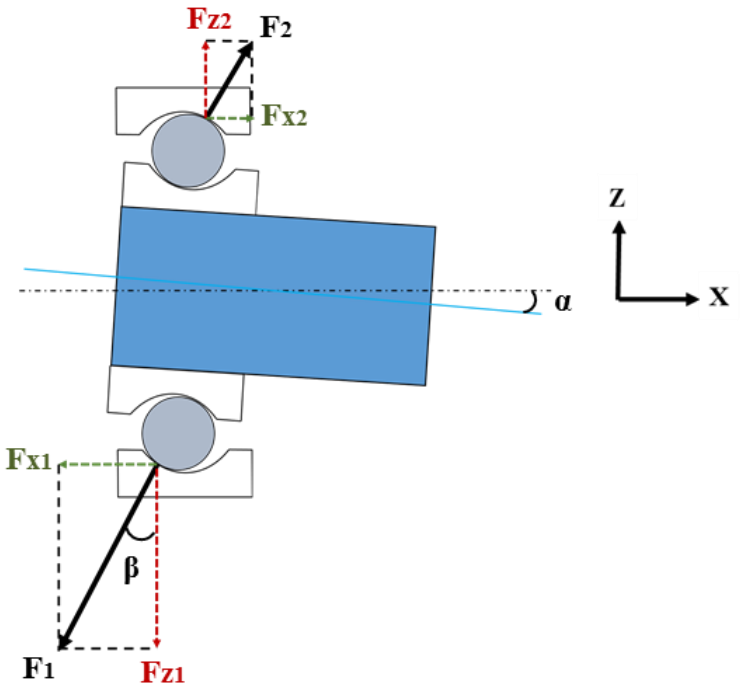

Figure 4.11. Cross-section view of contact forces between balls and bearing race under radial load and rotor misalignment.

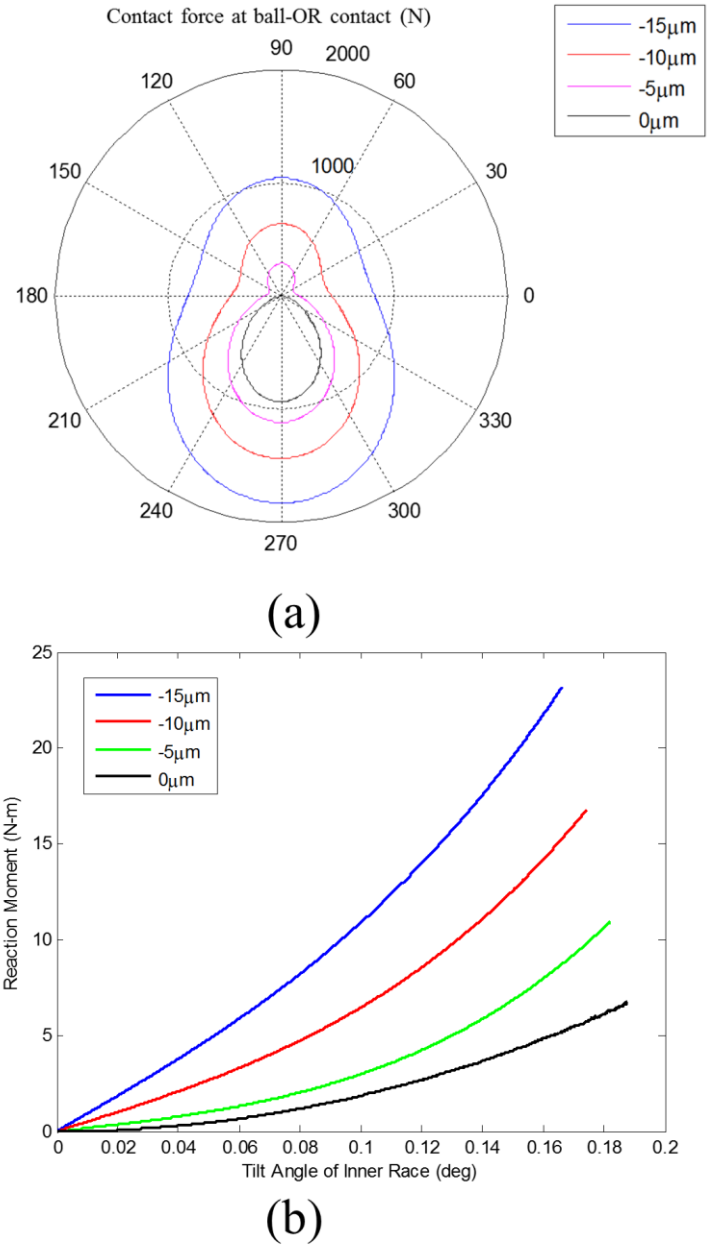

Figure 4.12. (a) Normal contact force between one ball and OR as the ball moves around the OR, (b) Reaction moment in the bearing as a function of the tilt angle of bearing IR..

4.3.2 Effect of Housing Clearance

The clearance between the housing bore and bearing OR can significantly influence the housing support characteristics. Cao el al. [43] have shown that the housing support stiffness is dependent on the housing clearance. In this section, the effect of housing clearance on bearing vibration is studied. The steady state rotor speed is 1000rpm and a 3000N load is applied to the rotor center. Three housing clearance cases are studied for comparison: +5μm (clearance fit), 0μm (transition fit) and -5μm (interference fit). In all three cases, the bearing internal clearance is 0μm (transition fit).

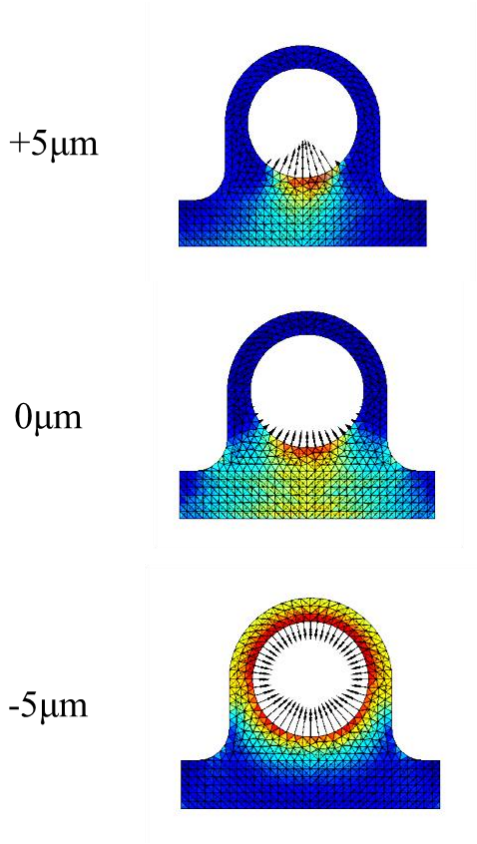

Figure 4.13. Contact force distribution between bearing OR and housing for housings with various clearance.

Figure 4.13 shows the deformed pillow block housing support after the load was applied to the bearing for each of the clearance cases. The distribution of nodal contact forces between the bearing OR and housing is indicated by the black arrows. It can be seen in Figure 4.13 that the housing clearance has a large effect on the contact area between bearing and housing. A

clearance fit results in a less conformal contact, and the bearing is only supported by a small area on the housing in the loading direction. In this case, the support stiffness in the Y-axis direction is significantly reduced. As the clearance reduces, contact becomes more conformal. The effect of the contact between bearing OR and housing is seen in the VC motion of IR. Figure 4.14 shows the IR motion in the Y direction. In the clearance case, since the bearing is not supported in the tangential direction (along Y axis), the VC motion can result in instabilities such as fretting wear or fatigue between the contacting bodies. It is therefore critical to choose a proper housing clearance so that the bearing can remain supported in all directions during operation.

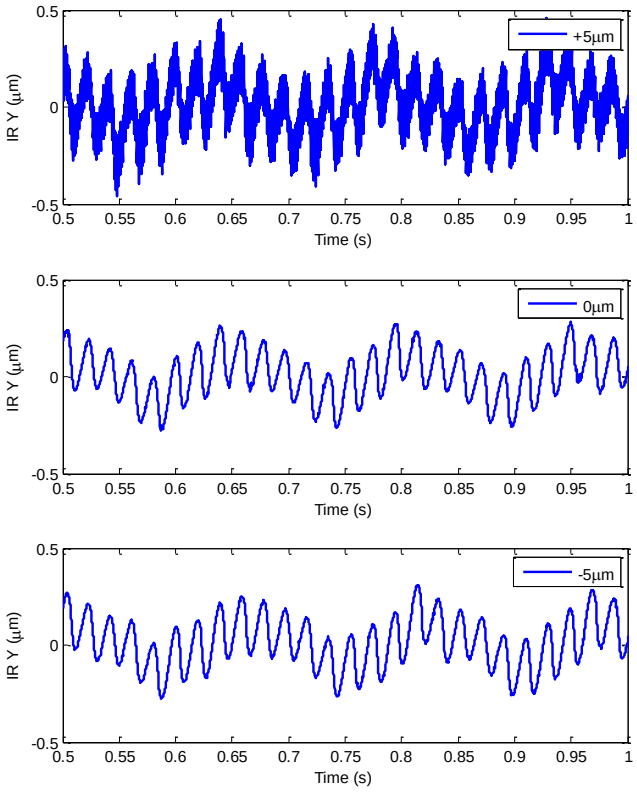

Figure 4.14. Effect of housing clearance on the IR varying compliance motions in Y direction.

4.3.3 Housing Deformation

It was shown previously that rotor deformation generates reaction force and moment within the ball bearing. These reactions will also act on the bearing support through the interaction between OR and housing. However, bearing models published previously commonly assumed that the

OR is fixed in space, and neglected the behavior of bearing support. In this investigation, a more realistic flexible housing model is included, and the housing deformation is investigated.

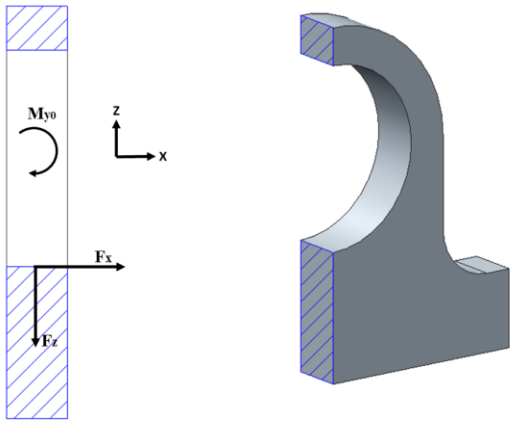

Figure 4.15. Cross-section view of bearing housing free-body diagram.

In the case of a radial load on the rotor center in Figure 4.5, bearing housing is deformed under compression in the loading direction, but housing is also subject to bending due to the moment and axial reaction force as shown in sec 4.3.1. Figure 4.15 shows the free-body diagram of the forces and moment acting upon the housing. M_{y0} is the reaction moment from the bearing and F_x is the axial traction force acting on the housing bore where the OR is compressed against. The housing bore has a -5μm interference fit and the bearing internal clearance is varied to show the effect on the housing deformation. In this study, 0μm, -5μm, -10μm and -15μm bearing clearances are used, and a negative value indicates an interference fit. The rotor is still rotated at 1000rpm and a 3000N load is applied to rotor center.

Table 4.2 lists the calculated reaction force and moment of the Bearing 1 in Figure 4.5. Figure 4.16 demonstrates the deformed configurations of rotor and housings under radial load. As the bearing internal interference increases, the contact stiffness between balls and races increases. So when the rotor tilts, a large reaction moment is generated to tilt the bearing as a rigid disk in the same direction. As a result, the increased the moment bends the housing in the same direction as well. It is shown that the bearing internal clearance can affect the deformation of the

housing, since the behavior of each part within the rotor-bearing system interrelates with all others.

Table 4.2. Reaction forces and moment of bearing.

Bearing Internal Clearances	Fz (N)	Fx (N)	My0 (Nm)
0μm	-1500	-292.2	6.77
-5 μm	-1500	-277.8	10.90
-10 μm	-1500	-266.1	16.77
-15 μm	-1500	-265.7	23.16

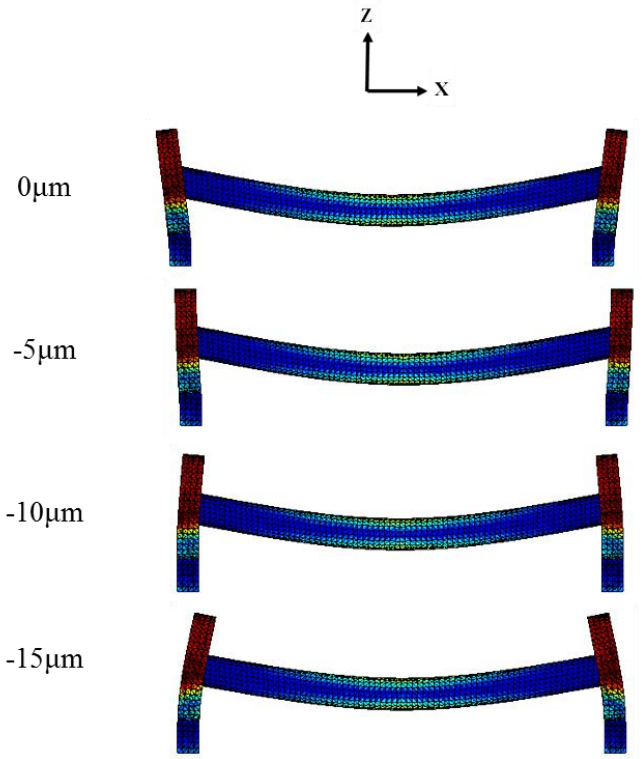

Figure 4.16. Deformed configuration of EFEM rotor and housings (housing deformation*2000).

Besides the bearing internal clearance, the configuration of the rotor-bearing system can also change the resulting deformation of bearing housings. A rotor-bearing configuration under overhung load was created by relocating Bearing 2 100mm towards rotor center, and a 3000N radial load was applied at the end of the overhung portion. The bearing internal clearance and housing clearance are first chosen to be 0μm (transition fit).

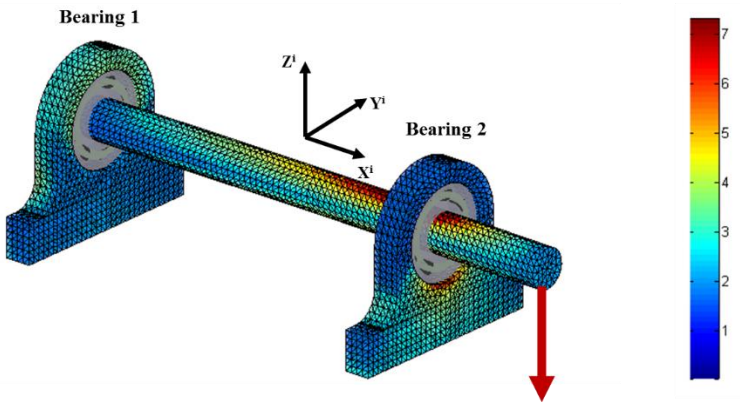

Figure 4.17. The combined rotor-bearing model with overhung load applied at end of the rotor (von Mises stress in MPa shown in the figure).

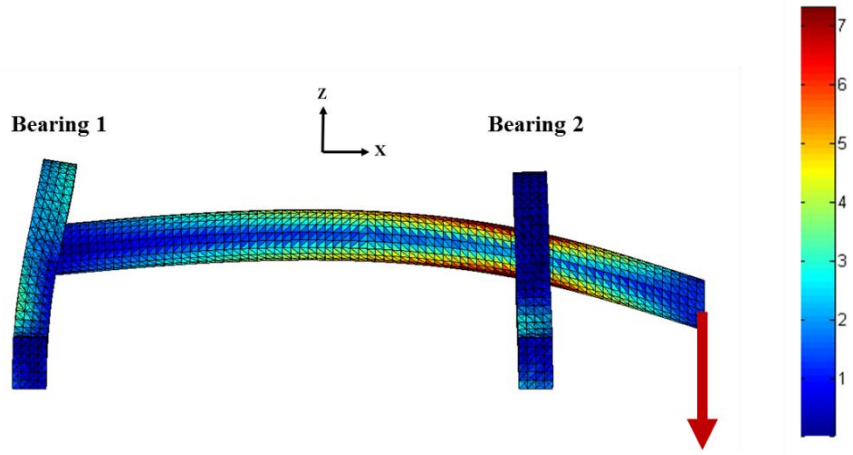

Figure 4.18. Deformed configuration of EFEM rotor and housings under overhung load (housing deformation*2000, von Mises stress in MPa shown in the figure).

Figure 4.17 illustrates the von Mises stress contours generated within the rotor and bearing housings as a result of the overhung load. It can be seen that the rotor is supported at the bottom of housing for Bearing 2 and at the top of the housing for Bearing 1 so that the reaction forces and applied force are balanced. Since the top of the pillow block housing is significantly more flexible than the bottom which is fixed to ground, much larger deformation is observed in Bearing 1 as well, as shown in Figure 4.18. Similar simulations were then repeated for various housing clearance conditions and a fixed OR condition for comparison. Table 4.3 lists the resulting IR displacements/angles and reaction forces/moments. As the housing support changes

from a fixed OR condition to a positive clearance fit condition, the bearing support stiffness reduces. Therefore the displacement of IR increases. It is also observed that the magnitude of reaction force in X direction decreases, since the OR follows the motion of the IR better with a reduction of support stiffness. The reaction force in Z direction and tilt angle, however, do not change much with the housing conditions, since they are determined only by the distances between the bearings and the location where the external load is applied.

Table 4.3. Results of displacements/angles and reaction forces/moments of the rotor-bearing system under overhung load for various housing clearance cases and fixed OR case.

Bearing 1				
		Housing Clearance		
	Fixed OR	-5μm	0μm	+5μm
IR X (μm)	60.7	61.2	61.6	62.1
IR Z (μm)	10.8	11.0	12.0	15.2
Fx (N)	-141.4	-130.9	-124.4	-118.4
Fz (N)	-981.4	-982.6	-982.5	-976.5
IR Tilt Angle (deg)	-0.088	-0.088	-0.088	-0.087
IR Moment (Nm)	1.308	1.252	1.238	1.226
Bearing 2				
		Housing Clearance		
	Fixed OR	-5μm	0μm	+5μm
IR X (μm)	60.7	61.2	61.6	62.1
IR Z (μm)	-28.4	-29.2	-29.5	-32.25
Fx (N)	141.4	130.9	124.4	118.4
Fz (N)	3981.4	3982.6	3982.5	3976.5
IR Tilt Angle (deg)	0.203	0.203	0.203	0.204
IR Moment (Nm)	4.191	4.098	4.049	4.039

4.3.4 Rotor Critical Speed

Critical speed of a shaft rotor system is the theoretical angular velocity at which the deflection of the shaft reaches maximum. The critical speed can also be excited by an unbalance mass with respect to the axis of rotation. It is important to study the performance of the rotor-bearing system at critical speed, since in many applications the operating speed of the rotor has to go through the critical speed. The rotor first critical speed simulated by the EFEM rotor model was

validated by Brouwer and Sadeghi [39] and the results compared well with ABAQUS and analytical solutions. In this work, the effect of first critical speed is simulated using the combined rotor-bearing system model in Figure 4.9. A 20kg mass disk is added to the center of the rotor by distributing the mass evenly to all the nodes at the center cross-section. The rotor speed is increased from 0 to 10,000rpm, and an imbalance mass is added to the rotor center to excite the critical speed and no external load is applied to the system.

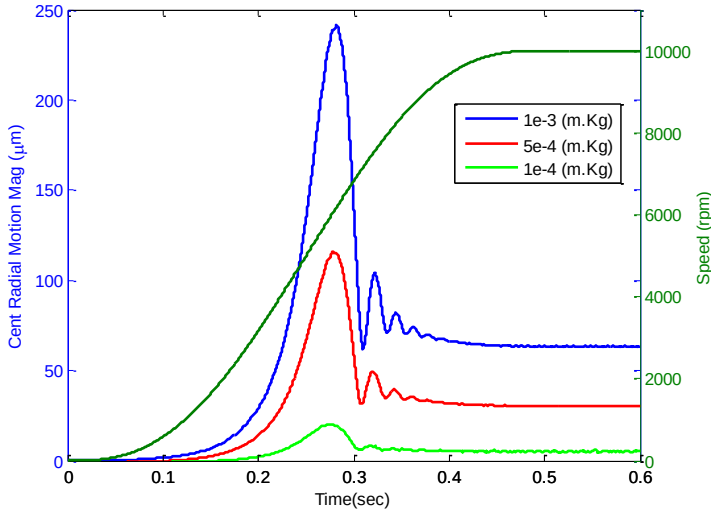

Figure 4.19. Magnitude of rotor deflection as rotor speed is increased from 0 to 10,000rpm.

First, transition fit (0μm) is specified for both bearing internal clearance and housing clearance and Figure 4.19 depicts the displacement of rotor center for three imbalance mass cases (1e-3 m*kg, 5e-4 m*kg, and 1e-4 m*kg). As it can be seen, the rotor deflection magnitude reduces linearly with the reduction of imbalance mass. It is found that the displacement reaches its peak magnitude at the first critical speed which is 6,457rpm. To show the effect of rotor critical speed under a severe loading condition, a large imbalance mass (1e-3 m*kg) was used in the following results. Figure 4.20 and Figure 4.21 show the comparison of bearing IR displacements between a rotor-bearing system with flexible housing support and one with fixed OR. It can be seen that as the rotor passes through the first critical speed, the bearing IR displacement is increased when housing flexibility is considered. Also note that compared to the case of fixed OR model, the IR displacement is significantly larger in +Z, +Y and –Y direction, but nearly the same in –Z direction. This is due to the fact that when the bottom of the housing is fixed to ground, the

support stiffness is large in the –Z direction, and in the other directions, the support stiffness is reduced as the result of variation in geometry and boundary conditions. The deformed configurations of the system at every 90 degrees of rotor rotation at critical speed can be seen in Figure 4.22. The rotor deflection at resonance also causes the reaction moment to increase, as can be seen in Figure 4.23. The results in Figure 4.23 also show that the moment is reduced with a positive bearing internal clearance.

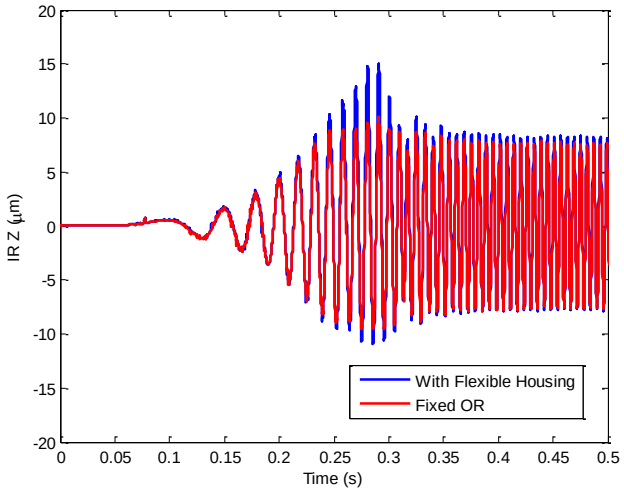

Figure 4.20. Bearing IR displacement in Z for a rotor-bearing model with fixed OR and one with flexible housing support.

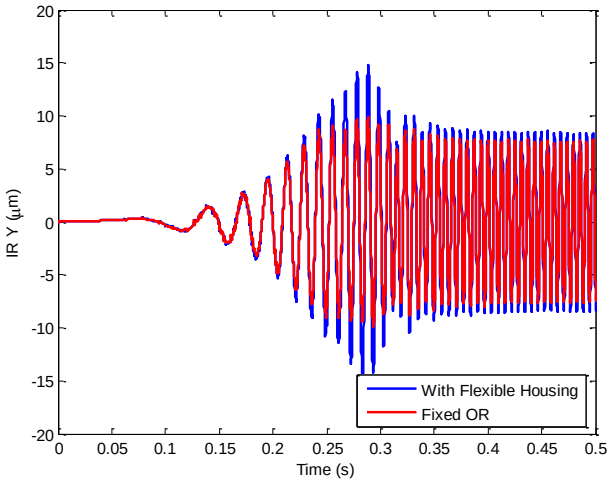

Figure 4.21. Bearing IR displacement in Y for a rotor-bearing model with fixed OR and one with flexible housing support.

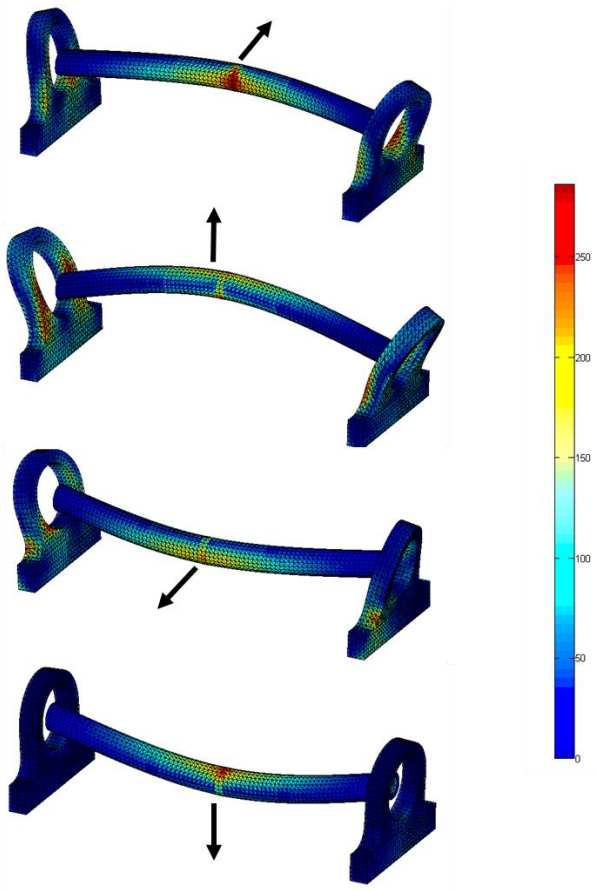

Figure 4.22. Deformed configurations of EFEM rotor and housings at first critical speed (Motions captured at every 90 degrees of rotor rotation, and the arrows indicate the directions of rotor deformation, von Mises stress in MPa shown in the figure).

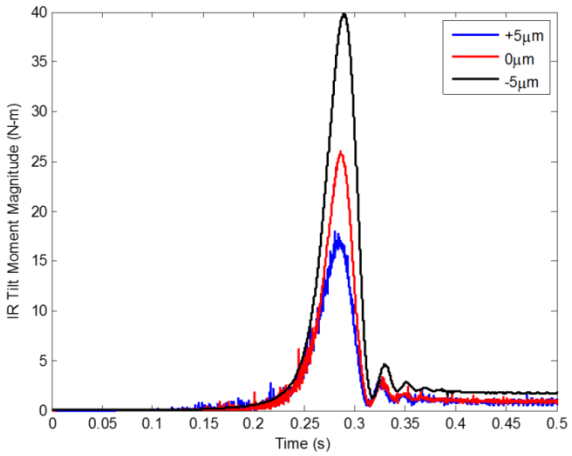

Figure 4.23. Reaction moment of bearing as the rotor goes through first critical speed.

4.4 Conclusions

In this investigation a combined EFEM-DEM dynamic rotor-bearing model has been developed to study the behaviors of rotor, bearing and bearing housing under various conditions. The dynamic bearing model is based on the discrete element method and the flexible rotor and housing models are developed using the explicit finite element method. The results show that both the bearing internal clearance and housing bore clearance have a significant impact on the VC vibration. The magnitude of VC vibration decreases as the bearing internal clearance becomes smaller. A large housing clearance, on the other hand, will lead to insufficient support stiffness and bearing unstable motion as the contact area between bearing OR and housing reduces significantly. It was also demonstrated that deflection of the rotor causes the generation of bearing reaction force and moment, which can also be affected by bearing clearance. Housing deformation was shown to vary with the reactions generated within the bearing. Therefore it is important to properly choose the clearances as well as the location of external load, since the behavior of each component (bearing, rotor, housing, etc.) are interrelated with each other. Rotor first critical speed was also studied, and housing flexibility was shown to increase the IR displacement at resonance. When the rotor reaches large deflection at critical speed, reaction moment increases in the bearing accordingly. And typically a large reaction moment is related to an increase in contact force and friction which may reduce bearing life.

CHAPTER 5. A WIRELESS SENSOR TELEMETER FOR IN-SITU CAGE VIBRATION MEASUREMENT AND CORROBORATION WITH ANALYTICAL RESULTS

5.1 Introduction

This chapter discusses the development of a cage telemeter and a dynamic bearing model for the investigation of bearing cage dynamics. The cage in the dynamic bearing model is developed using the explicit finite element method (EFEM) described by Cao et al. [43, 44, and 62]. And the cage sensor telemeter is based on the LC circuit previously used by Ashtekar et al. [53] for bearing cage temperature measurements. Modification to the signal acquisition and data processing demonstrated that the same LC circuit can be used to detect and collect cage vibrational motion. The telemeter was tested in a pristine and defective (spalled) bearing to collect cage dynamic vibration under various conditions. The performance of the cage telemeter is compared with accelerometer measurements under the same conditions. The chapter also discusses the correlation between the analytical simulation and experimental measurements.

5.2 Cage Telemeter and Experimental Equipment

The vibration telemeter developed for this study is similar in principle to the bearing cage telemeters developed by Ashtekar et al. [53] and Brouwer et al. [59]. However, instead of measuring the cage temperature, which was done by tracking the resonant frequency of the sensor on the cage, the LC circuit is used to detect the high frequency vibrational signals associated with the cage motion. The data acquisition and signal processing procedures were revised to achieve the sensing of cage motion. Details of the telemeter design and experimental setup are given in the following sections.

5.2.1 Design and Instrumentation

The telemeter design has two major components: a passive LC circuit instrumented on the bearing cage and an active transceiver for receiving the signals. Figure 5.1 depicts the telemeter installed on the cage of a ball bearing. The passive sensor on the bearing cage is an inductor-capacitor resonator. A U2J type ceramic capacitor (C) is attached to the side of the cage using electrically-insulating epoxy and the inductor placed along the cage circumference is a single

loop of coil (L1). The transceiver is also represented by a single loop of coil (L2) which is then linked to a signal analyzer. Both coils are pressed into the groove milled out of a PEEK insert ring for electrical insulation. As seen in the figure, the transceiver was located in proximity (3mm) to the sensor on the cage, since the telemeter uses magnetic field for coupling between the two inductors, a close distance ensures a strong coupling while also minimizes the effect of metallic surrounding on the signal.

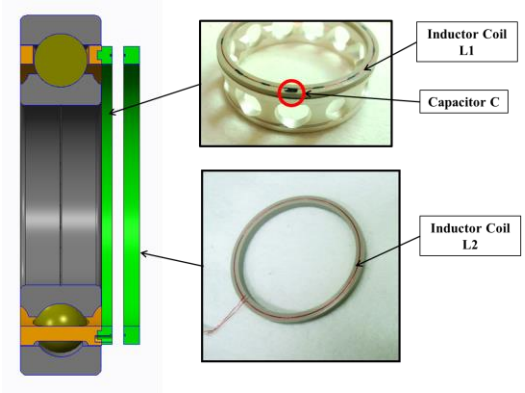

Figure 5.1. Cage telemeter instrumentation on a ball bearing.

When the LC resonator and transceiver are coupled, an energy loss is detected by a vector network analyzer used in the experiment. Figure 5.2 illustrates the S_{11} measured by the network analyzer. S_{11} is the reflection coefficient between the input power from the analyzer and the reflected power from the sensor. The signal spectrum indicates that the maximum power consumption occurs near the natural frequency of the LC resonator.

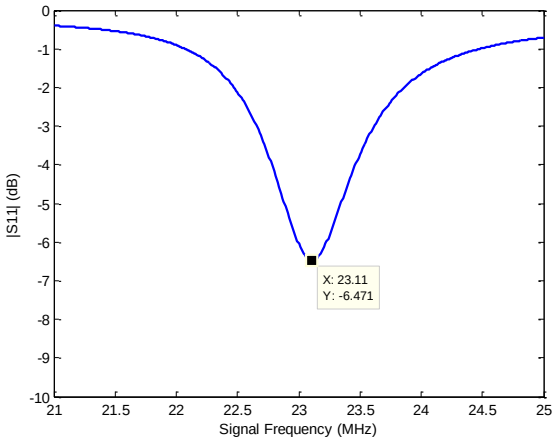

Figure 5.2. Telemeter signal spectrum detected at 5mm axial distance between the transceiver and stationary cage.

Previous investigators [53, 59] using the same circuitry searched this spectrum for the natural frequency which was then converted to temperature. In this work, however, it is assumed that the temperature has negligible influence on the vibration measurement since temperature varies at a much lower frequency. Therefore, in the vibration measurement, searching for the resonant frequency over a frequency span is no longer necessary. Instead, the cage vibration is measured by monitoring the signal amplitude at a single frequency. Since the cage motion affects the coupling between the resonator and transceiver, it causes a change in the signal amplitude. Thus, by performing a FFT transformation on the signal amplitude the cage vibration can be obtained. Please note that the current telemeter design is able to detect the cage vibration frequency, but it cannot discern the direction and exact position of the cage center of mass.

5.2.1.1 Validation of Cage Translational Motion Detection

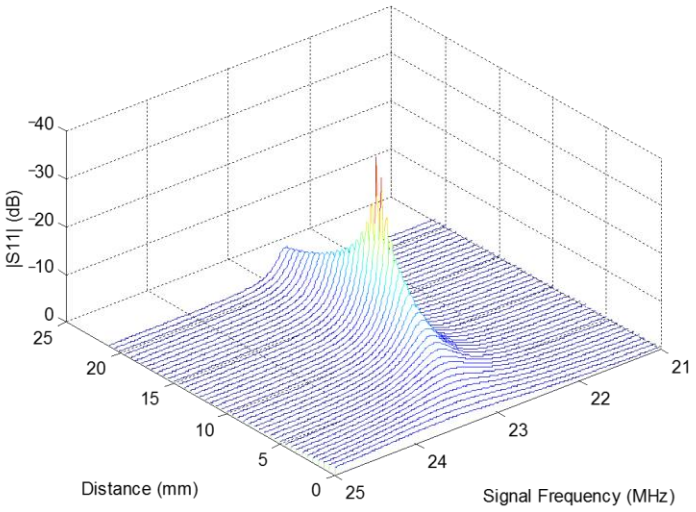

Figure 5.3. Waterfall plot of the cage telemeter signal spectrum at various distances.

Figure 5.3 illustrates the shift in the signal spectrum when the radial distance between the inductors was increased from 0 mm to 20 mm while the axial distance was fixed at 3 mm. The results demonstrate the signal sensitivity to cage displacement. A shaker was then used to create vibration on the sensor under controlled conditions. Figure 5.4 illustrates the setup on the shaker for vibration measurements. The cage instrumented with the sensor was placed on top of the

shaker and the transceiver was fixed to a stationary stand. The shaker was used to vibrate the cage at a constant frequency. Figure 5.5 depicts the oscillation of the signal amplitude in both time and frequency domains. The frequency domain result (Figure 5.5 (b)) depicts a peak at 120 Hz which is the same as the shaker output frequency. This demonstrated that the cage telemeter is capable of detecting cage translational motion and thus vibration.

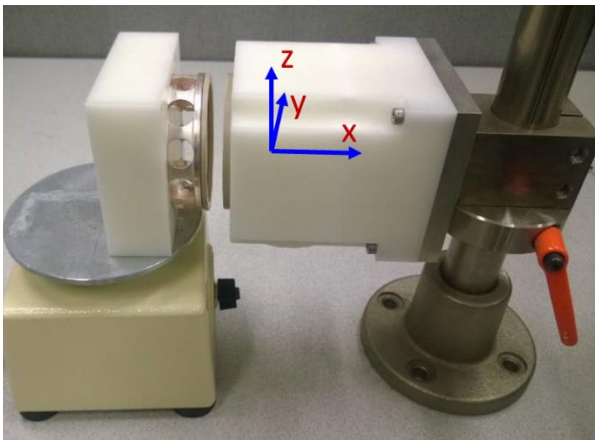

Figure 5.4. Vibration measurement validation using a shaker.

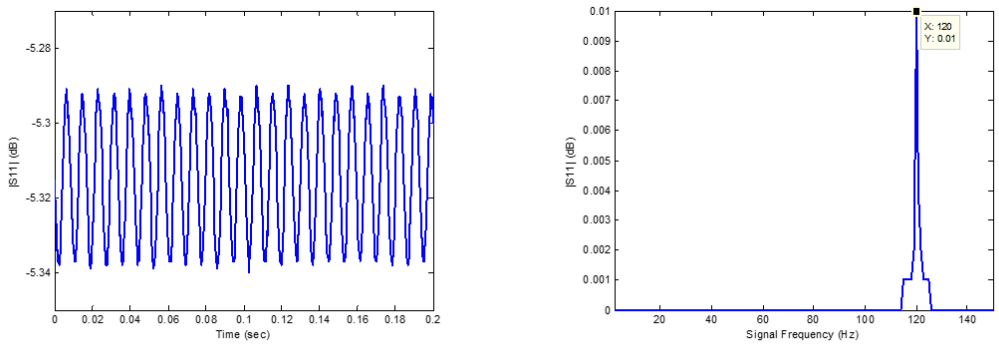

(a) (b)

Figure 5.5. (a) Detected signal of shaker vibration (in Z direction at 120Hz) in time domain, (b) same signal shown in frequency domain.

5.2.1.2 Validation of Cage Rotational Motion Detection

The previous tests successfully demonstrated that the sensor can measure frequency of vibration when the cage was not rotated and simply translated at a particular frequency relative to the transceiver. To demonstrate the capability of the sensor during operation (rotating), the sensor was installed on the spindle of the lathe using the available chuck, while the transceiver was

attached to the mill of the CNC machine. In this configuration, the sensor and receiver could be moved and precisely controlled to be positioned relative to one another in space. In the CNC machine, the lathe (rotating spindle) is attached to a programmable XY table, which allows the sensor and receiver to be axially (X-direction) or radially (Y-direction) positioned relative to each other. The receiver attached to the mill of the CNC could also be programmed to be positioned relative to the sensor in the Z-direction (perpendicular to the lathe spindle axis). Figure 5.6 and Figure 5.7 illustrate the setup for the test. The CNC machine was programmed to accurately control the rotational speed of the cage and relative position between the cage and transceiver.

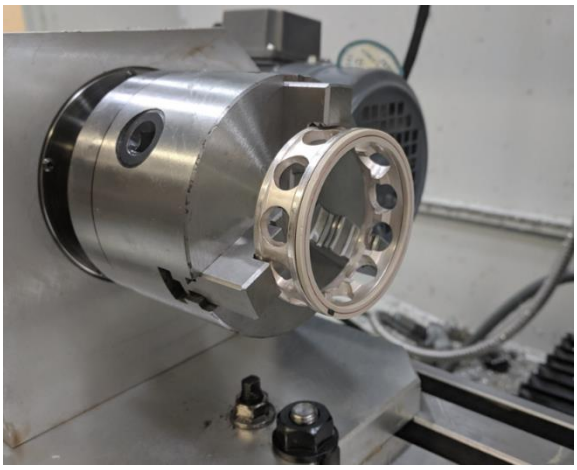

Figure 5.6. Instrumented cage on the spindle of a lathe.

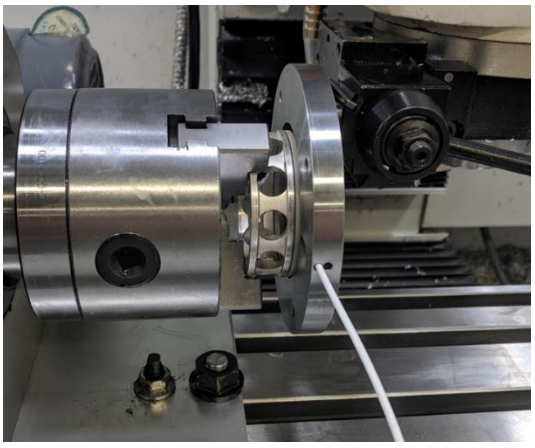

Figure 5.7. Cage rotation measurement setup on a CNC machine.

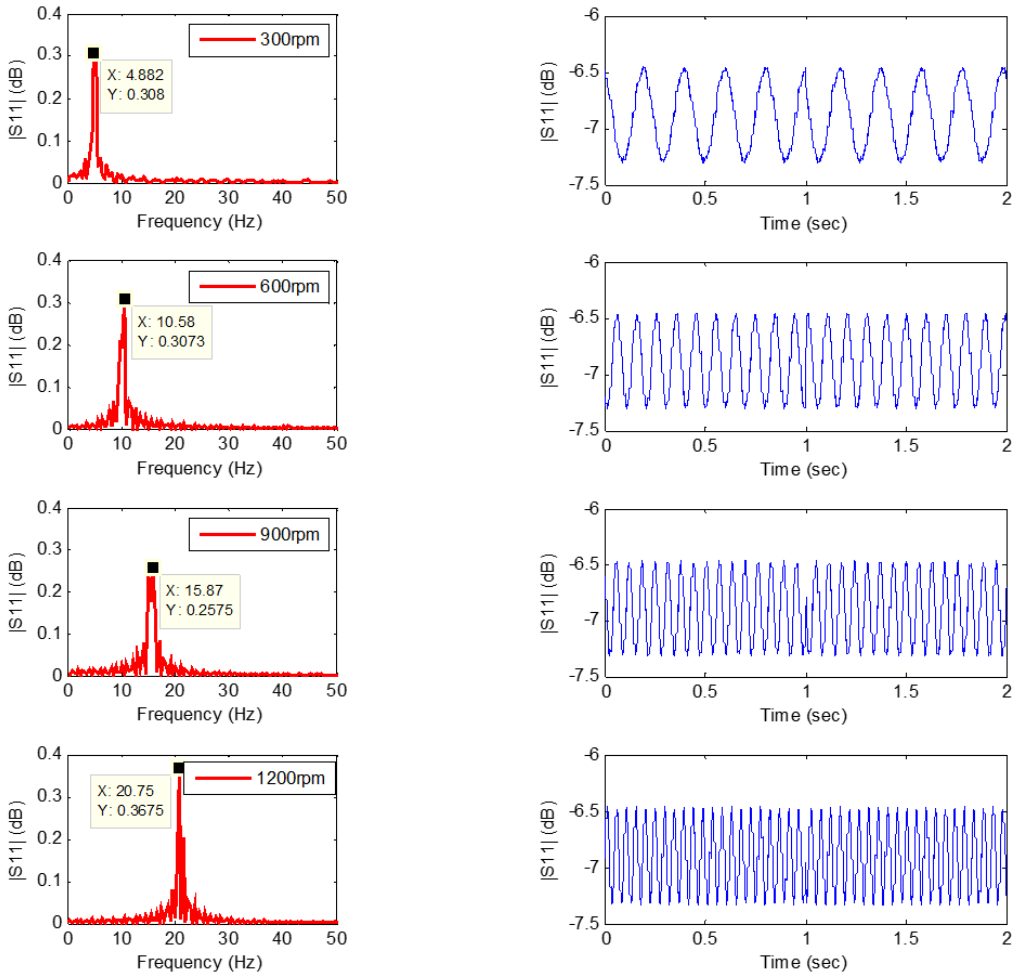

(a) (b)

Figure 5.8. a) Detected cage rotation signal in frequency domain, (b) same result in time domain.

Figure 5.8 depicts the signal oscillation due to the cage rotation, while the two inductors were kept at a 1.78 mm axial distance and 1.27 mm radial offset. The cage rotational speed was varied between 300 rpm (5 Hz) and 1200 rpm (20 Hz). The frequency domain results shown in Figure 5.8 depict the dominant peak at cage speed frequency. Table 5.1 provides a comparison between the actual spindle output speed, which was recorded by a built-in speed sensor and the speed detected by the telemeter. As shown, the results are in good agreement.

Table 5.1: Cage speed measurement results from spindle sensor and cage telemeter.

Input Speed (RPM)	Spindle Speed (RPM)	Telemeter Measured Speed (RPM)	Difference (%)
300	295	292.9	0.7
600	613	634.8	3.4
900	940	952.2	1.3
1200	1260	1245	1.2

The correlation between the signal amplitude and offset distance was also investigated. The radial offset was increased, while the cage rotation speed (300 rpm) and axial displacement (1.78 mm) were kept constant. To check if the signal is sensitive to radial direction, the radial offset was increased along various directions. Figure 5.9 illustrates the signal amplitude versus the offset distance in each angular direction. The results demonstrate that the signal strength did not depend on the angular direction, but it increased with offset distance.

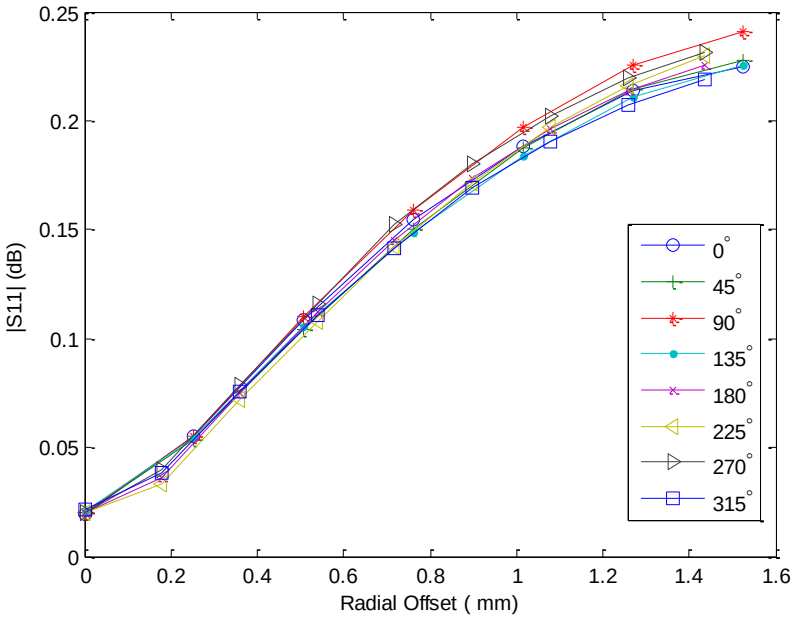

Figure 5.9. Cage telemeter signal sensitivity with radial offset distance along various directions.

5.2.1.3 Combined Translational and Rotational Motions Detection

In this test, both rotational and translational motions were applied to the telemeter. The spindle and thus the cage rotational speed was set to 1200 rpm (20 Hz), and the XY table was

programmed to oscillate radially at a specified feed rate for 10 cycles. Three feed rates were used: 0.85 mm/s, 1.69 mm/s, and 3.84 mm/s. Figure 5.10 depicts the FFT results of the 3 different feed rate cases and all three signal spectrums have a peak near spindle frequency due to cage rotation. In the lower frequency range, there is a secondary peak indicating the translational oscillation of the lathe and the frequency of this peak increases with the feed rate.

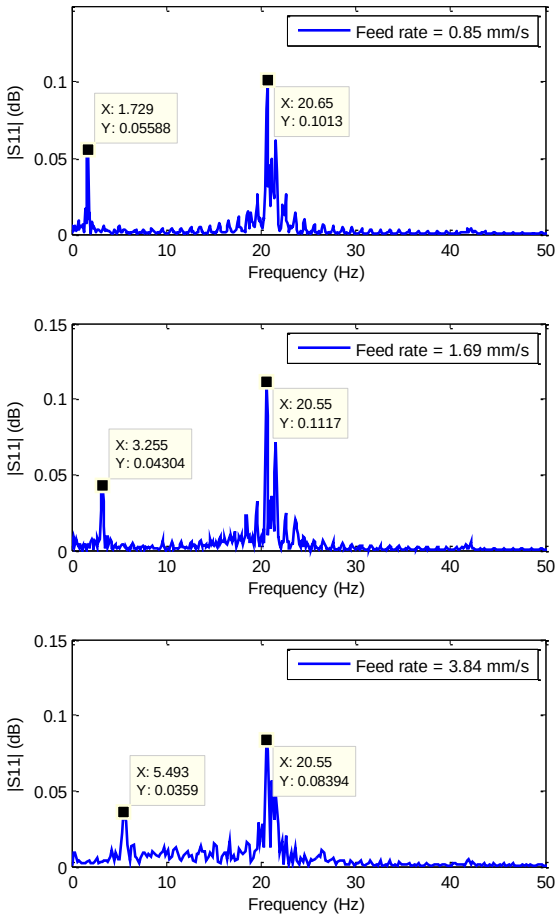

Figure 5.10. Detected signals of the combined translational and rotational cage motions (translational motion is specified by the spindle feed rate, and rotational motion is at 1200rpm).

5.2.2 Experimental Equipment

Figure 5.11 depicts the test rig developed for this investigation. The rig was designed to test a ball bearing instrumented with the cage telemeter. The test rig consists of a main shaft driven by an electric variable speed motor, a ball bearing supporting radial load, a double-row spherical

roller bearing supporting both axial and radial loads and a test bearing assembly within which the instrumented ball bearing was mounted. A displacement-controlled axial loading mechanism was used to apply axial load to the test bearing by rotating the large screw as seen in the cross-section CAD drawing in Figure 5.12. The magnitude of the axial load was measured by the inline donut-shaped load cell. Radial load was applied by hanging dead weight on the test bearing housing.

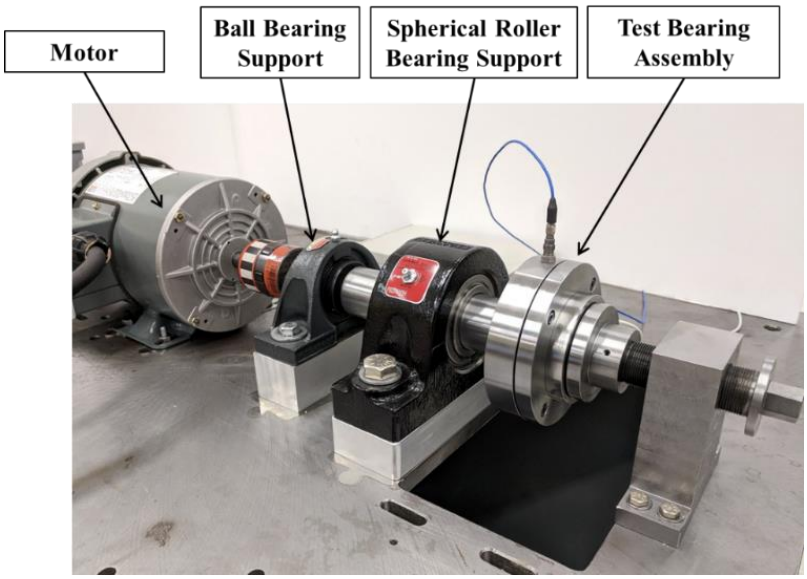

Figure 5.11. Test rig for instrumented bearing tests.

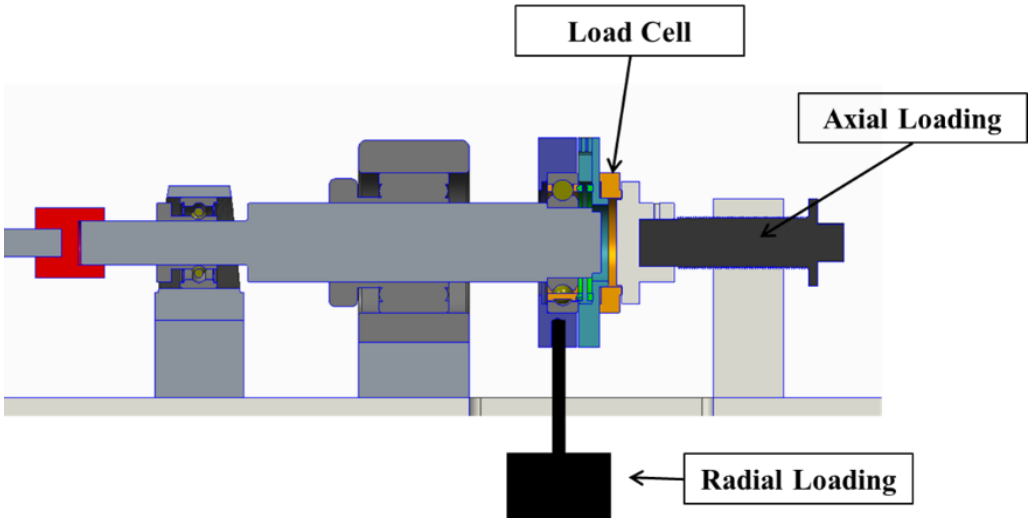

Figure 5.12. CAD drawing of the test rig.

Figure 5.13 shows a cross-sectional view of the test bearing assembly. The test bearing with instrumented cage was pressed into the housing and the transceiver was attached to the opposing inner surface of the housing at a distance of 3 mm next to the sensor. Holes were drilled through the housing for the cable to connect the transceiver with a vector network analyzer. The vector network analyzer used in the test has a maximum sampling rate of 6,666 Hz. Two piezo-electric accelerometers were used to measure bearing housing vibrations, and the results from the accelerometers were compared with the cage telemeter measurements. A user-interface program was designed to read and record the experimental data.

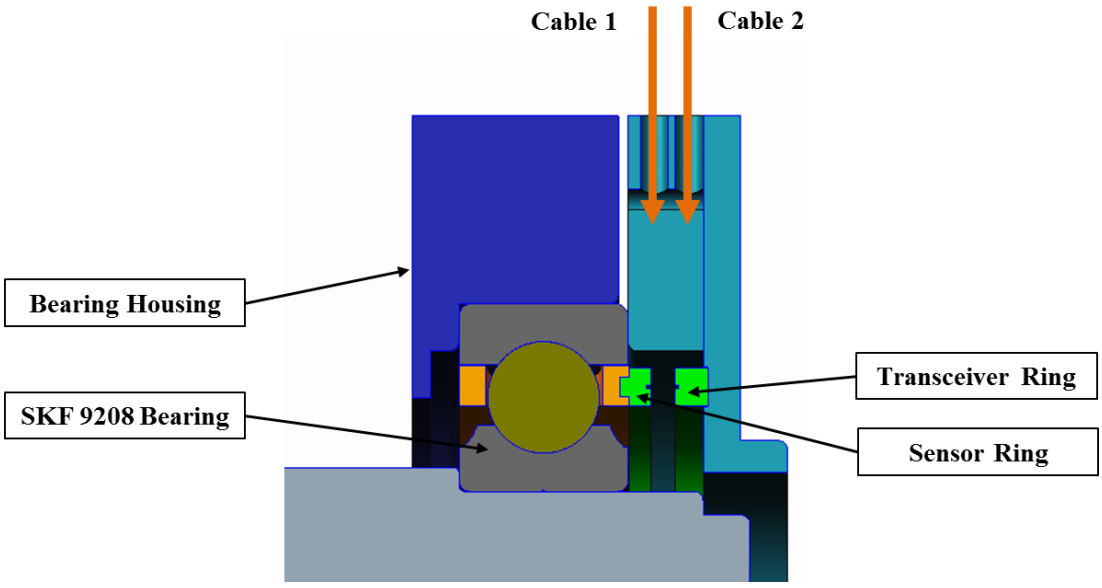

Figure 5.13. CAD drawing of the test bearing assembly.

5.3 Dynamic Bearing Model with EFEM Cage

For the analytical part of this investigation, a combined EFEM-DEM dynamic bearing model was developed to simulate the test bearing and corroborate experimental results. Details of both the model are described in the following sections.

5.3.1 DEM Dynamic Bearing Model

In the DEM dynamic bearing model [4], it is assumed that each bearing element is a rigid body with 6 degrees of freedom in a three dimensional space. Contact forces and moments are calculated for each bearing element to obtain the equations of motion. The normal contact force

is determined by the geometric interaction between the two rigid bodies in contact and the magnitude of the force is based on the Hertzian force-deflection relationship:

$$F_n = k\delta^{3/2} \tag{5.1}$$

where k is the Hertzian contact stiffness and δ is the geometric overlap. The traction force is calculated using the normal force and a friction coefficient which is a function of the relative slip velocity at contact location. Weinzapfel and Sadeghi [10] provided a full description of this approach. The reaction moment due to the contact force and the contact spin torque due to the variation of slip velocity within the contact region are also calculated in the bearing model. The net force and moment acting on each element are summed and used to determine the translational and rotation equations of motion. These equations are then integrated in time using the 4th order Runge-Kutta method to obtain the dynamic solution.

5.3.2 EFEM Cage Model Description

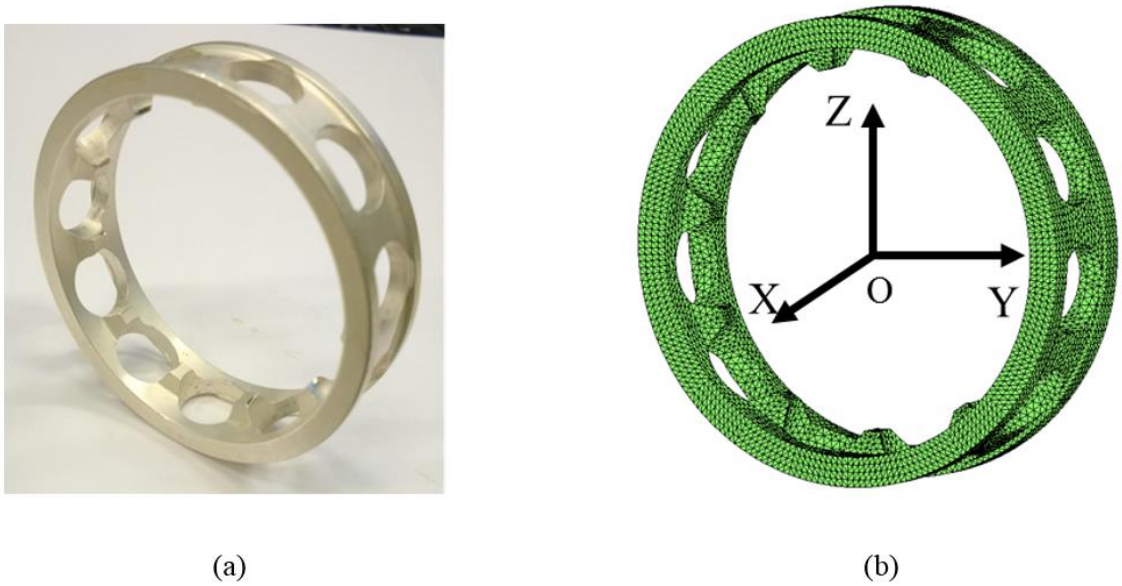

Figure 5.14. (a) outer race guided bearing cage, (b) mesh of EFEM cage model.

Figure 5.14 depicts the machined cage of the ball bearing and a mesh based on the same cage geometry. The mesh is created using the tetrahedral element and the cage material is steel. The EFEM formulation starts with the calculation of the deformation gradient of each tetrahedral element,

$$\boldsymbol{F}_{ij} = \boldsymbol{\delta}_{ij} + \sum_{n=1}^{4} \frac{\partial N^n}{\partial X^j} u_i^n \tag{5.2}$$

where u is the displacement of the node, X is the coordinates of the node in the initial configuration, N stands for the shape function of tetrahedral element and $\boldsymbol{\delta}$ is the Kronecker delta. The deformation gradient is then used to calculate the Right Cauchy-Green deformation tensor;

$$\boldsymbol{C}_{ij} = \boldsymbol{F}^T \boldsymbol{F} \tag{5.3}$$

Using the deformation tensor $\boldsymbol{C}_{ij}$, the Lagrangian strain tensor can be evaluated

$$\boldsymbol{E}_{ij}^L = \frac{1}{2}(\boldsymbol{C}_{ij} - \boldsymbol{\delta}_{ij}) \tag{5.4}$$

Then the second Piola-Kirchhoff stress is determined using

$$\boldsymbol{S}_{ij} = \frac{E}{1+v}(\boldsymbol{E}_{ij}^L + \frac{v}{1-2v} tr(\boldsymbol{E}_{ij}^L)\boldsymbol{\delta}_{ij}) \tag{5.5}$$

where v is Poisson ratio and E is Young's modulus. The second Piola-Kirchhoff stress $\boldsymbol{S}_{ij}$ is used to calculate the nodal force in the undeformed configuration

$$\boldsymbol{f_0} = (\boldsymbol{S}_{ij} \cdot \boldsymbol{n_0}) \cdot A \tag{5.6}$$

with A being the face surface area and $\boldsymbol{n_0}$ being the face outward normal. $\boldsymbol{f_0}$ is converted to the traction force $\boldsymbol{f}$ in the deformed configuration following a push-forward operation using the deformation gradient tensor

$$\boldsymbol{f} = \boldsymbol{F} \cdot \boldsymbol{f_0} \tag{5.7}$$

The traction force is equally distributed over all the nodes on each face to calculate the total nodal force. The equation of motion for each node is integrated in time to solve for the nodal displacement. This process is repeated for each element within the mesh so that a dynamic solution of the entire cage is obtained.

Contact algorithms are developed to combine the EFEM cage with the rest of the bearing elements. Since the cage modeled in this study is guided by outer race, contact may occur

between the balls and cage pockets, as well as between cage and outer race. Figure 5.15 shows the contact regions on the cage.

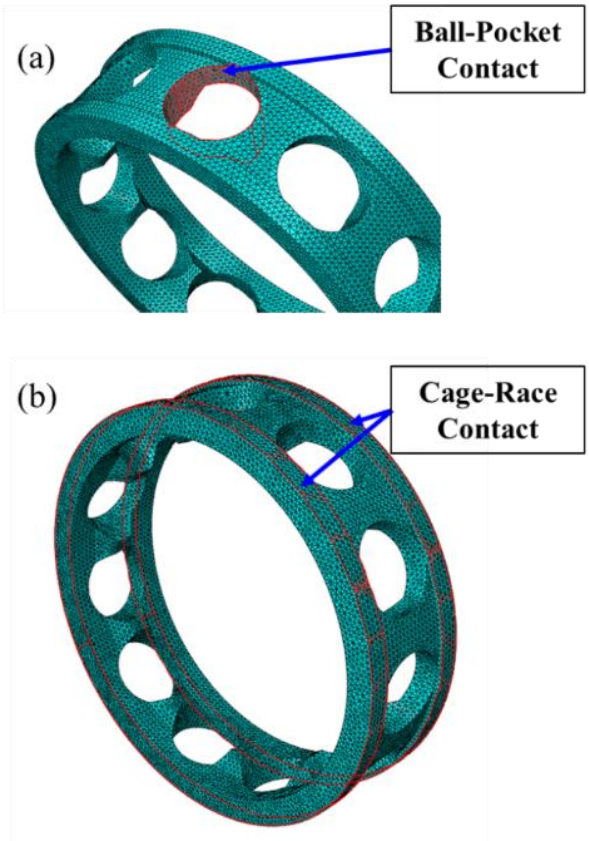

Figure 5.15. (a) ball-pocket contact region, (b) cage-race contact region.

In the previous bearing model developed by Saheta [4], normal contact force on the rigid cage was based on the Hertzian formula, which causes difficulty in the convergence of the solution for the EFEM cage due to the high contact stiffness. Therefore, a more efficient penalty method was applied to solve for contact forces. The normal force is calculated based on the interpenetration between the nodes on the EFEM cage and the rigid bearing elements (balls or outer race)

$$\boldsymbol{F_n} = \Delta d * K * \boldsymbol{n} \tag{5.8}$$

where Δd is the penetrated distance of node into the rigid element, K is the contact stiffness, and $\boldsymbol{n}$ is the unit normal at contact. $K = 2e8\ N/m$ is used in the model so that nodal penetration is minimized and the solution can be robust. Friction force is also evaluated at contact on the cage using a traction coefficient of 0.1.

5.3.3 EFEM Cage Validation – Modal Analysis

The dynamic behavior of the EFEM cage under external excitation has been studied and validated using modal analysis. The first two natural frequencies in the lower frequency range (0 - 5,000 Hz) were obtained, since low frequency modes are commonly the most prominent modes at which the structure vibrates. The first two natural frequencies were determined through three different approaches: experimental impact modal analysis, EFEM cage simulation and ABAQUS Eigen solver.

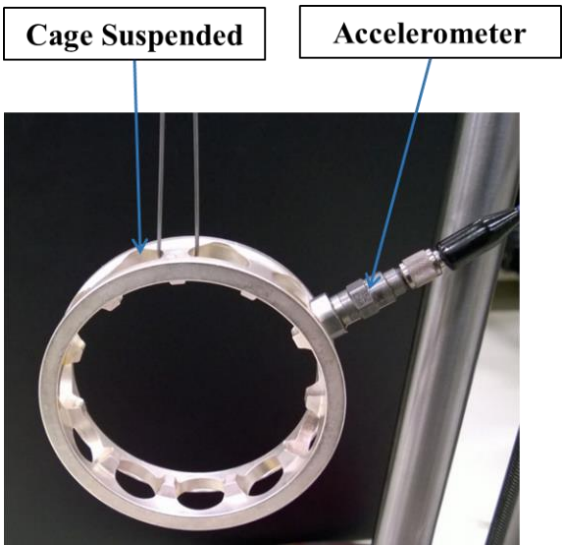

Figure 5.16. Experimental setup of the impact modal analysis.

Figure 5.16 illustrates the experimental impact modal analysis testing setup. In order to minimize the effects of the foundation (i.e. a foam pad), the cage was suspended using an elastic wire. The cage was excited by a quick impact from a hammer and the cage free vibration response was captured using the accelerometer attached to the cage circumference. The cage vibration response in the frequency domain, as seen in Figure 5.17, shows the dominant peaks of the first two natural frequencies. The case was impacted at different location while the accelerometer was also moved around the circumference of the cage. Invariably the first and second modes occurred at around 2006 Hz and 4392 Hz respectively.

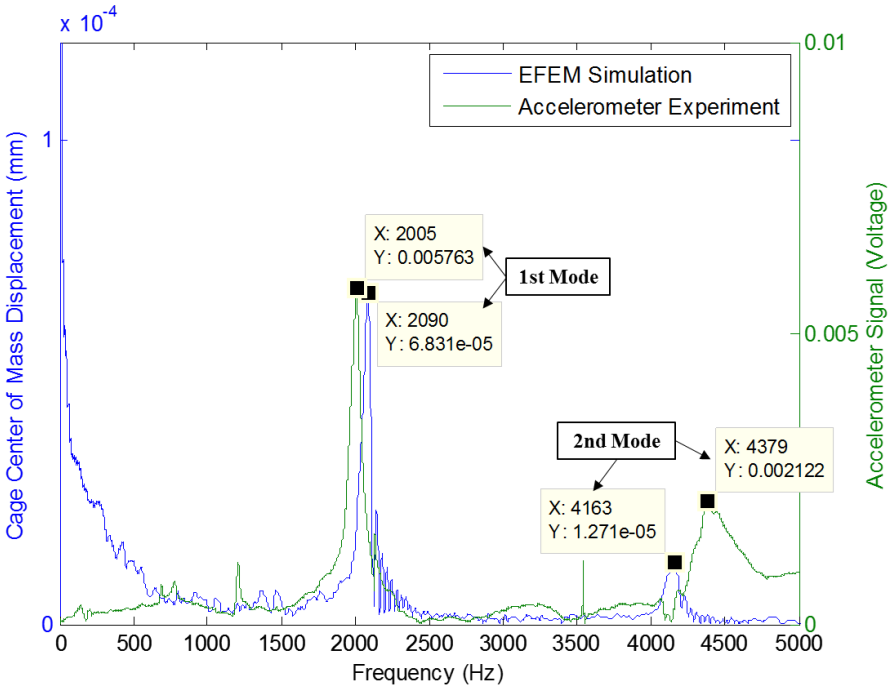

Figure 5.17. Modal analysis results from EFEM simulation and accelerometer signal of impact experiment.

A similar modal analysis with impact on the cage was simulated using the EFEM cage model. The EFEM cage was suspended by fixing the nodes on top of the cage, and gravity was applied to the cage model. An impact force was applied to the cage outer boundary for a short time duration of 0.0001 second. Figure 5.17 also depicts the response of the cage center of mass displacement in frequency domain, which also shows natural frequencies at 2084 Hz and 4163 Hz.

The cage modes and frequencies were then calculated in ABAQUS using the Lanczos eigensolver. A linear perturbation analysis was applied to the cage and the eigensolver identified the cage modes. The first two bending modes as seen in Figure 5.18 were determined to be at 1989 Hz and 4105 Hz, respectively. The natural frequencies of the cage obtained using the three methods (experimental impact, ABAQUS and current EFEM) are listed in Table 5.2 for comparison. It can be seen that results from all three methods are in good agreement, especially for the estimation of the first modal frequency.

Table 5.2: Results from the three modal analysis methods.

Bending Mode	ABAQUS (Hz)	EFEM Cage Model (Hz)	Impact Modal Analysis (Hz)
1st	1989	2084	2006
2nd	4105	4163	4392

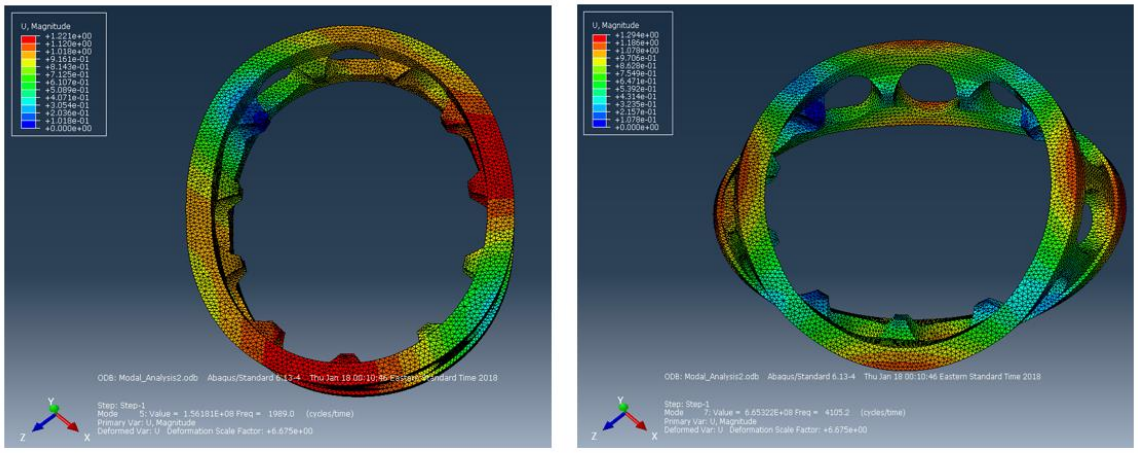

(a) (b)

Figure 5.18. ABAQUS modal analysis solution: (a) first bending mode 1989 Hz, (b) second bending mode 4105 Hz.

5.4 Results and Discussion

In this section, experimental results are presented to demonstrate the cage telemeter in monitoring in-situ cage motions and bearing defect. The EFEM cage model was used to study the cage motion under the same conditions as those in the experiments. Specifications of the ball bearing under test are listed in Table 5.3.

Table 5.3: Ball bearing specifications.

Ball Bearing	
Number of Balls	11
Pitch Radius (mm)	30.000
IR Groove Radius (mm)	6.600
OR Groove Radius (mm)	6.600
Ball Radius (mm)	5.953
Cage Pocket Radius (mm)	6.500
Cage Inner Radius (mm)	29.125
Cage Outer Radius (mm)	33.375
Cage Race Radial Clearance (mm)	0.200
Cage Mass (kg)	0.069
Cage Type	OR guide
Contact Angle (deg)	35
Lubricant	Mobile Jet Oil II

5.4.1 Cage Dynamics in a Pristine Bearing – Effect of Speed

The cage behavior was first studied in a pristine bearing to obtain a basic understanding of the effect of various operating conditions, such as speed. An axial load of 445 N was applied to the test bearing shown in Figure 5.11, and the shaft speed was increased with 600 rpm (10 Hz) increment to 1800 rpm (30 Hz). Figure 5.19 depicts the oscillation of signal amplitude received by the cage telemeter in the time domain. Figure 5.20 depicts the results for these conditions in the frequency domain. It can be seen that two dominant frequencies were generated on the cage, with one at the cage frequency (F_C), and the other one at shaft frequency (F_S).

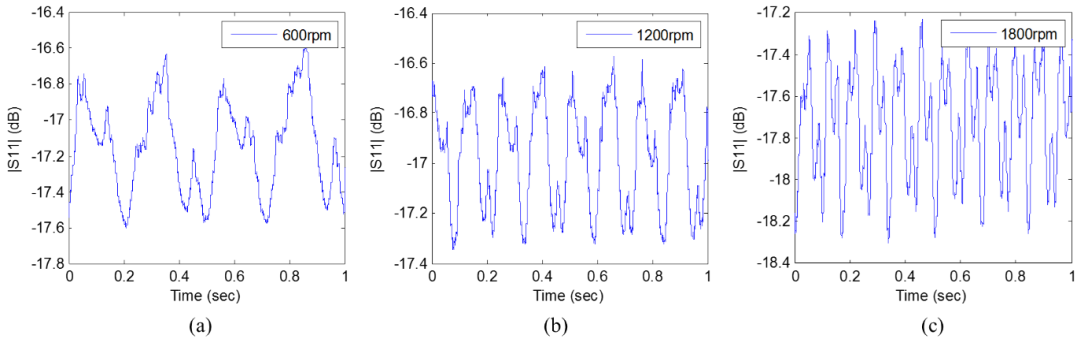

Figure 5.19. Detected cage speed signals in time domain: (a) 600rpm shaft speed, (b) 1200rpm shaft speed, (c) 1800rpm shaft speed.

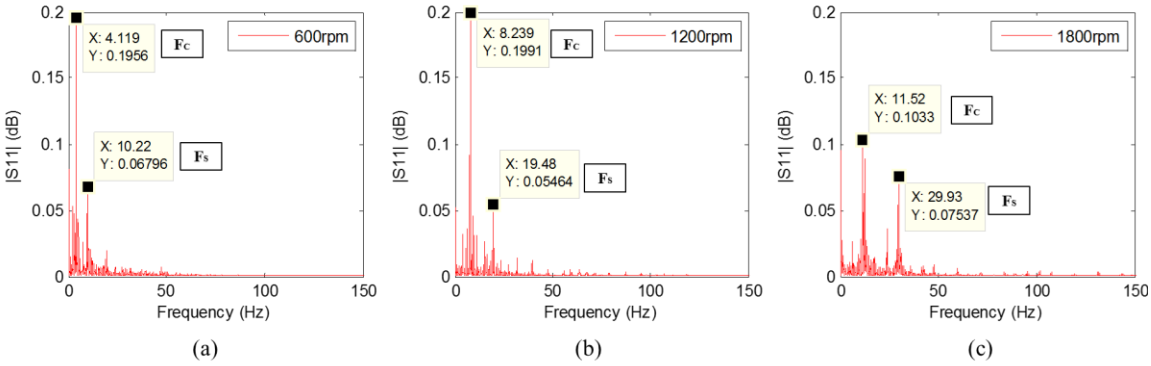

Figure 5.20. Detected cage speed signals in frequency domain: (a) 600rpm shaft speed, (b) 1200rpm shaft speed, (c) 1800rpm shaft speed.

To obtain further insight into the cage motion, the same speed and axial load conditions were simulated using the dynamic bearing model with EFEM cage. In the model, the inner race speed was increased from 0 to the steady-state speeds at 600 rpm, 1200 rpm, and 1800 rpm respectively, and an axial load (445 N) was applied to the outer race similar to the experimental setup. The outer race was supported by an elastic foundation which was represented by a spring and dashpot model. Gravity was applied. Figure 5.21 depicts the motion of the cage center of mass for the three speed cases. Note that in all three cases the cage center was moved downwards due to gravity, and towards one side due to the direction of bearing rotation. At 600 rpm, the speed was not large enough to generate a centrifugal force and cause the cage to whirl, therefore the cage moved towards the bottom of the bearing (outer race) at a radial displacement of 0.2 mm, which was the clearance between the cage and outer race. As the speed increased to 1800 rpm, the centrifugal force become more significant and caused a whirling motion. This may explain the reduction of the signal amplitude at cage frequency for the 1800 rpm case, since the signal is less sensitive to cage rotation when the cage center is closer to the center of the transceiver. Figure 5.22 illustrates the simulation results for the dominant peak at cage frequency. Table 5.4 provides a comparison between the cage frequencies obtained from measurement and simulation. The results indicate a close correlation.

Table 5.4: Experimental and analytical results of cage frequency in test bearing.

Motor Input Shaft Frequency (Hz)	Detected Shaft Frequency (Hz)	Detected Cage Frequency (Hz)	Simulated Cage Frequency (Hz)
10	10.22	4.119	3.815
20	19.48	8.239	8.392
30	29.90	11.52	12.21

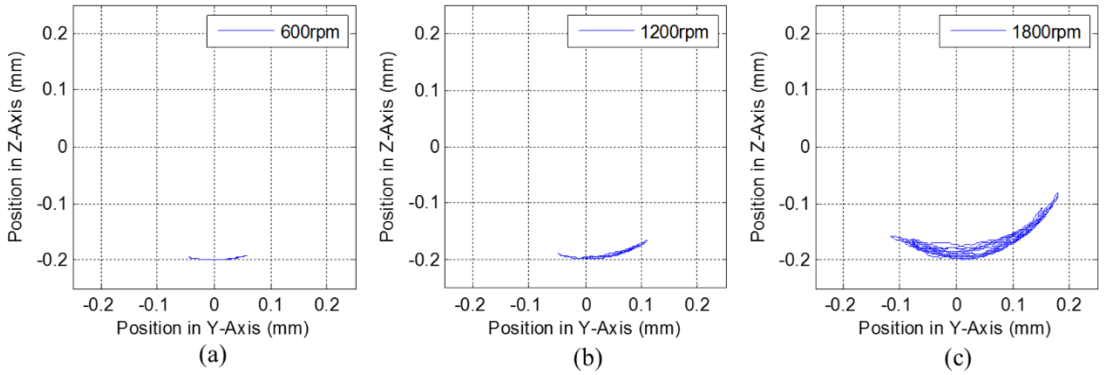

Figure 5.21. Simulated cage center of mass motions for the three speed cases under the same bearing axial load (445N): (a) 600rpm shaft speed, (b) 1200rpm shaft speed, (c) 1800rpm shaft speed.

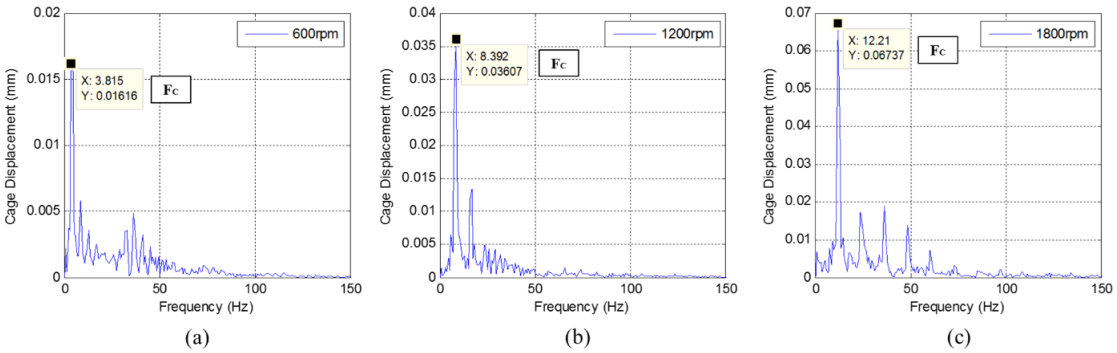

Figure 5.22. Simulated cage displacement in frequency domain: (a) 600rpm shaft speed, (b) 1200rpm shaft speed, (c) 1800rpm shaft speed.

5.4.2 Cage Dynamics in a Pristine Bearing – Effect of Radial Load

The bearing cage motion is highly dependent on the external loading conditions. Stacke et al. [7, 8] presented results for an angular contact ball bearing with a ball-guided polymer cage. They showed that in a radially loaded case, the cage moved in a chaotic manner since the balls in the loaded zone guided the cage differently than the balls in the unloaded zone. In the current study,

the test bearing was loaded under pure radial load of 445 N and operated at 1200 rpm. Please note that the radial load will introduce an axial reaction force in the angular contact bearing.

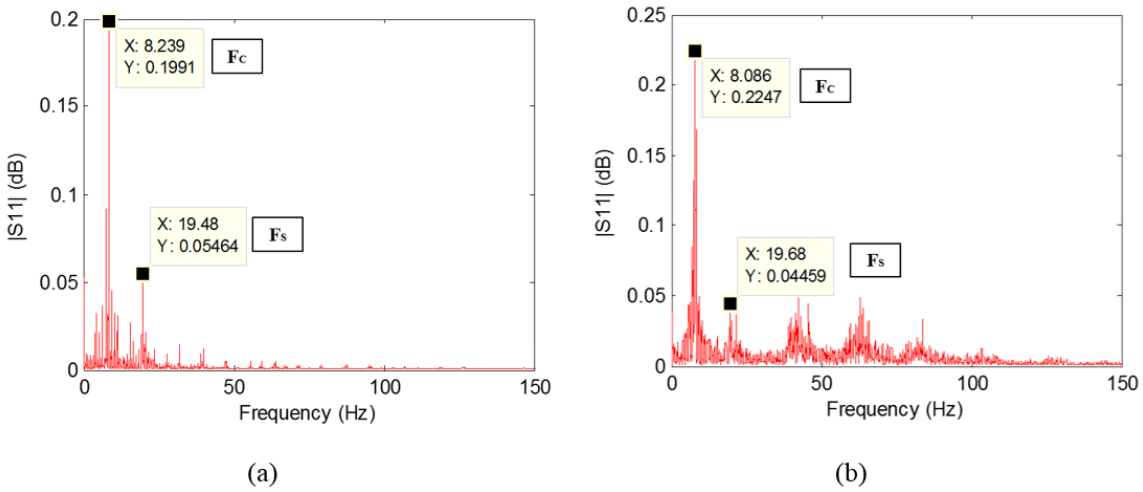

Figure 5.23. Detected telemeter signals of the two loading cases at 1200rpm: (a) axial load 445 N, (b) radial load 445 N.

Figure 5.23 demonstrates a comparison between the cage telemeter signal obtained from an axially loaded case and a radially loaded case. In both cases, the cage frequency and shaft frequency were detected, but the overall vibration level was higher when the bearing was subject to radial load. This result indicated an unstable cage motion, and it correlated well with the "chaotic" motion measured by Stacke et al. [7, 8] in a radially loaded bearing.

The dynamic bearing modeling supported the experimental result. Figure 5.24 depicts the chaotic motion of the EFEM cage when the radial load was applied to the bearing model. Figure 5.25 plots the contact forces acting between the ball and cage pocket for the two loading cases. While the magnitude of the contact force quickly dropped after start-up in an axially loaded bearing, the large discrete contact forces in a radially loaded bearing showed that the ball was frequently impacting the cage and was causing more vibrations on the cage. It also needs to be pointed out that the magnitude of the contact force depends on the stiffness and damping parameters in the contact model, the actual contact force has to be verified experimentally.

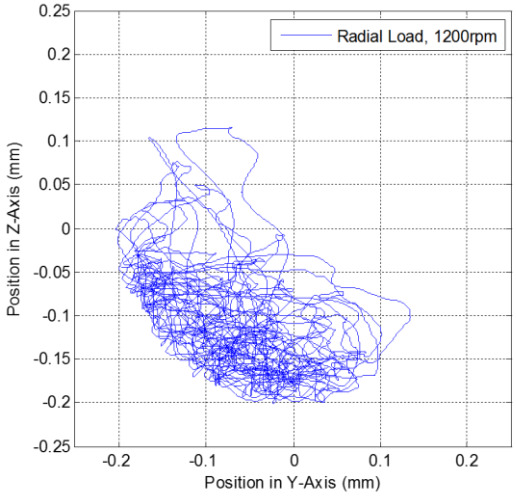

Figure 5.24. Simulated flexible cage center of mass motion in the bearing under radial load.

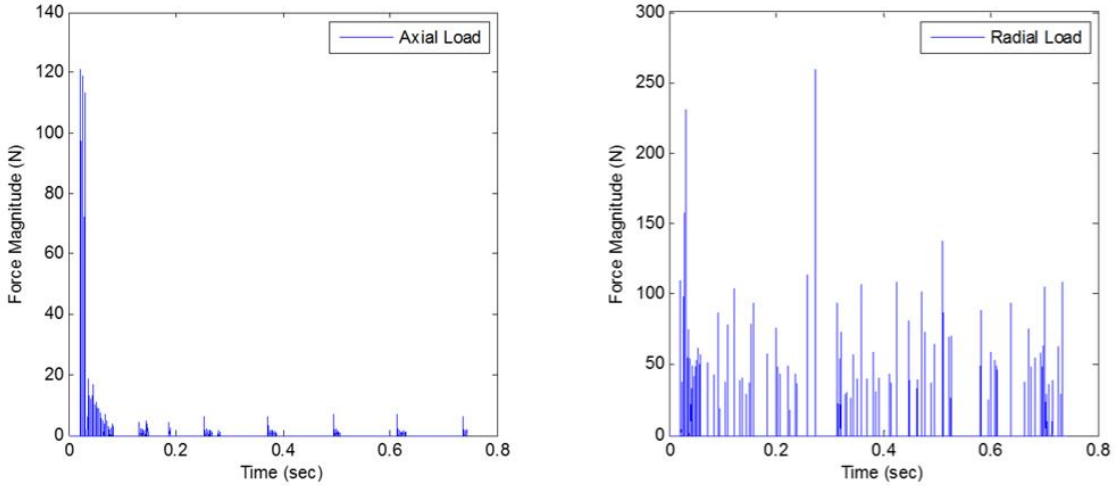

(a) (b)

Figure 5.25. Simulated ball-pocket contact force in two loading cases: (a) axial load, (b) radial load.

Cage flexibility has a significant influence on the cage motion and dynamics. In order to demonstrate the effects of cage flexibility on bearing dynamics, the dynamic bearing model (DBM) was used to investigate cage motion for a rigid and EFEM cage under the same operating condition. This allowed a direct comparison between the two approaches. Figure 5.26 depicts the results obtained from DBM for a rigid cage operating under the same load (445N) and speed (1200 rpm) conditions as the simulation in Figure 5.25. Comparing the result depicted in Figure

5.26 to the motion of the flexible cage in Figure 5.24, the rigid cage experienced greater vibrations and more instability due to its large contact stiffness. The flexible cage, on the other hand, deforms under contact forces (Figure 5.27 illustrates the cage deformation), and demonstrates a higher compliance.

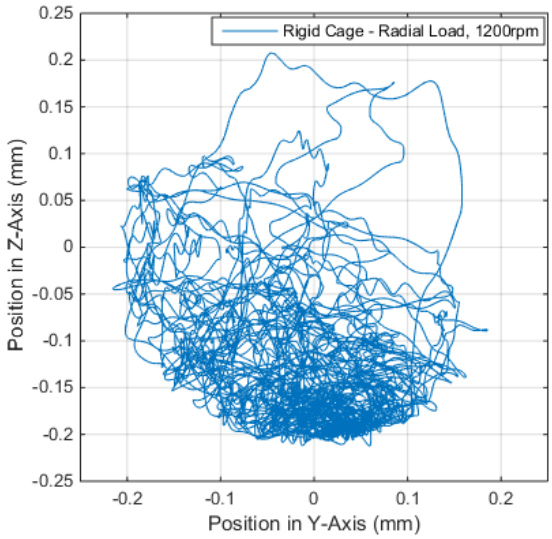

Figure 5.26. Simulated rigid cage center of mass motion in the bearing under radial load.

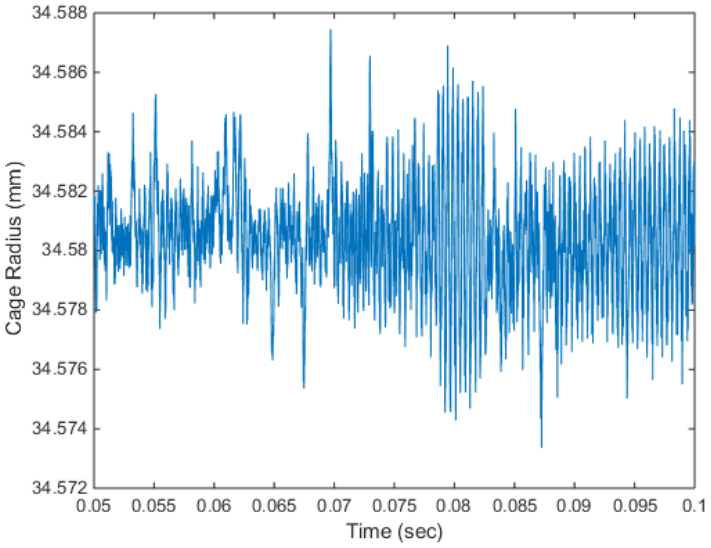

Figure 5.27. Variation in the radius of the flexible cage in the bearing under radial load.

5.4.3 Detection of Bearing Defect - Ball Pass Frequency on Outer Race

Surface defect, such as a dent or spall, indicates the imminent failure of an operating bearing. And the detection of bearing defect is critical to preventing sever damage from occurring. To demonstrate the bearing defect detection using the cage telemeter, a spall was seeded on the bearing outer race as shown in Figure 5.28. In the bearing model, the surface profile of the outer race was also modified to incorporate the spall, which was approximated by a curve with 6 mm radius (R) and two rounded corners with 1 mm radius (r). The spall shape created in the model is depicted in Figure 5.29.

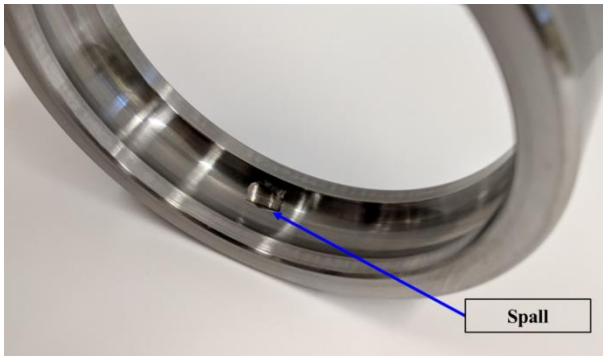

Figure 5.28. Bearing outer race with a spall in the raceway.

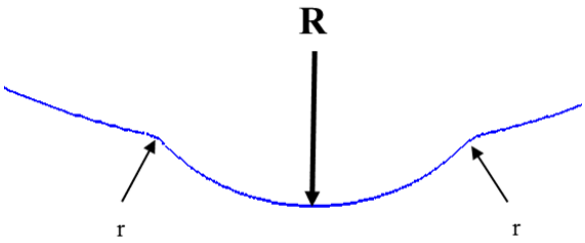

Figure 5.29. Spall profile in the dynamic bearing model (R=6mm, r=1mm).

An axial load of 445 N was applied to the bearing in the test rig and the motor speed was set to 1800 rpm. Figure 5.30 shows the signal spectrum from the telemeter. Besides the cage speed frequency and shaft speed frequency, the ball pass frequency on outer race (BPFO) was also detected due to the damaged bearing outer race.

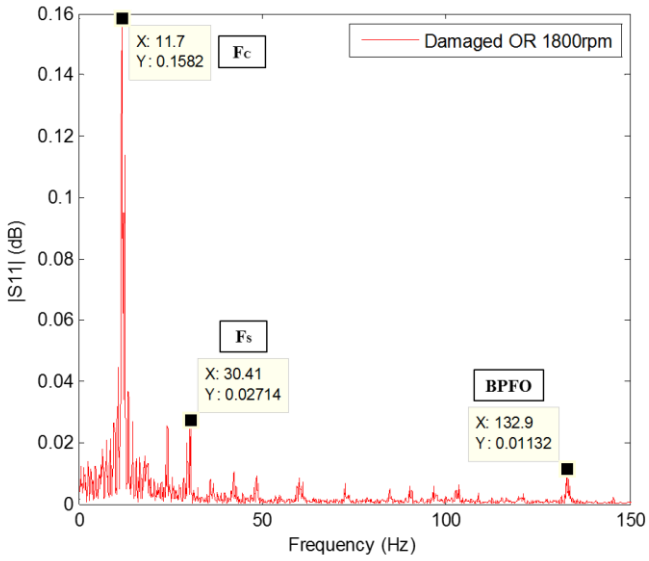

Figure 5.30. Detected telemeter signal from the test ball bearing with outer race damage (bearing was under 445N axial load, and bearing speed was 1800rpm).

5.4.4 Comparison with Accelerometers

To compare the performance of the cage telemeter with the performance of accelerometers, two accelerometers (piezoelectric accelerometer, 100mV/g sensitivity) were attached to the outer perimeter of the bearing housing, as depicted in Figure 5.31. The positions of the accelerometers were also varied to measure vibration signal on the bearing housing along different directions. Figure 5.31(a) depicts two accelerometers mounted along 0º (+Y axis) and 90º (+Z axis), and in Figure 5.31(b) the accelerometers were along +45º and -45º. Please note that the spall on the outer race was positioned along the –Z axis. The results from accelerometers in Figure 5.31(a) were shown in Figure 5.32 and accelerometers in Figure 5.31(b) produced results in Figure 5.33. It can be seen that since the spall position was along the –Z axis, the accelerometer along 90º (+Z) detected a dominant BPFO frequency, the ones along +45º and -45º have also detected the BPFO frequency but with a reduced signal amplitude and the accelerometer along 0º, which was orthogonal to spall location (-90º), was not able to discern the BPFO frequency signal from noises. Figure 5.34 shows the bearing outer race displacement result from the simulation, and it confirmed that the bearing outer race vibration was much larger along the +Z direction.

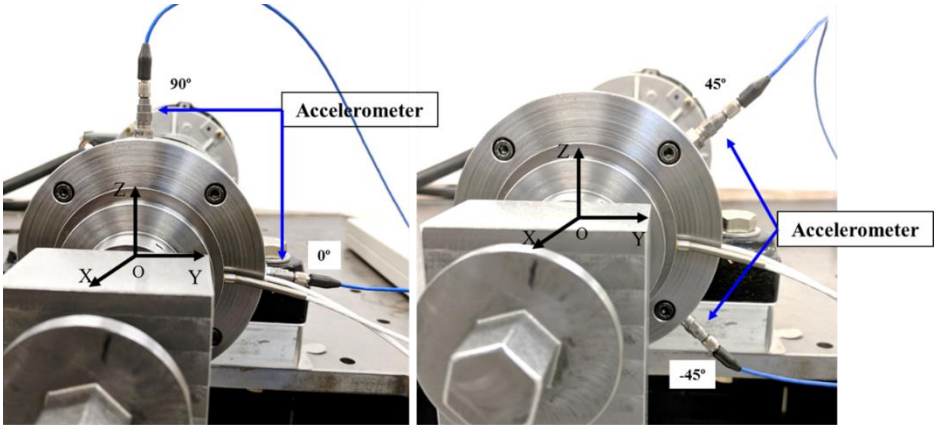

Figure 5.31. Accelerometers attached on test bearing housing: (a) along 0º and 90º, (b) along +45ºand -45º.

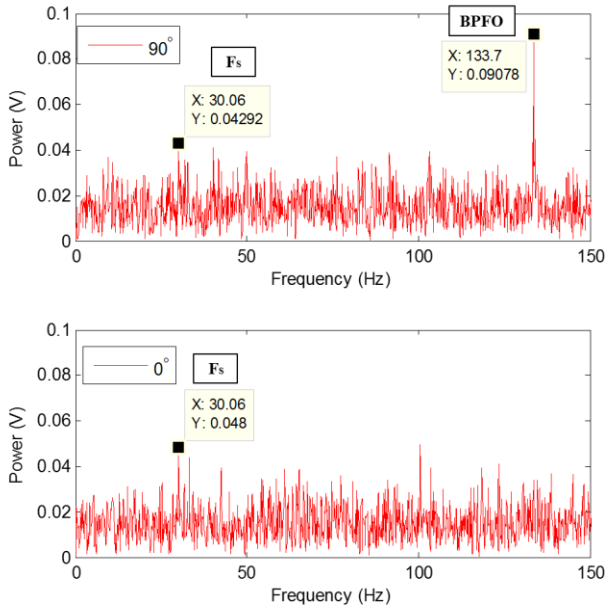

Figure 5.32. Detected accelerometer signals along 0º and 90º.

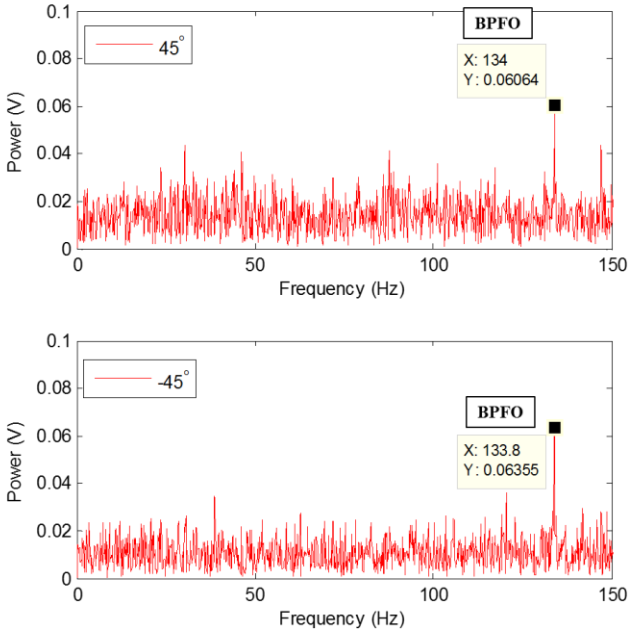

Figure 5.33. Detected accelerometer signals along +45º and -45º.

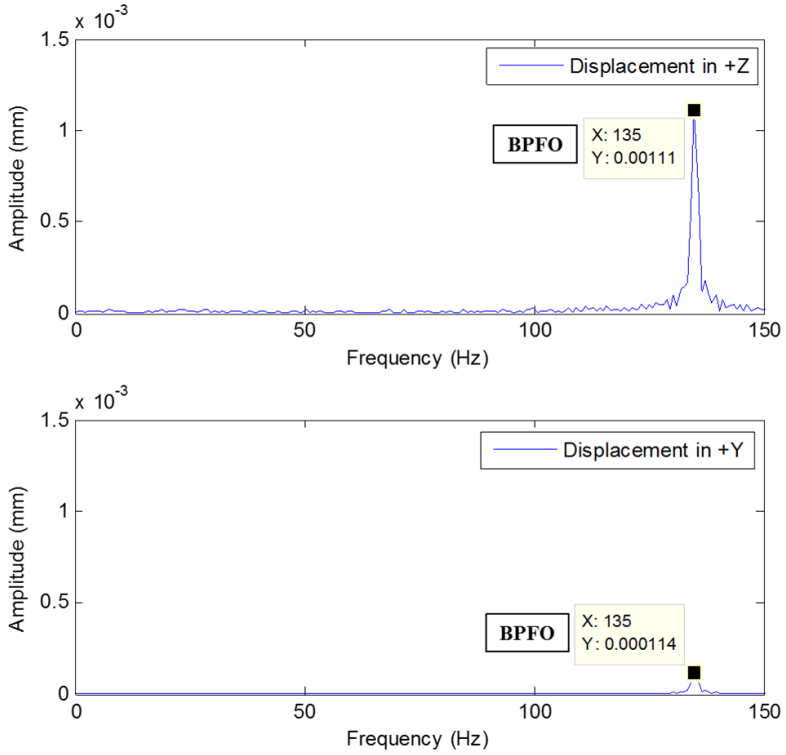

Figure 5.34. Simulated bearing outer race displacements along +Z and +Y directions.

It can be concluded from these results that the detection of bearing defect using standard accelerometers on bearing housing relies on the proper positioning of the accelerometer. The detection is less successful if it is positioned away from the vibration transfer path. The cage telemeter, on the other hand, is not limited by the location of the damage since it measures vibration signals along all directions simultaneously. Please also note that the accelerometers were not able to detect any signals related to the cage, as the cage motions are not directly transferred to the outer race or housing.

5.5 Conclusions

In this chapter, a cage telemeter was designed and developed to demonstrate its capability in detecting the bearing cage motions and dynamics. A dynamic bearing model with EFEM cage was developed to compare the analytical and experimental results. The telemeter is based on an LC circuit similar to previous published temperature telemeters [53, 59]. Experimental results showed that the cage telemeter can identify the cage motion and frequency under various operating conditions. The cage telemeter could measure the chaotic cage vibrations caused by different loading conditions, such as a pure radial load. The cage telemeter also showed some advantages over the accelerometers. It could serve as a cage motion sensor as well as a bearing vibration sensor. While the accelerometer placement is critical to measurement, the cage telemeter does not have such limitation. The results obtained from the model demonstrated significantly more details in the cage motion and dynamics. Analytical results showed that at low speeds, the motion of the outer race guided cage was governed by the gravity, however the cage began to whirl as the speed increased. A radial load applied to the bearing resulted in a chaotic cage motion since the radial load caused a small load zone which caused the balls to constantly impact the cage when moving across the loaded and unloaded zones.

CHAPTER 6. SUMMARY AND FUTURE WORK

6.1 Summary

In chapter 2, an explicit finite element model was developed to model bearing housings and combined with a discrete element dynamic bearing model to investigate the effect of housing flexibility on bearing dynamics. In this investigation, all bearing components are allowed six degrees-of-freedom except the outer race which was allowed only five DOF. The DOF which allows for the bearing to rotate (fret) in the housing was neglected. Two different housing support materials (i.e. elastic and viscoelastic) were considered in this investigation using EFEM. A novel rigid and deformable body contact model using the penalty method was developed to detect and determine contact forces between the rigid outer race and deformable housing. Housings with different geometries were developed and used to demonstrate the effects of housing on outer race and inner race motions. The results from this investigation show that the housing deformation is significant and cannot be neglected in modeling bearing dynamics. The analysis for rubber bushing demonstrated that, due to the viscoelastic behavior, rubber deformation is rate dependent and as expect illustrated the rubber advantages over steel in damping impact loading.

In chapter 3, a new EFEM bushing model was presented that allows for investigations of the effect of elastomeric bushings on bearing dynamics. Results of the proposed elastomeric bushing model show good agreement with the existing experimental work. It is further shown that the model can successfully simulate the expected dynamic performance of elastomeric bushings for various material properties and bushing geometries, however further experimental validation is necessary in future work.

The EFEM bushing model was combined with a dynamic bearing model to study bearing motion and dynamics. While the existing bearing models commonly assume fixed outer race and fail to include the bearing support flexibility, the presented model has no such constraints. It is demonstrated that compared to rigid support (fixed outer race), elastomeric bushings exhibit more effective damping to improve the stability of bearing systems under variable loadings. Furthermore, the damping behavior can be tuned by choosing proper bushing geometries and

properties. The flexibility of the bushing also improves the compliance of bearings to angular misalignment, and as a result, bearing reaction forces are reduced.

In chapter 4, a combined EFEM-DEM dynamic rotor-bearing model has been developed to study the behaviors of rotor, bearing and bearing housing under various conditions. The dynamic bearing model is based on the discrete element method and the flexible rotor and housing models are developed using the explicit finite element method. The results show that both the bearing internal clearance and housing bore clearance have a significant impact on the VC (Varying Compliance) vibration. The magnitude of VC vibration decreases as the bearing internal clearance becomes smaller. A large housing clearance, on the other hand, will lead to insufficient support stiffness and bearing unstable motion as the contact area between bearing OR and housing reduces significantly. It was also demonstrated that deflection of the rotor causes the generation of bearing reaction forces and moments, which can also be affected by bearing clearance. Housing deformation was shown to vary with the reactions generated within the bearing. Therefore it is important to properly choose the clearances as well as the location of external load, since the behaviors of each component (bearing, rotor, housing, etc.) are interrelated with each other. Rotor first critical speed was also studied, and housing flexibility was shown to increase the IR displacement at resonance. When the rotor reaches large deflection at critical speed, reaction moment increases in the bearing accordingly. And typically a large reaction moment is related to an increase in contact force and friction which may reduce bearing life.

In chapter 5, a cage telemeter was designed and developed to demonstrate its capability in detecting the bearing cage motions and dynamics. A dynamic bearing model with EFEM cage was developed to compare the analytical and experimental results. The telemeter is based on an LC circuit similar to previous published temperature telemeters [53, 59]. Experimental results showed that the cage telemeter can identify the cage motion and frequency under various operating conditions. The cage telemeter could measure the chaotic cage vibrations caused by different loading conditions, such as a pure radial load. The cage telemeter also showed some advantages over the accelerometers. It could serve as a cage motion sensor as well as a bearing vibration sensor. While the accelerometer placement is critical to measurement, the cage telemeter does not have such limitation. The results obtained from the model demonstrated

significantly more details in the cage motion and dynamics. Analytical results showed that at low speeds, the motion of the outer race guided cage was governed by the gravity, however the cage began to whirl as the speed increased. A radial load applied to the bearing resulted in a chaotic cage motion since the radial load caused a small load zone which caused the balls to constantly impact the cage when moving across the loaded and unloaded zones.

6.2 Future Work

6.2.1 Rotor-Bearing Dynamics with Elastomeric Support

Bearing support is critical to the performance of rotor-bearing systems. For instance, the rotor-bearing in a high speed turbocharger relies on a proper support to stabilize the system and constrain rotor-bearing motions. In Chapter 4, it was presented that flexibility of a steel housing can significantly alter the motions of bearing components. The same the model may be modified to include elastomeric support which was studied in Chapter 3. Analytical studies can be conducted to investigate the effect of elastomeric support on rotor-bearing performance, and provide a rule of thumb for the design of elastomeric supports in actual applications. Experimental investigations can also be carried out in the future to verify the performance of elastomeric support in a rotor-bearing system.

6.2.2 Bearing Performance at High Speed

The current combined DEM-EFEM bearing model has been used to study bearing dynamics at relatively low bearing speed. And the analysis using the current model can be extended to high speed conditions. At higher speed, the dynamics of rolling elements and bearing cage are of particular interest. The model can also be used to study the vibrational behavior of flexible bodies such as housing, rotor, and cage, and their impacts on the bearing performance as the bearing is operating at much higher speed.

6.2.3 Investigation of Fretting in Bearing

A bearing assembly is subject to fretting wear at the bearing-shaft and bearing-housing interfaces. Chapter 4 has described the contact model used between bearing outer race and housing inner surface. And the normal and frictional forces are calculated for each node on the housing inner surface and bearing outer race. The same contact model can be applied to the

inner race and shaft interface. Then the modified model can be used to study the fretting phenomenon at these two interfaces. Fretting wear is a function of relative motion between the two bodies and the magnitude of the contact force. If wear is properly calculated, it can be included as a dependent variable for bearing clearances.

6.2.4 Further Development of Cage Vibration Sensor

The current cage vibration sensor, as presented in Chapter 5, is able to detect the cage vibration frequency, but it cannot discern the direction and exact position of the cage center of mass. Therefore, in the future development of this vibration sensor, it should be extended to measure cage motions in all directions (three displacements, three rotations) separately, and the signal may be calibrated with the motion magnitude. If these can be achieved, then the vibration sensor is capable of detecting the cage position/orientation continuously.

REFERENCES

1. Jones, A. B. (1960), “A General Theory for Elastically Constrained Ball and Radial Roller Bearings,” Transactions of the ASME. Series D, Journal of Basic Engineering, 82, pp 309-320.
2. Harris, T. A. (1966), *Rolling Bearing Analysis*, John Wiley.
3. Gupta, P. K., (1984), *Advanced Dynamics of Rolling Elements*, Springer-Verlag, New York
4. Saheta, V., (2001), “Dynamics of Rolling Element Bearings Using Discrete Element Method,” MS thesis, Purdue University, West Lafayette, IN.
5. Ghaisas, N., Wassgren, C., and Sadeghi, F. (2004), “Cage Instabilities in Cylindrical Roller Bearings,” Journal of Tribology, 126(4), pp 681-689.
6. Adams, M. L. (1980), "Non-linear dynamics of flexible multi-bearing rotors." Journal of Sound and Vibration 71.1, pp 129-144.
7. Stacke, L. E., Dag F., and Patrik N.. (1999), "BEAST—a rolling bearing simulation tool." Proceedings of the Institution of Mechanical Engineers, Part K: Journal of Multi-body Dynamics 213.2, pp 63-71.
8. Stacke, L. E., and Dag F.. (2001), "Dynamic behaviour of rolling bearings: simulations and experiments." Proceedings of the Institution of Mechanical Engineers, Part J: Journal of Engineering Tribology 215.6, pp 499-508.
9. Ashtekar, A., & Sadeghi, F. (2012). A new approach for including cage flexibility in dynamic bearing models by using combined explicit finite and discrete element methods. Journal of Tribology, 134(4), 041502.
10. Weinzapfel, N., and Sadeghi, F. (2009), “A Discrete Element Approach for Modeling Cage Flexibility in Ball Bearing Dynamics Simulations,” Journal of Tribology, 131(2).
11. Hill, J. M., 1975, "Radical deflections of rubber bush mountings of finite lengths." International Journal of Engineering Science 13.4, pp. 407-422.
12. Horton, J. M., and Tupholme, G. E, 2006, "Approximate radial stiffness of rubber bush mountings." Materials & design 27.3, pp. 226-229.

13. Horton, J. M., Gover, M. J. C., and Tupholme, G. E., 2000, "Stiffness of rubber bush mountings subjected to tilting deflection." Rubber chemistry and technology73.4, pp. 619-633.
14. Berg, M, 1998, "A non-linear rubber spring model for rail vehicle dynamics analysis." Vehicle system dynamics 30.3-4, pp. 197-212.
15. Sjöberg, M. M., and Kari, L., 2002, "Non-linear behavior of a rubber isolator system using fractional derivatives." Vehicle System Dynamics 37.3, pp. 217-236.
16. Mooney, M., 1940, "A theory of large elastic deformation." Journal of applied physics 11.9, pp 582-592.
17. Rivlin, R. S., and Saunders, D. W., 1951, "Large elastic deformations of isotropic materials. VII. Experiments on the deformation of rubber." Philosophical Transactions of the Royal Society of London. Series A, Mathematical and Physical Sciences 243.865, pp 251-288.
18. Yeoh, O. H., 1993, "Some forms of the strain energy function for rubber." Rubber Chemistry and technology 66.5, pp 754-771.
19. Ogden, R. W., 1972, "Large deformation isotropic elasticity-on the correlation of theory and experiment for incompressible rubberlike solids." Proceedings of the Royal Society of London. A. Mathematical and Physical Sciences 326.1567, pp 565-584.
20. Wang, M. C, and Guth, E., 1952, "Statistical theory of networks of non-Gaussian flexible chains." The Journal of Chemical Physics 20.7, pp 1144-1157.
21. Flory, P. J., and Rehner Jr, J., 1943, "Statistical Mechanics of Cross-Linked Polymer Networks I. Rubberlike Elasticity." The Journal of Chemical Physics 11.11, pp 512-520.
22. Treloar, L. R. G., 1946, "The elasticity of a network of long-chain molecules.—III." Trans. Faraday Soc. 42, pp 83-94.
23. Treloar, L. R. G., The physics of rubber elasticity. Oxford University Press, 1975.
24. Arruda, E. M., and Boyce, M. C., 1993, "A three-dimensional constitutive model for the large stretch behavior of rubber elastic materials." Journal of the Mechanics and Physics of Solids 41.2, pp 389-412.
25. Kuhn, W., and Grun, F., 1942, "The crystal structure of polyethylene." Koll.-Z. 101, pp 248-262.

26. Bergström, J. S., and Boyce, M. C., 1998, "Constitutive modeling of the large strain time-dependent behavior of elastomers." Journal of the Mechanics and Physics of Solids 46.5, pp 931-954.
27. Kaliske, M, and Rothert, H., 1997, "Formulation and implementation of three-dimensional viscoelasticity at small and finite strains." Computational Mechanics 19.3, pp 228-239.
28. Kadlowec, J., Wineman, A., and Hulbert, G., 2003, "Elastomer bushing response: experiments and finite element modeling." Acta mechanica 163.1-2, pp. 25-38.
29. Olsson, A. K., and Austrell, P. E., 2003, "Finite element analysis of a rubber bushing considering rate and amplitude dependent effects." CONSTITUTIVE MODELS FOR RUBBER, pp. 133-140.
30. Jeffcott, H. H., (1919), "XXVII. The lateral vibration of loaded shafts in the neighbourhood of a whirling speed.—The effect of want of balance." The London, Edinburgh, and Dublin Philosophical Magazine and Journal of Science, 37(219), 304-314.
31. Kim, Y. B., and Noah, S. T, (1990), "Bifurcation analysis for a modified Jeffcott rotor with bearing clearances." Nonlinear Dynamics, 1(3), 221-241.
32. Lund, J. W, (1974), "Stability and damped critical speeds of a flexible rotor in fluid-film bearings." Journal of Engineering for Industry, 96(2), 509-517.
33. Bansal, P. N., and Kirk, R. G. (1975). "Stability and damped critical speeds of rotor-bearing systems." Journal of Engineering for Industry, 97(4), 1325-1332.
34. Nelson, H. D., and McVaugh, J. M. (1976), "The dynamics of rotor-bearing systems using finite elements." Journal of Engineering for Industry, 98(2), 593-600.
35. El-Saeidy, F. M. (1998). "Finite element modeling of a rotor shaft rolling bearings system with consideration of bearing nonlinearities." Journal of Vibration and Control, 4(5), 541-602.
36. Gupta, T. C., Gupta, K., and Sehgal, D. K. (2011). "Instability and chaos of a flexible rotor ball bearing system: an investigation on the influence of rotating imbalance and bearing clearance." Journal of engineering for gas turbines and power, 133(8), 082501.
37. Rao, J.S., and Sreenivas, R., (2003), "Dynamics of a three level rotor system using solid elements." In ASME Turbo Expo 2003, collocated with the 2003 International Joint Power Generation Conference (pp. 601-606). American Society of Mechanical Engineers.

38. Ashtekar, A., and Sadeghi, F. (2011). “Experimental and Analytical Investigation of High Speed Turbocharger Ball Bearings.” Journal of Engineering for Gas Turbines and Power, 133(12), 122501.
39. Brouwer, M. D., Sadeghi, F., Ashtekar, A., Archer, J., and Lancaster, C. (2015). “Combined Explicit Finite and Discrete Element Methods for Rotor Bearing Dynamic Modeling.” Tribology Transactions, 58(2), 300-315.
40. Nicholas, J. C., and Barrett, L. E. (1986). “The effect of bearing support flexibility on critical speed prediction.” ASLE transactions, 29(3), 329-338.
41. Vance, J. M., Murphy, B. T., and Tripp, H. A. (1987). “Critical speeds of turbomachinery: computer predictions vs. experimental measurements—part II: effect of tilt-pad bearings and foundation dynamics.” Journal of vibration, acoustics, stress, and reliability in design, 109(1), 8-14.
42. Vázquez, J. A., Barrett, L. E., and Flack, R. D. (2001). “A flexible rotor on flexible bearing supports: stability and unbalance response.” Journal of Vibration and Acoustics, 123(2), 137-144.
43. Cao, L., Brouwer, M. D., Sadeghi, F., and Stacke, L. E. (2016). “Effect of Housing Support on Bearing Dynamics.” Journal of Tribology, 138(1), 011105.
44. Cao, L., Sadeghi, F., and Stacke, L. E. (2016). “An Explicit Finite Element Model to Investigate the Effects of Elastomeric Bushing on Bearing Dynamics.” Journal of Tribology.
45. Hamrock, B., Schmid, S., and Jacobson, B. (2004), *Fundamentals of Fluid Film Lubrication*, Marcel Dekker, New York.
46. Miller, K., Joldes, G., Lance, D., & Wittek, A. (2007). Total Lagrangian explicit dynamics finite element algorithm for computing soft tissue deformation. *Communications in numerical methods in engineering*, *23*(2), 121-134.
47. Bower, A. F. (2011). *Applied mechanics of solids*. CRC press.
48. Ok, J. K., Yoo, W. S., and Sohn, J. H., 2007, Experimental study on the bushing characteristics under several excitation inputs for bushing modeling. International journal of automotive technology, 8(4), pp. 455-465.
49. Ashtekar, A., Sadeghi, F., and Stacke, L. E., 2008, "A new approach to modeling surface defects in bearing dynamics simulations." *Journal of Tribology*, 130(4), 041103.

50. Nickel, D. A., and Sadeghi, F., 1997,"In Situ Tribocomponent Temperature Measurement Using a Radio Telemeter", Tribology Transactions, 40(3), pp 514-520.
51. Joshi, A., Marble, S., and Sadeghi, F., 2001, "Bearing Cage Temperature Measurement Using Radio Telemetry," Proceedings of the Institution of Mechanical Engineers, Part J: Journal of Engineering Tribology, 215(5), pp 471–481.
52. Kovacs, A. S., 2008, Early-Warning Wireless Telemeter for Harsh-Environment Bearings, Master's Thesis, Purdue University, West Lafayette, Indiana.
53. Ashtekar, A., Kovacs, A. S., Sadeghi, F., and Peroulis, D., 2010, "Bearing Cage Telemeter for the Detection of Shaft Imbalance in Rotating Systems," Radio and Wireless Symposium (RWS), pp 5–8.
54. Tandon, N., and Choudhury, A. (1999). "A review of vibration and acoustic measurement methods for the detection of defects in rolling element bearings." Tribology international, 32(8), 469-480.
55. McFadden, P. D., and Smith, J. D. (1984). "Model for the vibration produced by a single point defect in a rolling element bearing." Journal of sound and vibration, 96(1), 69-82.
56. Ashtekar, A., Sadeghi, F., and Stacke, L. E. (2010). "Surface defects effects on bearing dynamics." Proceedings of the Institution of Mechanical Engineers, Part J: Journal of Engineering Tribology, 224(1), 25-35.
57. Sawalhi, N., and Randall, R. B. (2011). "Vibration response of spalled rolling element bearings: Observations, simulations and signal processing techniques to track the spall size." Mechanical Systems and Signal Processing, 25(3), 846-870.
58. Cao, H., Niu, L., and He, Z. (2012). "Method for vibration response simulation and sensor placement optimization of a machine tool spindle system with a bearing defect." Sensors, 12(7), 8732-8754.
59. Brouwer, M. D., Shahidi, A., Gupta, L. A., Sadeghi, F., and Peroulis, D. (2014, July). "Application of ball bearing cage RF temperature sensor in high speed turbocharger." In Antennas and Propagation Society International Symposium (APSURSI), 2014 IEEE (pp. 1312-1313). IEEE.
60. Kannel, J. W., and Bupara, S. S. (1978). "A simplified model of cage motion in angular contact bearings operating in the EHD lubrication regime." Journal of Lubrication Technology, 100(3), 395-403.

61. Gupta, P. K., Dill, J. F., and Bandow, H. E. (1985). “Dynamics of rolling element—bearings experimental validation of the DREB and RAPIDREB computer programs.” Journal of tribology, 107(1), 132-137.

62. Cao, L., Sadeghi, F., and Stacke, L. E. (2017). “A Combined EFEM–Discrete Element Method Dynamic Model of Rotor–Bearing–Housing System.” Journal of Tribology, 139(6), 061102.

VITA

Lijun Cao was born on July 27th, 1990 in Wuxi, Jiangsu Province, China. He attended Purdue University in West Lafayette, Indiana and received a Bachelor of Science in Mechanical Engineering. He then continued to pursue graduate studied in Mechanical Engineering at Purdue University as well. He joined the Mechanical Engineering Tribology Laboratory in July 2012, and received his Master of Science in Mechanical Engineering in December 2014. Upon completion of his doctorate, he joined SKF BV in Nieuwegein, Netherlands.